SSC-345

(PART 2)

ELASTIC - PLASTIC FRACTURE MECHANICS

MARINE STRUCTURAL APPLICATIONS

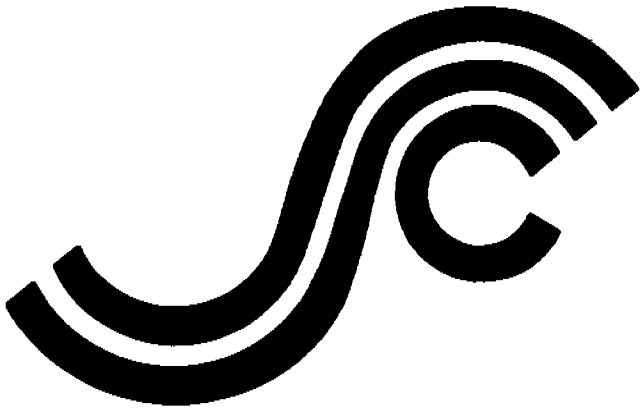

SHIP STRUCTURE COMMITTEE

1990

SHIP STRUCTURE COMMITTEE

The SHIP STRUCTURE COMMITTEE is constituted to prosecute a research program to improve the hull structures of ships and other marine structures by an extension of knowledge pertaining to design, materials, and methods of construction.

RADM J. D. Sipes, USCG, (Chairman)
Chief, Office of Marine Safety, Security and Environmental Protection
U. S. Coast Guard

Mr. Alexander Malakhoff
Director, Structural Integrity Subgroup (SEA 55Y)
Naval Sea Systems Command

Dr. Donald Liu
Senior Vice President
American Bureau of Shipping

Mr. H. T. Haller
Associate Administrator for Ship–building and Ship Operations
Maritime Administration

Mr. Thomas W. Allen
Engineering Officer (N7)
Military Sealift Command

CDR Michael K. Parmelee, USCG,
Secretary, Ship Structure Committee
U. S. Coast Guard

CONTRACTING OFFICER TECHNICAL REPRESENTATIVES

Mr. William J. Siekierka
SEA 55Y3
Naval Sea Systems Command

Mr. Greg D. Woods
SEA 55Y3
Naval Sea Systems Command

SHIP STRUCTURE SUBCOMMITTEE

The SHIP STRUCTURE SUBCOMMITTEE acts for the Ship Structure Committee on technical matters by providing technical coordination for determinating the goals and objectives of the program and by evaluating and interpreting the results in terms of structural design, construction, and operation.

AMERICAN BUREAU OF SHIPPING

Mr. Stephen G. Arntson (Chairman)
Mr. John F. Conlon
Mr. William Hanzalek
Mr. Philip G. Rynn

MILITARY SEALIFT COMMAND

Mr. Albert J. Attermeyer
Mr. Michael W. Touma
Mr. Jeffery E. Beach

MARITIME ADMINISTRATION

Mr. Frederick Seibold
Mr. Norman O. Hammer
Mr. Chao H. Lin
Dr. Walter M. Maclean

NAVAL SEA SYSTEMS COMMAND

Mr. Robert A. Sielski
Mr. Charles L. Null
Mr. W. Thomas Packard
Mr. Allen H. Engle

U. S. COAST GUARD

CAPT T. E. Thompson
CAPT Donald S. Jensen
CDR Mark E. Noll

SHIP STRUCTURE SUBCOMMITTEE LIAISON MEMBERS

U. S. COAST GUARD ACADEMY

LT Bruce Mustain

U. S. MERCHANT MARINE ACADEMY

Dr. C. B. Kim

U. S. NAVAL ACADEMY

Dr. Ramswar Bhattacharyya

STATE UNIVERSITY OF NEW YORK MARITIME COLLEGE

Dr. W. R. Porter

WELDING RESEARCH COUNCIL

Dr. Martin Prager

NATIONAL ACADEMY OF SCIENCES – MARINE BOARD

Mr. Alexander B. Stavovy

NATIONAL ACADEMY OF SCIENCES – COMMITTEE ON MARINE STRUCTURES

Mr. Stanley G. Stiansen

SOCIETY OF NAVAL ARCHITECTS AND MARINE ENGINEERS – HYDRODYNAMICS COMMITTEE

Dr. William Sandberg

AMERICAN IRON AND STEEL INSTITUTE

Mr. Alexander D. Wilson

Member Agencies:

United States Coast Guard
Naval Sea Systems Command
Maritime Administration
American Bureau of Shipping
Military Sealift Command

Ship Structure Committee

An Interagency Advisory Committee
Dedicated to the Improvement of Marine Structures

Address Correspondence to:

Secretary, Ship Structure Committee
U.S. Coast Guard (G-MTH)
2100 Second Street S.W.
Washington, D.C. 20593-0001
PH: (202) 267-0003
FAX: (202) 267-0025

December 17, 1990

SSC-345
SR-1321

ELASTIC-PLASTIC FRACTURE MECHANICS MARINE STRUCTURAL APPLICATIONS

This is the second part of a two part report. The first reviewed the history and state-of-the-art of elastic-plastic fracture mechanics. This volume presents the results of an analytical and experimental study of fracture in the ductile-brittle transition region in ship hull steels. It is important that we increase our knowlededge in this area of fundamental material properties. A fracture mechanics based approach to design and analysis can provide a more qualitative assessment of the integrity of marine structures.

J. D. SIPES
Rear Admiral, U.S. Coast Guard
Chairman, Ship Structure Committee

Technical Report Documentation Page

1. Report No.	2. Government Accession No.	3. Recipient's Catalog No.
SSC-345 - Part 2		

4. Title and Subtitle	5. Report Date
Elastic-Plastic Fracture Mechanics - Marine Structural Applications	April 1990
	6. Performing Organization Code
7. Author(s)	8. Performing Organization Report No.
T. L. Anderson	SR-1321
9. Performing Organization Name and Address	10. Work Unit No. (TRAIS)
Texas A & M Research Foundation P. O. Box 3578 College Station, TX 77843	11. Contract or Grant No. DTCG23-88-C-20037
	13. Type of Report and Period Covered
12. Sponsoring Agency Name and Address Commandant U.S. Coast Guard 2100 Second Street, SW Washington, DC 20593	Final Report
	14. Sponsoring Agency Code G-M

15. Supplementary Notes

Sponsored by the Ship Structure Committee and its member agencies.

16. Abstract

This document contains the results of experimental and analytical studies of fracture in the ductile-brittle transition zone for two ship steels, EH36 and HSLA 80. Tensile, Charpy and fracture toughness test results using different strain rates are presented. Fracture toughness was quantified by the J integral and the crack tip opening displacement (CTOD). Elastic-plastic finite element analysis was combined with a local failure criterion to derive size limits for J and CTOD testing in the transition regions. Relationships between J and CTOD were explored both experimentally and analytically. A theoretical Charpy-fracture toughness relationship was used to predict CTOD transition curves for the steels. Charpy and CTOD transition temperatures were compared for a number of steels.

17. Key Words	18. Distribution Statement
Fracture Mechanics Elastic-Plastic Deformation Fracture Toughness Transition Region	Available from: Nat'l Technical Information Service Springfield, VA 22161 or Marine Tech. Information Facility National Maritime Research Center Kings Point, NY 10024-1699

19. Security Classif. (of this report)	20. Security Classif. (of this page)	21. No. of Pages	22. Price
Unclassified	Unclassified	96	

Form DOT F 1700.7 (8-72) Reproduction of completed page authorized

METRIC CONVERSION FACTORS

Approximate Conversions to Metric Measures

Symbol	When You Know	Multiply by	To Find	Symbol
		LENGTH		
in	inches	*2.5	centimeters	cm
ft	feet	30	centimeters	cm
yd	yards	0.9	meters	m
mi	miles	1.6	kilometers	km
		AREA		
in^2	square inches	6.5	square centimeters	cm^2
ft^2	square feet	0.09	square meters	m^2
yd^2	square yards	0.8	square meters	m^2
mi^2	square miles	2.6	square kilometers	km^2
	acres	0.4	hectares	ha
		MASS (weight)		
oz	ounces	28	grams	g
lb	pounds	0.45	kilograms	kg
	short tons (2000 lb)	0.9	tonnes	t
		VOLUME		
tsp	teaspoons	5	milliliters	ml
Tbsp	tablespoons	15	milliliters	ml
fl oz	fluid ounces	30	milliliters	ml
c	cups	0.24	liters	l
pt	pints	0.47	liters	l
qt	quarts	0.95	liters	l
gal	gallons	3.8	liters	l
ft^3	cubic feet	0.03	cubic meters	m^3
yd^3	cubic yards	0.76	cubic meters	m^3
		TEMPERATURE (exact)		
°F	Fahrenheit temperature	5/9 (after subtracting 32)	Celsius temperature	°C

*1 in = 2.54 (exactly). For other exact conversions and more detailed tables, see NBS Misc. Publ. 286, Units of Weights and Measures, Price $2.25, SD Catalog No. C13.10:286.

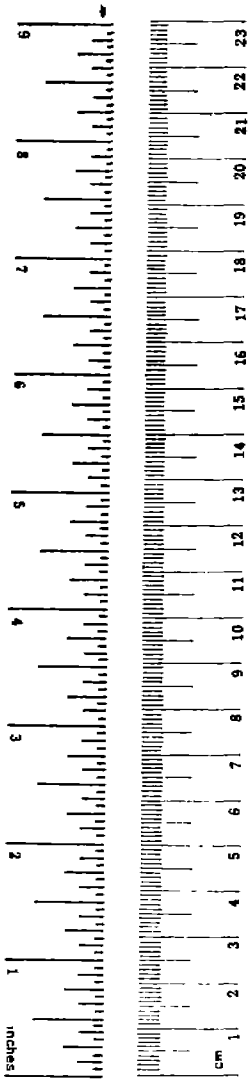

Approximate Conversions from M

Symbol	When You Know	Multiply by
		LENGTH
mm	millimeters	0.04
cm	centimeters	0.4
m	meters	3.3
m	meters	1.1
km	kilometers	0.6
		AREA
cm^2	square centimeters	0.16
m^2	square meters	1.2
km^2	square kilometers	0.4
ha	hectares (10,000 m^2)	2.5
		MASS (weight)
g	grams	0.035
kg	kilograms	2.2
t	tonnes (1000 kg)	1.1
		VOLUME
ml	milliliters	0.03
l	liters	2.1
l	liters	1.06
l	liters	0.26
m^3	cubic meters	35
m^3	cubic meters	1.3
		TEMPERATURE (exa
°C	Celsius temperature	9/5 (then add 32)

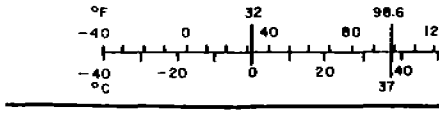

EXECUTIVE SUMMARY

This research program consisted of experimental and analytical studies of fracture in the ductile-brittle transition region of ship steels. Two materials were tested: a 25.4 mm thick plate of ASTM A 131 EH36 steel and a 31.8 mm plate of HSLA 80 steel. Tensile, Charpy, and fracture toughness tests were performed over a range of temperatures. The tensile tests were conducted at three strain rates: 0.0033, 5.1 and 280 s-1. Most of the Charpy and fracture toughness testing was concentrated in the transition region of each steel. Fracture toughness was quantified by the J integral and the crack tip opening displacement (CTOD).

Elastic-plastic finite element analysis was combined with a local failure criterion to derive size limits for J and CTOD testing in the transition region. These limits are eight times more strict than the size requirements for J_{IC} testing but are less severe than the requirements for a valid K_{IC} test. When fracture toughness data do not meet the required specimen size, the data can be corrected for constraint loss. This correction not only removes the size dependence of fracture toughness but also greatly reduces the scatter. Conceivably, this approach can also be applied to structures, although the computational requirements would be severe.

Relationships between J and CTOD were explored both analytically and experimentally. Both parameters are essentially equivalent measures of elastic-plastic toughness.

A theoretical Charpy-fracture toughness relationship was used to predict CTOD transition curves for the A 131 EH36 and HSLA 80 steels. Although the agreement between theory and experiment was reasonably good in both cases, further refinement and validation is needed before this approach can be used in practical situations. A parametric study showed that the predicted CTOD transition curve is highly sensitive to the dynamic flow properties.

Charpy and CTOD transition temperatures were compared for a number of steels. There appears to be no unique relationship between these two temperatures. Material toughness criteria based on Charpy energy should be used with extreme caution.

TABLE OF CONTENTS

1. INTRODUCTION

The Ship Structures Committee (SSC) has recognized the importance of fracture mechanics technology to the design and fabrication of marine structures. Existing fracture control procedures rely heavily on arbitrary Charpy impact requirements, but a fracture mechanics based approach would allow more quantitative assessments of structural integrity.

Many welded steel structures, such as ships, operate in or near the ductile-brittle transition region, where the failure mechanism is unstable cleavage. Although cleavage is often referred to as brittle fracture, cleavage in the transition region can be preceded by significant plastic deformation and stable tearing. Consequently, fracture in the transition region is typically elastic-plastic in nature; linear elastic fracture mechanics (LEFM) is usually invalid, and material toughness cannot be quantified by K_{IC}.

Most of the research in elastic-plastic fracture mechanics conducted in the United States has focused on the upper shelf of toughness. This work has been sponsored primarily by the nuclear power industry, which is concerned with service temperatures well in excess of ambient temperature. Fracture mechanics research in the United Kingdom, however, has been motivated largely by the construction of offshore platforms in the North Sea, where cleavage fracture is possible. Thus the elastic-plastic fracture mechanics methodology developed in the UK is more relevant to welded ship construction, but most designers and fabricators in the United States are unfamiliar with this technology.

The SSC asked Texas A&M University to undertake a research program on the application of elastic-plastic fracture mechanics to marine structures. The initial phase of this work involved a state-of-the-art critical review of the technology. This was followed by experimental and analytical studies which addressed some of the critical issues associated with fracture in the transition region.

The primary objectives of the literature review were as follows:

- To consolidate information from a wide variety of sources, both published and unpublished, into a single report.

- To facilitate a transfer of technology from the United Kingdom and other European countries to the United States.

- To identify critical issues which require further study.

The experimental and analytical work addressed some of the issued identified in the literature review.

1.1 THE LITERATURE REVIEW

The complete literature review was published as a separate report [1]. The main conclusions from the review are summarized below.

1.1.1 Fracture Toughness Testing

The American Society for Testing and Materials (ASTM) has published a number of standard test methods for measuring fracture toughness [2-5]. Plane strain, linear elastic fracture toughness can be quantified by K_{IC}, the critical stress intensity factor. Two elastic-plastic fracture toughness parameters are available: the J contour integral and the crack tip opening displacement (CTOD).

The K_{IC} test is of limited value for testing low- and medium-strength steels. If a steel can satisfy the size requirements of ASTM E399-83 [2], it is probably too brittle for structural applications. Thus fracture toughness in such materials must be quantified by elastic-plastic tests.

Fracture toughness testing procedures for materials on the upper shelf are well established. The J_{IC} and J-R curve standards [3,4] provide guidelines for measuring the material's resistance to ductile fracture initiation and crack growth. One problem receiving some attention is the crack growth limits in ASTM E1152-87 [4]. This research is driven primarily by the nuclear industry, where accurate tearing instability analyses are important, but this problem is only marginally important to the rest of the welding fabrication community.

Just as materials that satisfy the K_{IC} size criterion are usually too brittle, materials on the upper shelf are sufficiently tough so that fracture is often not a significant problem. The fracture research area most important to the welding fabrication industry is the ductile-brittle transition region.

Until recently, the transition region has received little attention from the fracture mechanics community in the United States. The CTOD test, the first standardized method which can be applied to the transition region, was published in 1989 by ASTM [5], whereas the British Standards Institute published a CTOD standard in 1979, and CTOD data were applied to welded structures in the UK as early as 1971 [6].

Because J integral test methods were originally developed for the upper shelf, there is no standardized J-based test that applies to the transition region. Such a standard should be developed so that J-based driving force approaches can be applied to structures in the transition region.

One problem with both J and CTOD testing in the transition region is the lack of size criteria to guarantee a single parameter characterization of fracture. The J_{IC} size requirements are probably not restrictive enough for cleavage, and the K_{IC} requirements are too severe for elastic-plastic fracture parameters. The appropriate size requirements can be established through a combination of finite element analysis and micromechanics models.

When a single parameter description of fracture toughness is not possible, as in shallow notched specimens and tensile panels, the issue of crack tip constraint becomes important. This is a very difficult problem. Unless a simple analysis is developed that characterizes constraint loss, these effects will be impossible to quantify without performing three-dimensional, elastic-plastic finite element analyses on every configuration of interest.

Another important issue is fracture toughness testing of weldments. Existing standards do not address the special considerations required for weldment testing. The Welding Institute and other organizations have developed informal procedures over the years, but such procedures need to be standardized.

Fracture toughness data in the transition region are invariably scattered, whether the tests are performed on welds or base materials, although the problem is worse in the heat-affected zone of welds. The nature of scatter in the lower transition region is reasonably well understood; procedures have been developed which allow for estimating lower-bound toughness with as few as three fracture toughness values. The problem of scatter in the upper transition region is more complicated; constraint loss and ductile crack growth combine to increase the level of scatter. Further work is necessary to quantify these effects.

An accurate correlation between Charpy energy and fracture toughness would be extremely useful. The empirical correlations developed to date are unreliable. Some progress has been made in developing theoretical correlations, but these

models do not take into account all factors. If an accurate relationship can be developed, material toughness criteria based on Charpy energy can be established rationally.

1.1.2 Application to Structures

Structural integrity can be inferred from fracture toughness by means of a driving force analysis, which relates toughness, stress and flaw size. Both linear elastic and elastic-plastic driving force analyses are available.

Although linear elastic fracture mechanics is of limited use in fracture toughness testing of structural steels, LEFM driving force relationships are suitable for many situations. A structure of interest, if it is sufficiently large or the stresses are low, may be subjected to nearly pure linear elastic conditions. Fracture toughness can be characterized on a small specimen by a critical J value, which can then be converted to an equivalent K_{IC} and compared to the applied K_I in the structure.

Pure LEFM analysis does carry risks, however. If the stresses are above approximately half the yield strength, plasticity effects can be significant. If the LEFM analysis does not contain some type of plasticity correction, it gives no warning when the linear elastic assumptions become suspect. Sufficient skill is necessary to determine whether or not an LEFM analysis is valid in a given situation.

It is perhaps better to apply an elastic-plastic driving force relationship to all problems; then, the appropriate plasticity corrections are available when needed. When a linear elastic analysis is acceptable, the elastic-plastic approach will reduce to the LEFM solution. Thus the analysis decides whether or not a plasticity correction is needed.

Several types of elastic-plastic fracture analyses are available. The CTOD design curve [7], based primarily on an empirical correlation between wide plate tests and CTOD data, is largely obsolete. Analyses based on the strip yield model [8] are still useful for low hardening materials. The Electric Power Research Institute (EPRI) procedure is the probably the most advanced analysis, but it is currently applicable to a limited range of configurations. The reference stress model [9], which is a modified version of the EPRI approach, is widely applicable. Any of these approaches can be expressed in terms of a failure assessment diagram. This is done merely for convenience, and has no significant effect on the outcome of the analysis.

A parametric comparison of elastic-plastic analyses produced some interesting results. As expected, the strip yield, reference stress, and EPRI analyses all agreed in

the linear elastic range. In the elastic-plastic and fully plastic ranges, where the three analyses might be expected to differ, predictions of failure stress and critical crack size were quite close in most cases; the only exception was when the strip yield model was applied to a high hardening material. All the analyses predicted similar failure stresses and critical crack sizes because failure in the fully plastic range is governed by the flow properties of the material. Above a certain level of toughness, critical values of stress and crack size are insensitive to fracture toughness.

The analyses do differ in the prediction of the applied J, but for a designer, critical crack size and failure stress are much more important quantities. Accurate predictions of the applied J may be impossible, even with an analysis that is theoretically perfect. The applied driving force in the plastic range is highly sensitive to the P/P_0 ratio, where P is the applied load and P_0 is the load at net section yield. A slight overestimate or underestimate of P_0 significantly affects the results. If the flow properties vary even by a few percent, the resulting error in P_0 leads to a large error in the J calculation.

In summary, the driving force expression probably does not matter in most cases. The only requirements are that the expression reduce to the LEFM solution for small scale yielding and predict the correct collapse limit under large scale yielding conditions. An additional proviso is that the strip yield approach or other non-hardening models should not be applied to high hardening materials.

Since the reference stress model [9] works nearly as well as the EPRI approach, there is little justification for the EPRI approach in non-nuclear applications. The EPRI procedure is more cumbersome because it requires a fully plastic geometry correction factor. The reference stress model produces similar results to the EPRI analysis and has the advantage of a geometry factor based on stress intensity solutions. Currently, there are many more published K solutions than fully plastic J solutions.

There are other reasons not to worry about applying accurate plastic geometry factors. Real structures, especially welded structures, pose many complex problems that existing analyses cannot address. The elastic-plastic driving force in a weldment cannot be represented accurately by a solution for a homogeneous structure. Additional factors such as residual stresses, three-dimensional effects, crack tip constraint, and gross-section yielding combine to increase the uncertainty and potential errors in fracture analyses. These errors are much more significant than those that might arise from choosing the strip yield or reference stress analysis over the EPRI approach. Until these complexities can be addressed, one may as well adopt a simple elastic-plastic analysis.

As a first step in a fracture analysis, a simple screening criterion may be appropriate. Two such approaches were introduced in the review. The yield-before-break criterion estimates the level of toughness required for the structure to reach net section yielding before fracture initiation. If the toughness is adequate to ensure yield-before-break conditions, fracture can be avoided simply by ensuring that the structure is loaded well below its limit load. An analogous quantity, the critical tearing modulus, is designed to ensure that the tearing resistance is adequate to avoid a tearing instability below the limit load.

1.2 EXPERIMENTAL AND ANALYTICAL STUDIES

The experimental and analytical portion of the research program addressed some of the important issues that were identified in the literature review. The results are outlined in the remainder of this report.

Chapter 2 describes the mechanical tests that were performed on two ship steels. Tensile, Charpy, and fracture toughness tests were conducted over a range of temperatures; most of the experiments concentrated on the ductile-brittle transition region of each material. These data were analyzed by various means in Chapters 3 and 4.

Chapter 3 addresses the issues of constraint and size effects on fracture toughness in the transition region. Elastic-plastic finite element analysis was performed by Professor R.H. Dodds of the University of Illinois as part of a separate study; in the present study, these results were used in conjunction with a micromechanical analysis to quantify the size dependence of cleavage fracture toughness. Specimen size requirements for critical J and CTOD values in the transition region were established. A separate article based on the analyses in Chapter 3 has been submitted for publication [10].

Various fracture tests for the transition region are compared in Chapter 4. The relationship between J and CTOD is explored, and the relative merits of each parameter are discussed. In addition, a theoretical relationship between Charpy energy and fracture toughness (critical J or CTOD values) is evaluated, and the structural significance of typical Charpy toughness requirements is assessed.

2. EXPERIMENTAL CHARACTERIZATION OF SHIP STEELS

2.1 TEST MATERIALS

Two ship materials were evaluated in this study: a 25.4 mm (1 in) thick plate of ASTM A 131 EH 36 steel and a 31.8 mm (1.25 in) thick plate of HSLA steel. The latter material was donated by David Taylor Research Center in Annapolis, Maryland. The chemical compositions of the two steels are shown in Table 2.1; the room temperature tensile properties are given in Table 2.2.

2.2 EXPERIMENTAL PROCEDURE

Tensile, Charpy and fracture toughness tests were performed on each material, with the majority of tests concentrated in the ductile-brittle transition region.

2.2.1 Tensile Tests

Round tensile specimens with 6.35 mm (0.25 in) diameter and 31.8 mm (1.25 in) gage length were machined in the longitudinal and transverse direction for the EH 36 steel and HSLA 80 steel, respectively. These orientations correspond to the principal axes of the Charpy and fracture toughness specimens. The tests were performed over a range of temperatures and at three nominal strain rates: 0.0033 s^{-1}, 5.1 s^{-1}, and 280 s^{-1}.

For the slowest strain rate, the guidelines of ASTM E 8 were followed. Low temperatures were achieved by a methanol bath cooled by dry ice and liquid nitrogen. For tests conducted below the freezing point of methanol, an insulated chamber cooled by nitrogen vapor was used.

For the two highest strain rates, each specimen was insulated with closed-cell foam, and liquid nitrogen was sprayed intermittently onto the specimen until the desired temperature was reached. Temperature was monitored by a thermocouple attached to the specimen surface.

The intermediate strain rate (5.1 s^{-1}) was achieved with a conventional closed-loop servohydraulic test machine. An open-loop servohydraulic test machine,

which was specially designed for dynamic tests, was required for the high rate tensile tests ($\dot{\varepsilon} \sim 280$ s).

Load and elongation were recorded by a computer data acquisition system. In the case of the two highest rates, data were first collected by a storage oscilloscope and then down-loaded to the computer. The load-elongation curves in the high rate tests contained a high degree of noise due to dynamic oscillations in the specimens; a four-point averaging technique was used to smooth these curves.

2.2.2 Charpy Impact Tests

Charpy impact tests were performed in accordance with ASTM E 23. Specimens were machined from the center and near the surface of each plate. The EH 36 specimens were oriented in the L-T direction, while the HSLA 80 specimens were machined in the T-L orientation.

The pendulum impact testing machine used in this investigation has a 120 ft-lb capacity, but the upper shelf energies of both steels were well in excess of this value. Thus it was only possible to characterize the lower half of the transition curve in this study. Upper shelf energies for the EH 36 material were given on the mill sheet. A previous testing program at David Taylor Research Center quantified the upper shelf toughness of the HSLA 80 plate.

2.2.3 Fracture Toughness Tests

Single edge notched bend (SENB) specimens were machined out of each plate. The specimen orientation matched that of the Charpy specimens; i.e., L-T for the EH 36 steel and T-L for the HSLA 80 steel. A total of 40 SENB specimens were machined from the EH 36 plate, while 20 specimens were fabricated from the HSLA 80 material.

The dimensions of the SENB specimens for both materials are shown in Fig. 2.1. The EH 36 specimens were fabricated in the full-thickness, Bx2B configuration, where B is the plate thickness (1.0 in). The loading span was 203 mm (8.0 in). The HSLA 80 specimens were side-grooved to a net thickness of 25.4 mm (1.0) in. The width and loading span matched that of the EH 36 specimens: 50.8 mm and 203 mm, respectively.

All specimens were fatigue precracked at room temperature. Fatigue loads were selected in accordance with ASTM E 1290.

Low temperatures were achieved by means of a well insulated chamber that was cooled by nitrogen vapor. Two thermocouples mounted on each specimen were connected to a controller which regulated the flow of nitrogen.

The tests were performed in displacement control. All specimens were instrumented with a clip gage at the crack mouth, and a few specimens were also equipped with a comparison bar-LVDT assembly that measured load-line displacement. The latter measurement was only made at higher test temperatures because the LVDT was not reliable below - 50°C. The plastic rotational factor, r_p, was computed from the tests where the load line displacement was measured. Since r_p is insensitive to temperature [11], the load line displacement could be inferred at low temperature from the clip gage displacement and r_p.

The nominal transition curve for the EH 36 steel plate was established with approximately 12 specimens; the remaining EH 36 specimens were tested at two temperatures in the transition region. All of the HSLA 80 specimens were tested in or near the transition region.

A critical J and critical CTOD value was computed from each test. The relationship in E 1290 was used for the CTOD calculations, and J was inferred from the load v. clip gage displacement record by means of the following equation [11]:

$$J = \frac{K^2 (1-\nu^2)}{E} + \frac{2 U_p^v}{B (W-a)} \left[\frac{W}{z + a + r_p(W-a)} \right] \tag{2.1}$$

where U_p^v is the area under the load-clip gage displacement curve, a is crack length, W is specimen width, and z is the knife edge height.

2.3 RESULTS

2.3.1 Tensile Data

Tensile properties for the two steels at various strain rates and temperatures are given in Tables 2.3 to 2.7. Figures 2.2 and 2.3 are plots of the quasistatic flow properties as a function of temperature. The tensile strength is plotted as a function of temperature and strain rate in Figs. 2.4 and 2.5. Note that the highest tensile strength for each material was measured at the intermediate strain rate.

A variety of possible explanations for the anomalous behavior in Figs. 2.4 and 2.5 were explored. Since the tensile tests at the three strain rates were performed on

three different machines, we initially postulated that one or more machine may be out of calibration, and thus give incorrect loads. However, subsequent checks revealed that all three load cells were well within acceptable calibration limits. Another possible explanation is associated with the level of noise in the high rate tests. Figure 2.6 shows a typical load-displacement record for a high rate tensile test *after* conditioning the data by four-point averaging. Although the averaging process reduces the noise, it may also remove important information. The absolute maximum load in each test was well above that obtained from averaged plots such as Fig. 2.6. Since the high peak loads were caused by dynamic oscillations, we assumed that the averaged curves were more indicative of material flow properties. However, the fact that the apparent tensile strength from the averaged plots is below the tensile strength at a slower strain rate indicates that this assumption may not be valid.

Figures 2.7 to 2.11 compare stress-strain curves at the slow and intermediate strain rates. Note that the noise level at $\dot{\varepsilon} = 5.1\ s^{-1}$ is very small; thus it is possible to resolve upper and lower yield points on the flow curves. Both materials appear to be highly sensitive to strain rate; the yield strength increases by a factor of two in some cases. The elongation to fracture decreases with strain rate, as does the strain hardening rate. In some cases, the tensile strength at $\dot{\varepsilon} = 5.1\ s^{-1}$ is actually less than the upper yield stress (eg. Fig. 2.11).

2.3.2 Charpy Data

Figures 2.12 and 2.13 show Charpy transition curves for the two steels. These data are listed in Tables 2.8 to 2.11. Both steels exhibit steep transitions from ductile to brittle behavior, a phenomenon that is typical of low carbon steels.

Both materials also have very high upper shelf energies. As stated earlier, the Charpy test machine at Texas A&M has only a 120 ft-lb (163 J) capacity, but the upper shelf energy was provided on the mill sheet in the case of the EH36 steel and by David Taylor Research Center in the case of the HSLA 80. Some specimens exceeded the capacity of the larger Charpy machines, as indicated on Figs 2.12 and 2.13 as well as Tables 2.10 and 2.11.

2.3.3 Fracture Toughness Data

Fracture toughness data for the two steels are listed in Tables 2.12 and 2.13. The CTOD data are plotted as a function of temperature in Figs. 2.14 and 2.15. Critical J values obtained from the same tests are plotted in Figs. 2.16 and 2.17. These data display the expected level of scatter in the transition region.

Replicate tests were performed at two temperatures in the transition region of each steel in order to assess scatter quantitatively. Figures 2.18 and 2.19 are Weibull plots of CTOD data in the transition region for both materials. The Weibull distribution, which is commonly used to describe scatter in fracture toughness data, is given by

$$F = 1 - \exp\left(-\left(\frac{\delta}{\theta}\right)^{\beta}\right) \tag{2.2}$$

where F is the cumulative probability, δ is the variable of interest (CTOD in this case), θ is the Weibull scale parameter, and β is the shape parameter, which is also referred to as the Weibull slope. This latter quantity corresponds to the slope of a Weibull plot and is a measure of the data scatter; a low β value indicates a high degree of scatter.

Figure 2.18 shows fracture toughness data for the EH36 steel at -80 and -60°C. The data at -60°C degrees were censored to exclude the two upper shelf values that were obtained at this temperature. That is, the δ_m values were included in the total number of tests (which is required to compute F) but were not plotted in Fig. 2.18 and were not used to compute the Weibull slope. Note that the slope at -60°C is lower than at -80°C, indicating more scatter at the higher temperature. The average toughness is higher at -60°C, and some of the specimens at this temperature exhibited stable tearing prior to cleavage. As discussed in Chapter 3, large scale yielding and stable tearing leads to a loss of constraint, which in turn increases the level of scatter in fracture toughness.

Figure 2.19 is a Weibull plot for the HSLA steel at -60°C and -40°C. The Weibull slope at -40°C is actually slightly higher than at the lower temperature, which is the opposite trend to what was observed in Fig. 2.18. However, very little can be concluded from the comparison of the two curves in Fig. 2.19; a Weibull fit on only five data points (-40°C) is highly unreliable.

Figure 2.20 compares the fracture toughness for both materials at -60°C. The two steels have similar Weibull slopes and median toughness at this temperature, although the EH36 steel has slightly higher toughness.

TABLE 2.1
Chemical composition of the A 131 EH36 and HSLA 80 steel plates.

Material	C	Mn	P	S	Si	Cu	Ni	Cr	Mo	V	Al	Nb
A 131 EH36	0.15	1.42	0.013	0.001	0.33	0.03	0.03	0.02	0.007	0.006	0.039	0.026
HSLA 80	0.03	0.50	0.012	0.001	0.300	*	0.92	0.89	0.200	*	0.037	0.040

*Not reported.

TABLE 2.2
Ambient temperature tensile properties as reported on the mill sheets.

Material	0.2% Yield Strength (MPa)	Tensile Strength (MPa)	Elongation (%)	Reduction in Area (%)
A 131 EH36	380	530	32	*
HSLA 80	530	611	32	81

*Not reported.

TABLE 2.3
Quasistatic tensile properties of the A 131 EH36 steel plate as a function of temperature. $\dot{\varepsilon} = 0.0033\ s^{-1}$

Temperature (°C)	Upper Yield Stress (MPa)	Lower Yield Stress (MPa)	Tensile Strength (MPa)
23	418	379	534
23	386	372	530
0	421	386	537
-10	457	393	548
-20	457	404	569
-30	467	418	576
-40	470	418	576
-50	470	428	629
-60	428	428	590
-60	519	428	604
-70	506	457	636
-80	517	463	639
-80	470	460	639
-100	460	443	629

TABLE 2.4

Quasistatic tensile properties of the HSLA 80 steel plate as a function of temperature. $\dot{\varepsilon} = 0.0033\ s^{-1}$

Temperature (°C)	Upper Yield Stress (MPa)	Lower Yield Stress (MPa)	Tensile Strength (MPa)
23	611	583	660
23	604	583	660
0	611	590	667
-20	639	597	681
-40	639	625	710
-60	639	618	710
-80	688	632	723
-90	702	653	737

TABLE 2.5

Tensile properties for the A 131 EH36 steel plate at $\dot{\varepsilon} = 5.1\ s^{-1}$.

Temperature (°C)	Upper Yield Stress (MPa)	Lower Yield Stress (MPa)	Tensile Strength (MPa)
23	771	657	820
-20	905	752	910
-60	953	830	958
-80	996	856	965
-100	923	898	971

TABLE 2.6

Tensile properties for the HSLA 80 steel plate at $\dot{\varepsilon} = 5.1\ s^{-1}$.

Temperature (°C)	Upper Yield Stress (MPa)	Lower Yield Stress (MPa)	Tensile Strength (MPa)
23	910	885	977
-20	997	924	1016
-40	1030	988	1046
-80	1103	1063	1092
-100	1226	1121	1138

TABLE 2.7

Approximate tensile strength of the two steel plates at $\dot{\varepsilon} = 280\ s^{-1}$.

Material	Temperature (°C)	Tensile Strength (MPa)
A131 EH36 Steel	23	650
	23	683
	23	726
	23	755
	-20	829
	-60	864
	-80	874
HSLA 80 Steel	23	931
	-20	915
	-40	909
	-60	955
	-80	918

TABLE 2.8

Charpy impact data obtained at Texas A&M University for the A131 EH36 steel plate. L-T orientation.

Temperature (°C)	Absorbed Energy (J)					
	Surface			Center		
-150	5			5		
-120	5			5		
-100	5			5		
-95	5	44	13	12		
	22	24	22			
	32	12	9			
-90	18	29		15		
-85	114	105	19	83	37	111
	7	15	69	103	111	121
	123	47		52	53	
-80	163*			33	58	
-75	163*	152		22	133	114
				56		

*Specimen did not separate.

TABLE 2.9
Charpy impact data obtained at Texas A&M University for the HSLA 80 steel plate. T-L orientation.

Temperature (°C)	Absorbed Energy (J)			
	Surface		Center	
-150	8			
-145			9	
-140	11	12		
-130	9		28	
-125	12			
-120	163*	15	27	
-115	14			
-110	163*	160*	57	13
-105			7	163*
-100			153	163*
-90			153	

*Specimen did not separate.

TABLE 2.10
Charpy impact data for the A 131 EH36 steel plate provided on the mill sheet. L-T orientation.

Temperature (°C)	Absorbed Energy (J)			
-40	223	300*	239	242
	259	300*	297	243
	224	300*	295	221
	235	300*	277	235

*Specimen did not separate.

TABLE 2.11
Charpy impact data for the HSLA 80 steel plate provided by David Taylor Research Center. T-L orientation.

Temperature (°C)	Absorbed Energy (J)			
-84	220	323	318	326*
	4	227	326*	324*
	214	322	316	235
	326*	202	313	326*
	237	233	265	326*
	326*	209	255	326*
	237	326*	326*	205
	326*	261	324*	224
	326*			
-73	334	323	308	355*
	346	334	339	338
	237	318	225	355*
	255	323	320	355*
	353*	318	334	223
	339	331	335	355*
	342	355*	322	355*
	255			
-18	326*	326*	326*	

*Specimen did not separate.

Table 2.12
Fracture toughness data for the A131 EH36 steel plate. L-T orientation.

Temperature (°C)	Critical CTOD (mm)	Critical J (kPa m)	Result Type*	Ductile Crack Extension (mm)
-100	0.015	23.63	δ_c	
-80	0.151	134.7	c	
	0.362	278.8	c	
	0.128	112.4	c	
	0.262	206.1	c	
	0.162	131.7	c	
	0.0725	73.2	c	
	0.189	157.1	c	
	0.261	207.9	c	
	0.0763	71.1	c	
	0.187	153.2	c	
	0.0593	64.62	c	
	0.197	197.5	c	
	0.267	246.8	c	-
-70	0.168	232.1	c	-
-60	0.433	325	c	-
	0.576	422.9	u	0.184
	0.35	252.9	c	-
	0.302	221.2	c	-
	0.234	257.1	c	-
	2.388	2671	m	-
	0.745	549.9	u	0.517
	0.0747	70.05	c	-
	0.327	239.6	c	-
	1.973	1560	u	1.308
	0.7576	557.1	u	0.369
	2.597	1545	m	-
	0.566	418.4	u	0.294
-50	0.267	196.7	c	-
	2.73	2432	m	-
	2.027	2556	m	-
-40	2.641	2254	m	-
-30	2.369	2306	m	-
23	2.921	1671	m	-

* c-Cleavage without stable tearing; u-Cleavage with stable tearing m-Maximum load plateau.

Table 2.13
Fracture toughness data for the HSLA 80 steel plate. T-L orientation.

Temperature (°C)	Critical CTOD (mm)	Critical J (kPa m)	Result Type	Ductile Crack Extension (mm)
-100	0.0776	87.2	c	
	0.0377	42.4	c	
-90	0.0235	27.2	c	
-80	0.0210	67.8	c	
-60	0.838	1080	u	0.460
	0.120	184	c	
	0.146	177	c	
	0.100	148	c	
	0.229	368	c	
	0.302	376	c	
	0.587	769	u	0.353
	0.691	420	u	0.397
	0.738	759	u	0.343
	0.307	368	c	
-50	0.067	143.4	c	
-40	0.237	306.5	c	
	1.179	1466	u	0.743
	0.885	1443	u	0.885
	0.605	584	u	0.605
	0.799	970.6	u	0.598

* c-Cleavage without stable tearing; u-Cleavage with stable tearing m-Maximum load plateau.

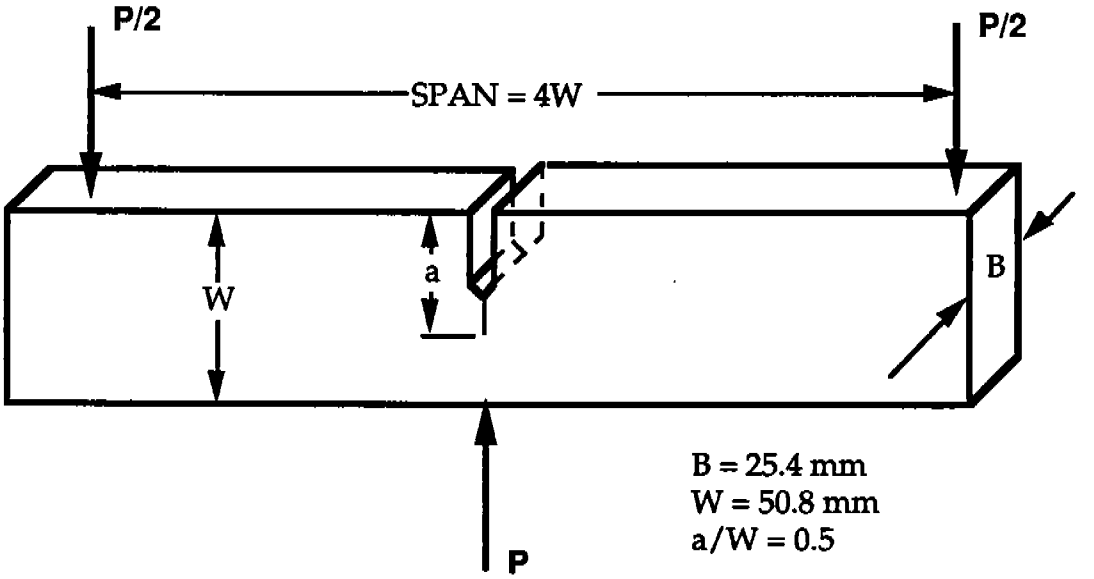

(a) A 131 EH36 steel specimens (L-T orientation).

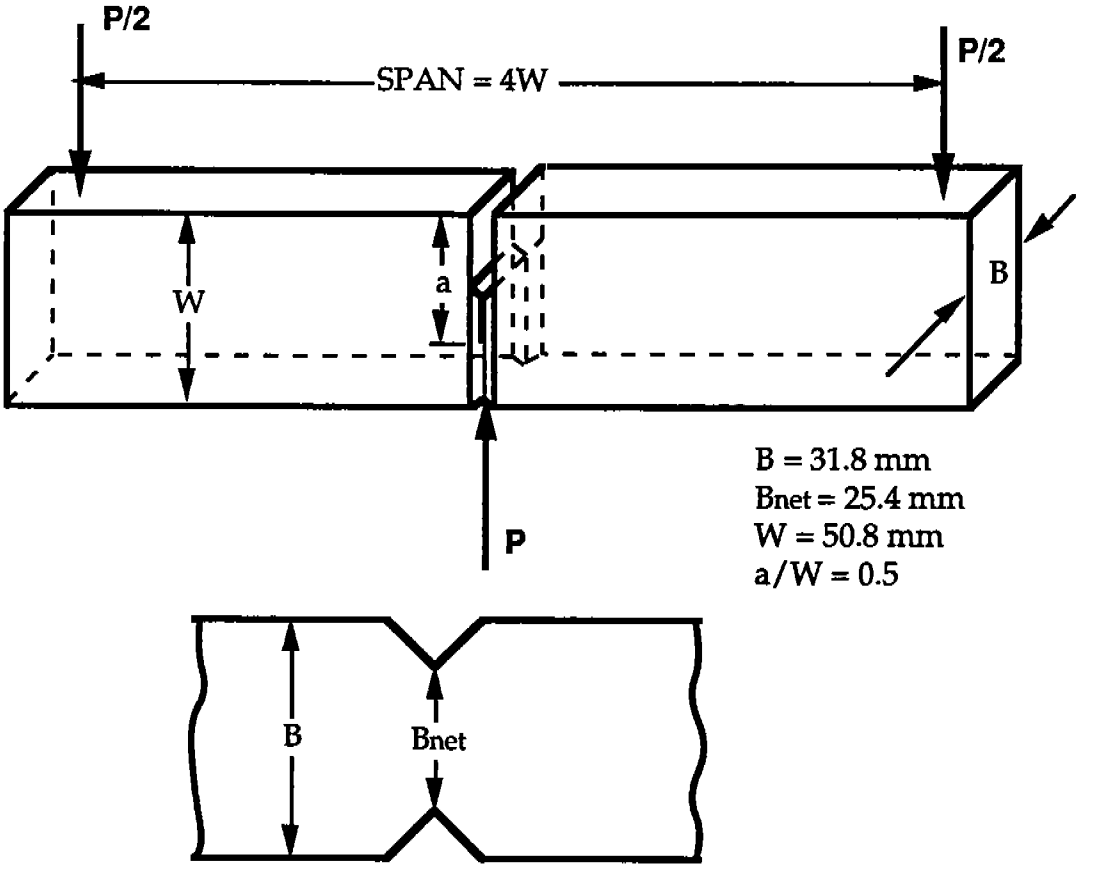

(b) HSLA 80 side grooved specimens (T-L orientation).

FIGURE 2.1 Single edge notched bend (SENB) specimens used for fracture toughness testing.

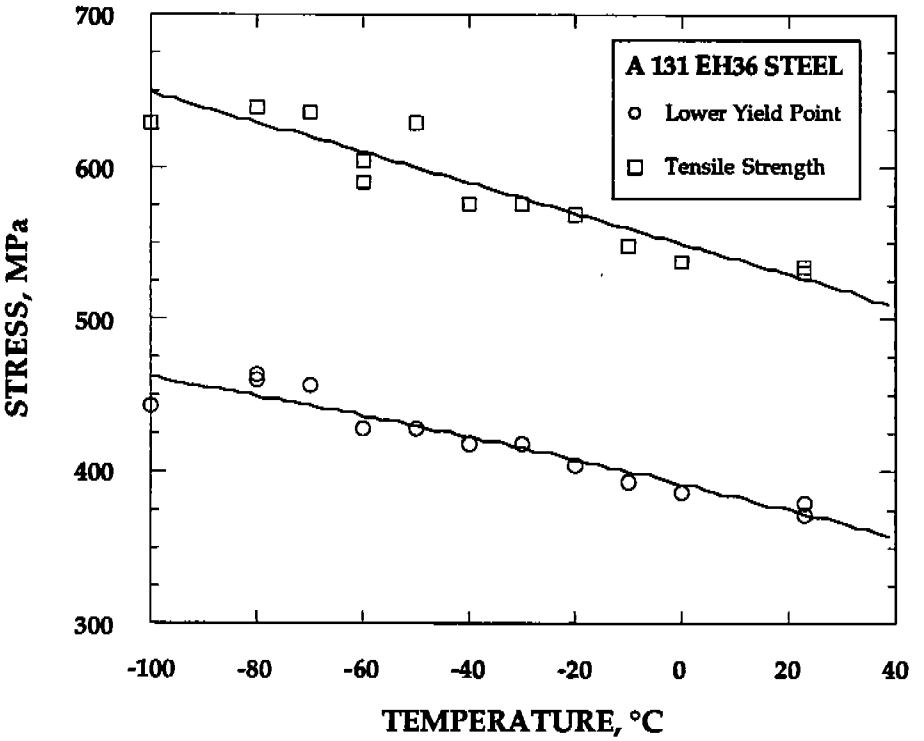

FIGURE 2.2 Quasistatic tensile properties of the A131 EH36 steel plate.

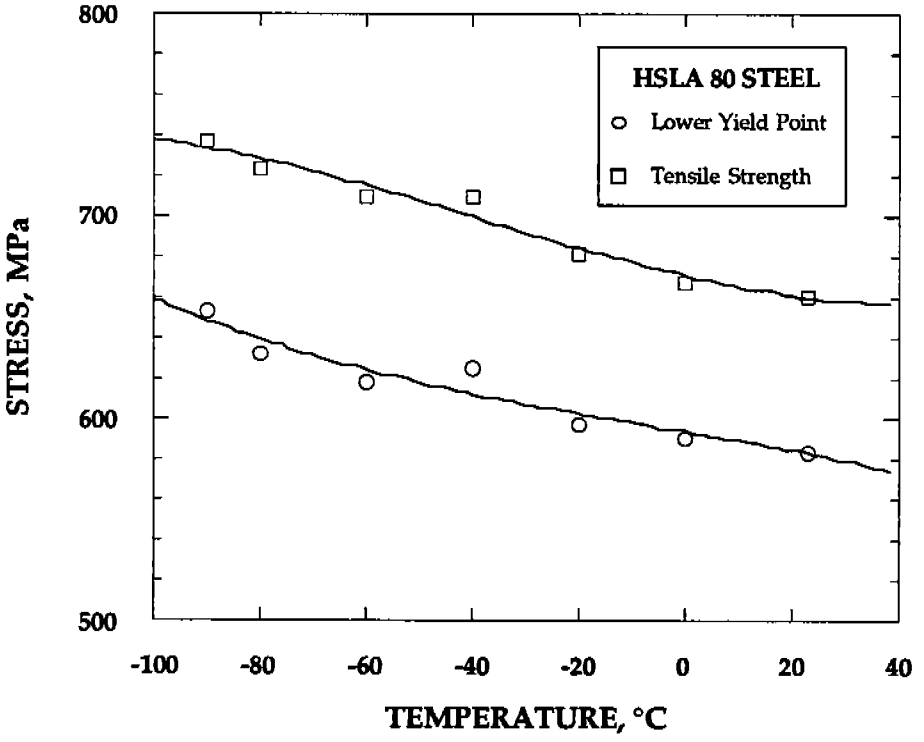

FIGURE 2.3 Quasistatic tensile properties of the HSLA 80 steel plate.

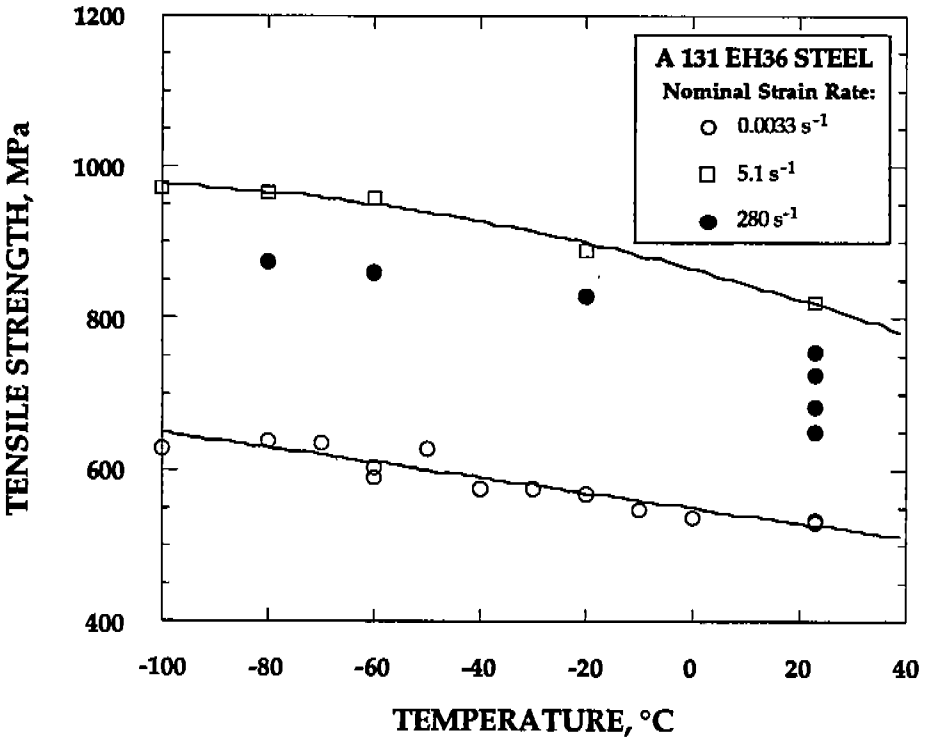

FIGURE 2.4 Tensile strength at three strain rates for the A131 EH36 steel plate.

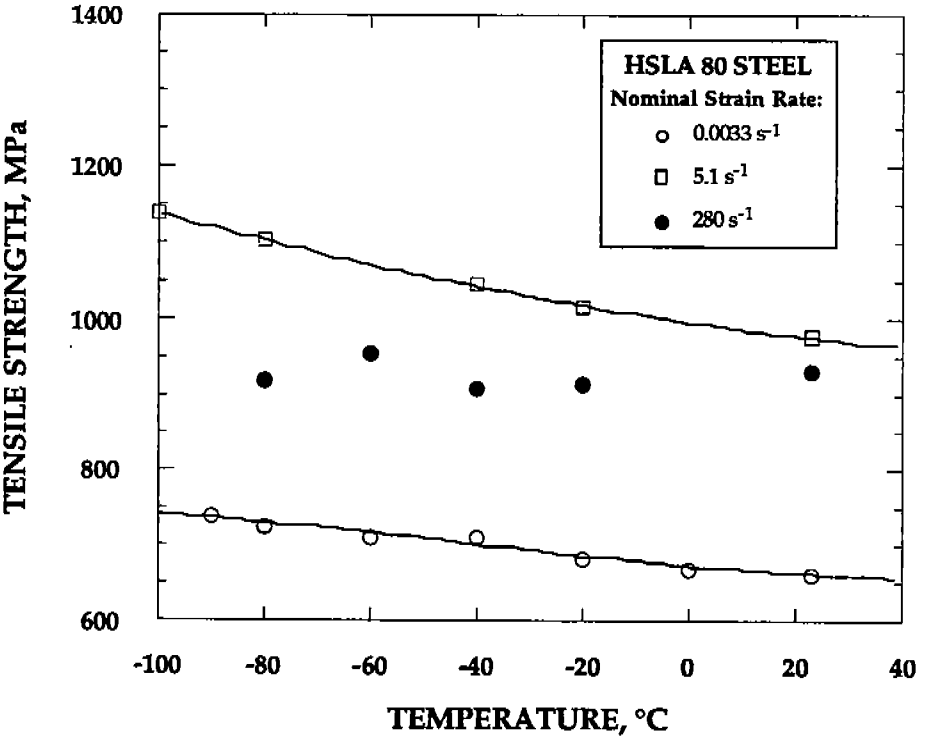

FIGURE 2.5 Tensile strength at three strain rates for the HSLA 80 steel plate.

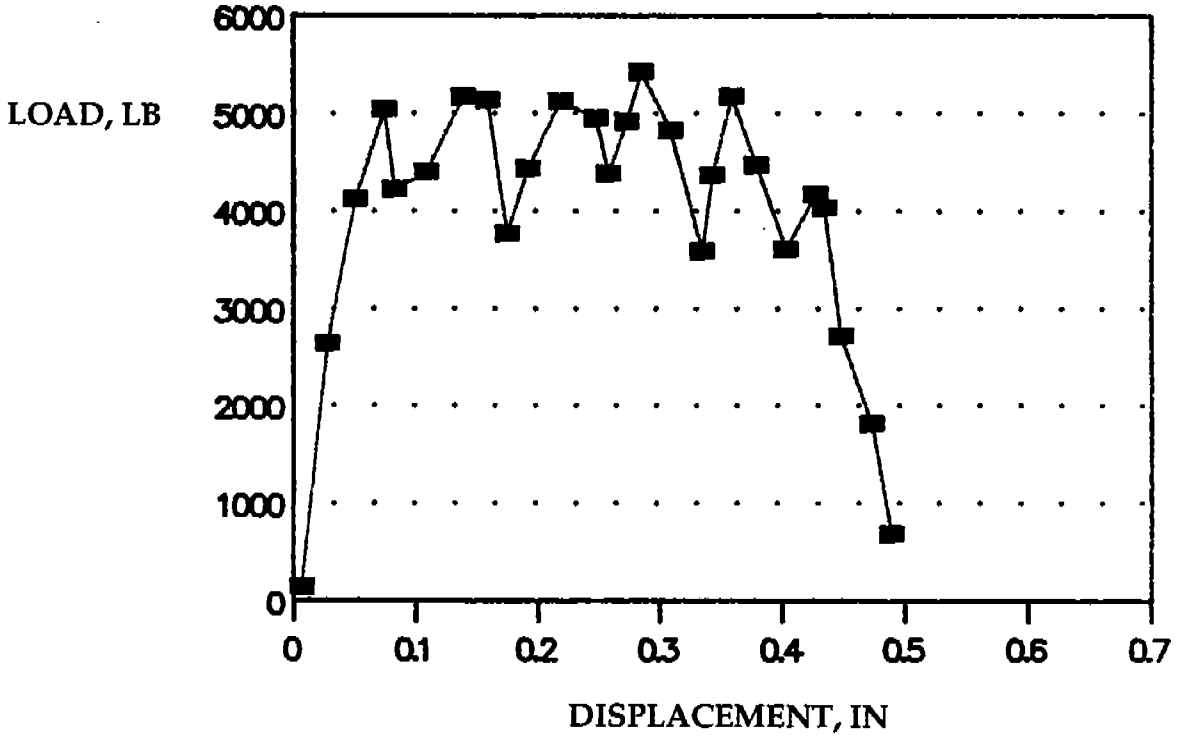

FIGURE 2.6 Load elongation curve for A131 EH36 steel at 23°C. Strain rate = 280 s^{-1}

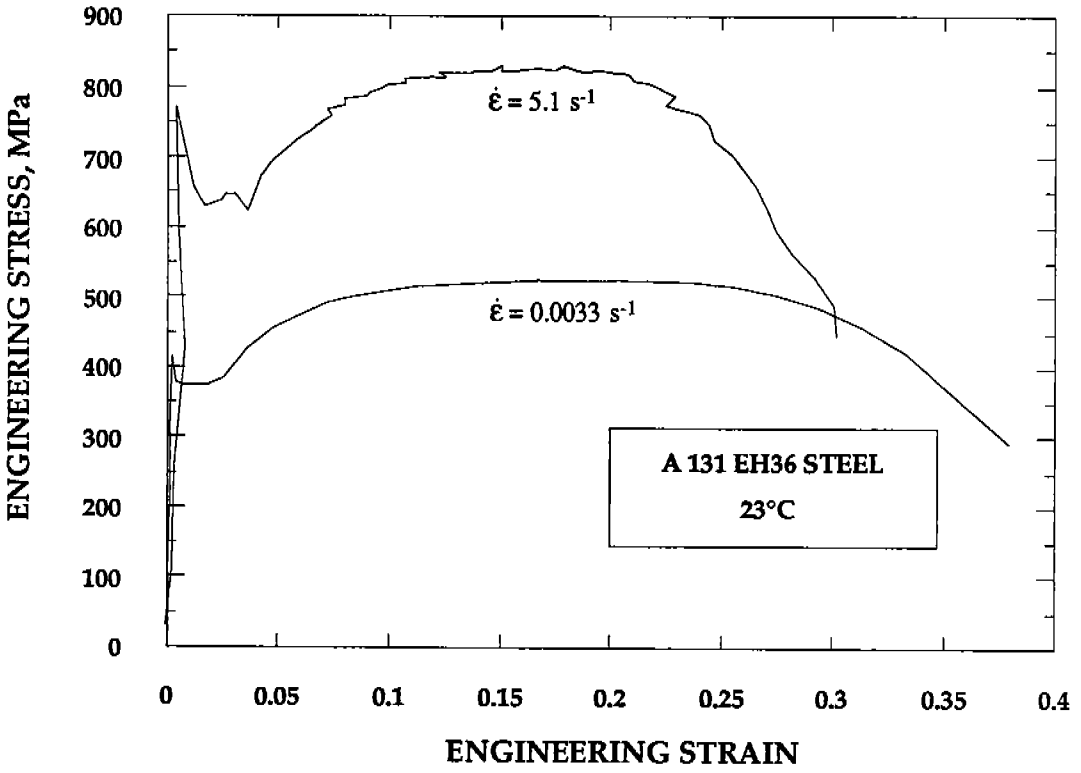

FIGURE 2.7 Effect of strain rate on flow behavior of A 131 EH36 steel at 23°C.

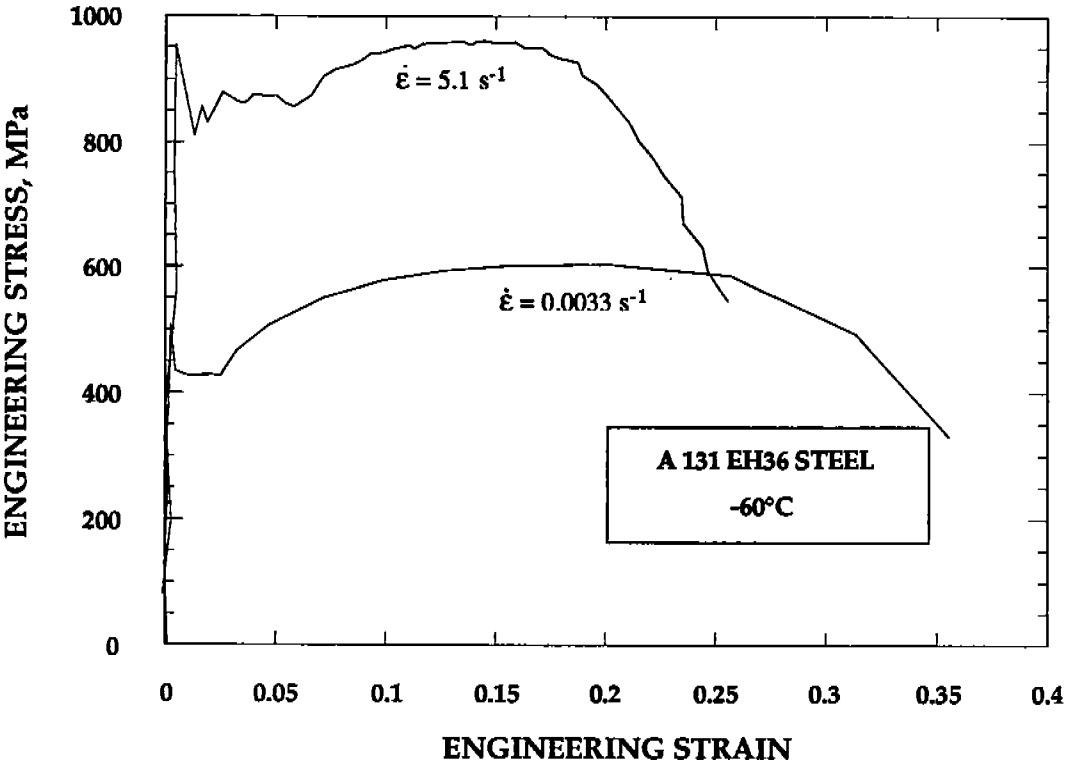

FIGURE 2.8 Effect of strain rate on flow behavior of A131 EH36 steel at -60°C.

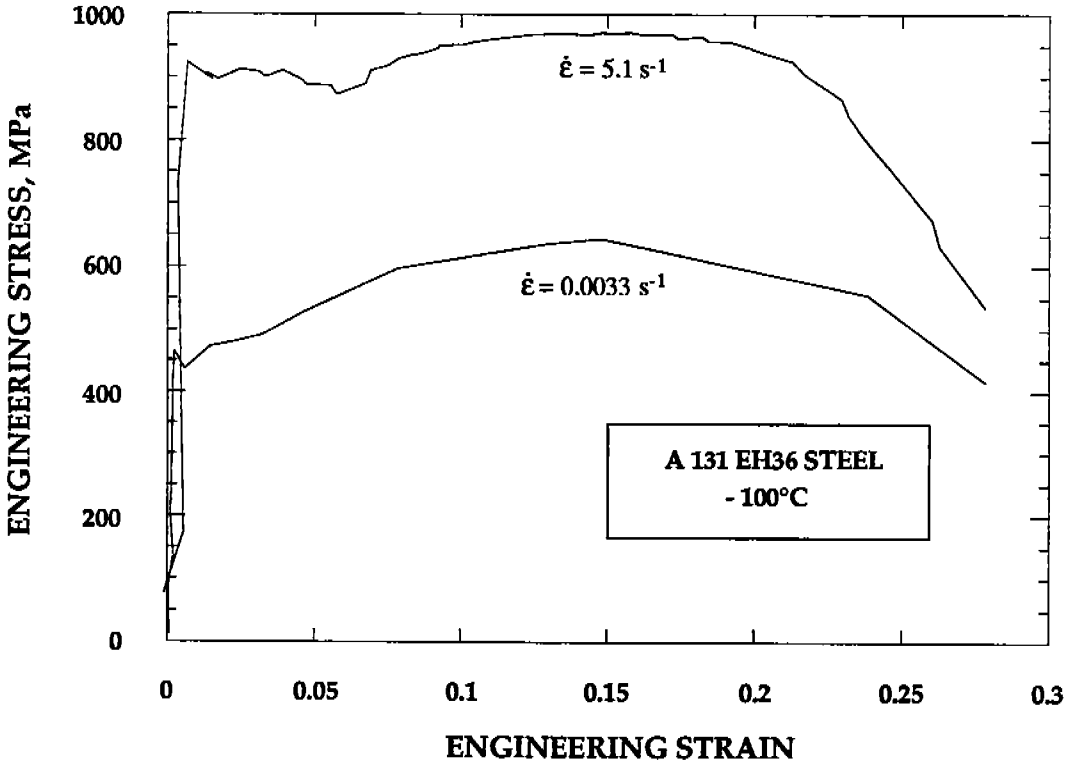

FIGURE 2.9 Effect of strain rate on flow behavior of A131 EH36 steel at -100°C.

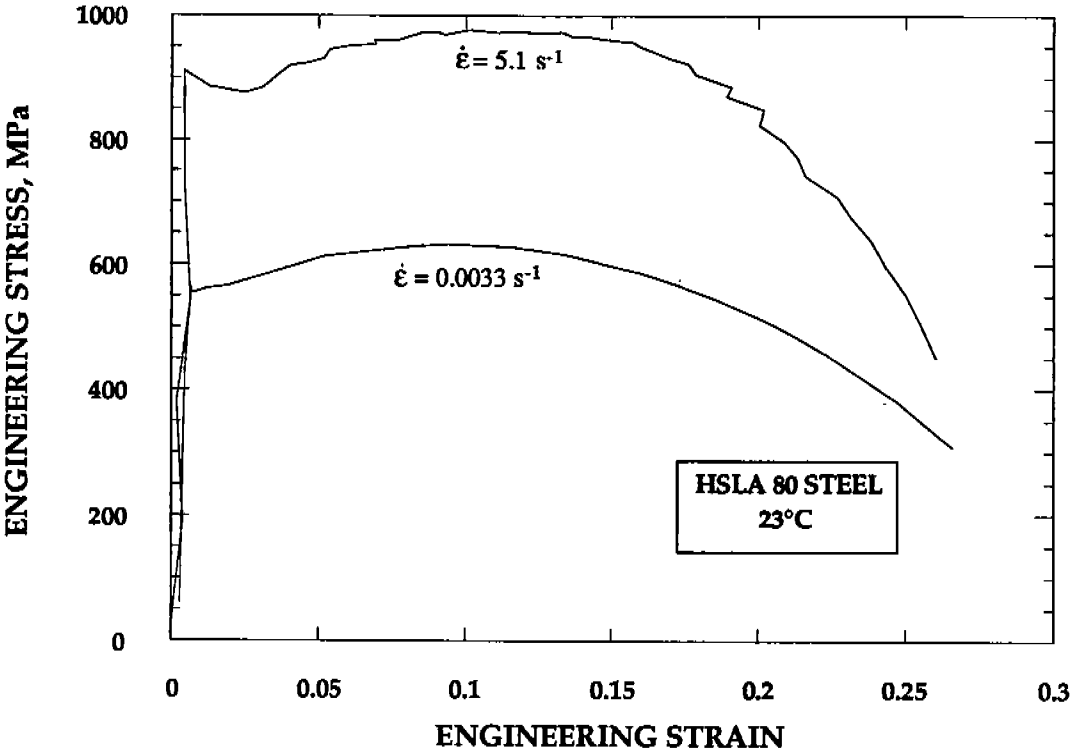

FIGURE 2.10 Effect of strain rate on flow behavior of HSLA 80 steel at 23°C.

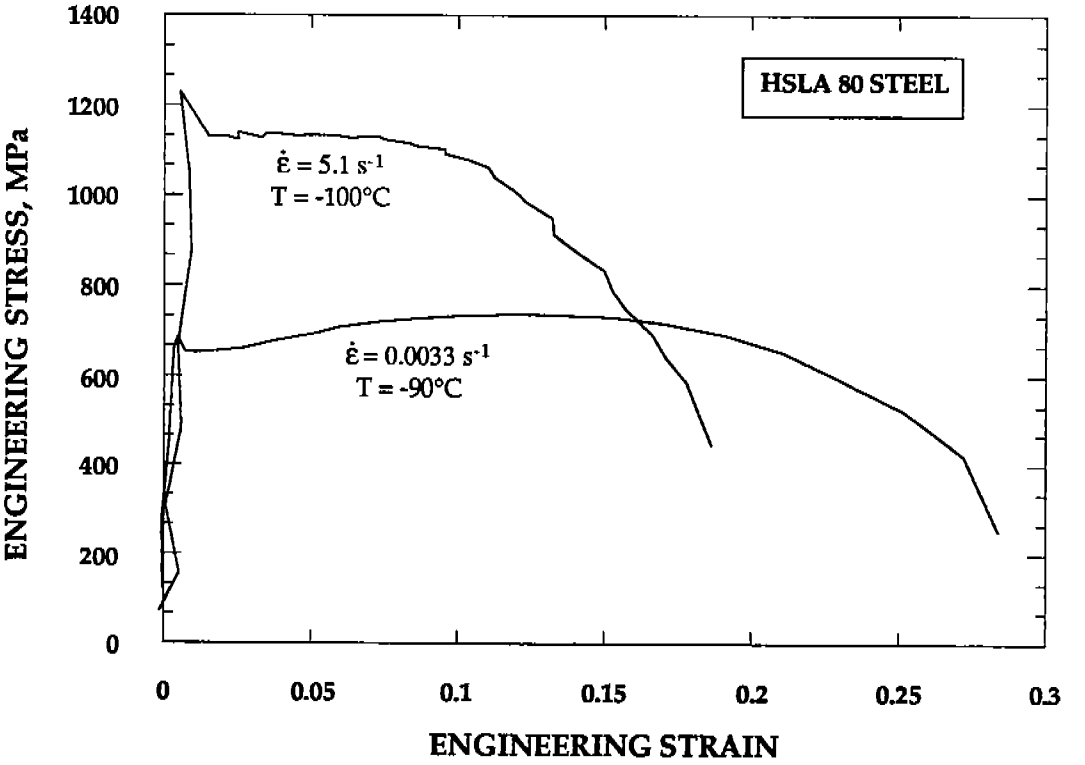

FIGURE 2.11 Effect of strain rate on flow behavior of HSLA 80 steel at low temperature.

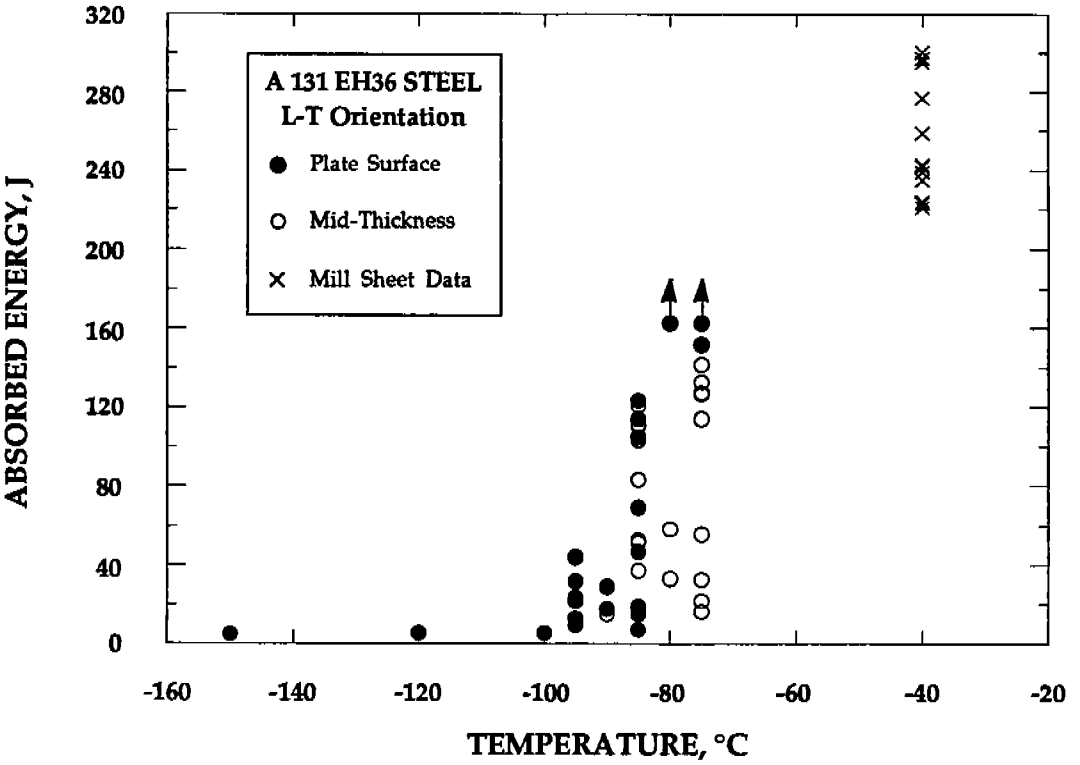

FIGURE 2.12 Charpy transition behavior of the A131 EH36 steel plate. L-T orientation.

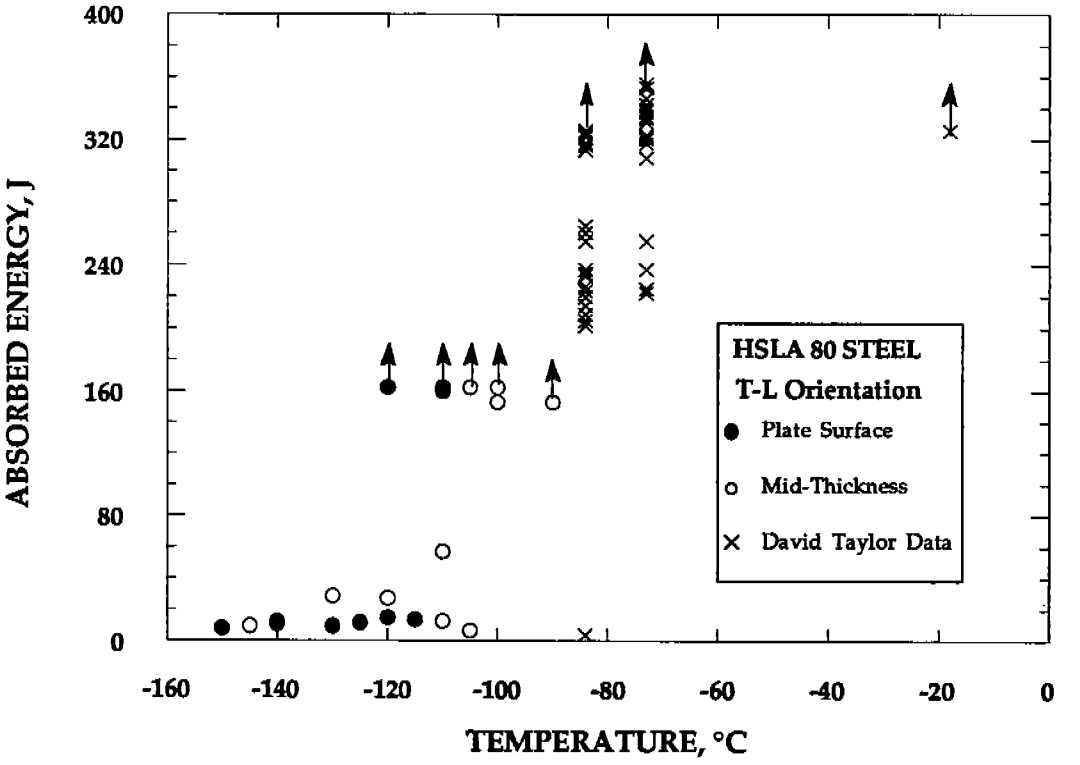

FIGURE 2.13 Charpy transition behavior of the HSLA 80 steel plate. T-L orientation.

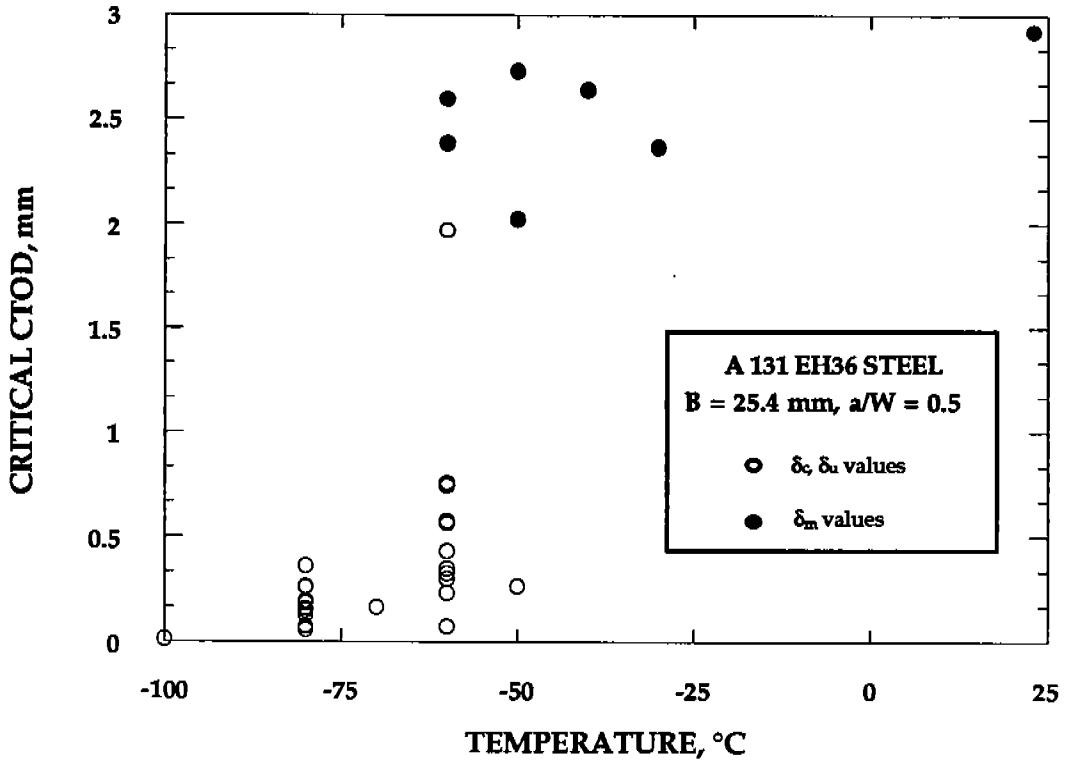

FIGURE 2.14 CTOD transition behavior of the A131 EH36 steel plate. L-T orientation.

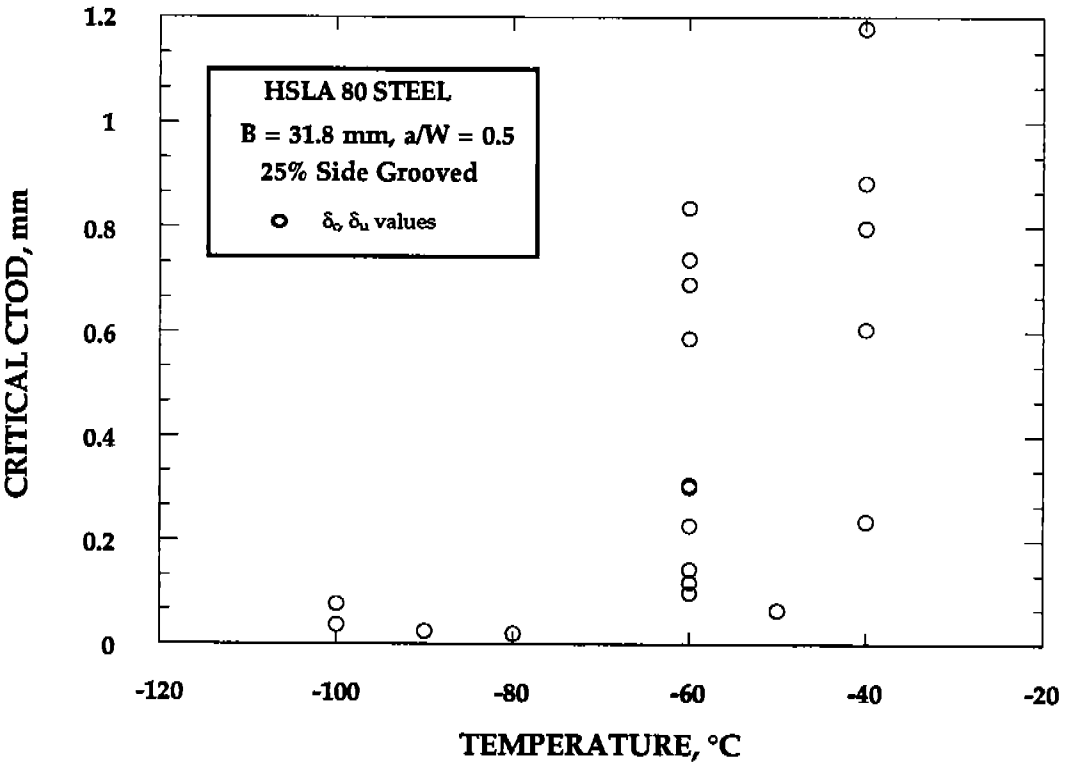

FIGURE 2.15 CTOD transition behavior of the HSLA 80 steel plate. T-L orientation.

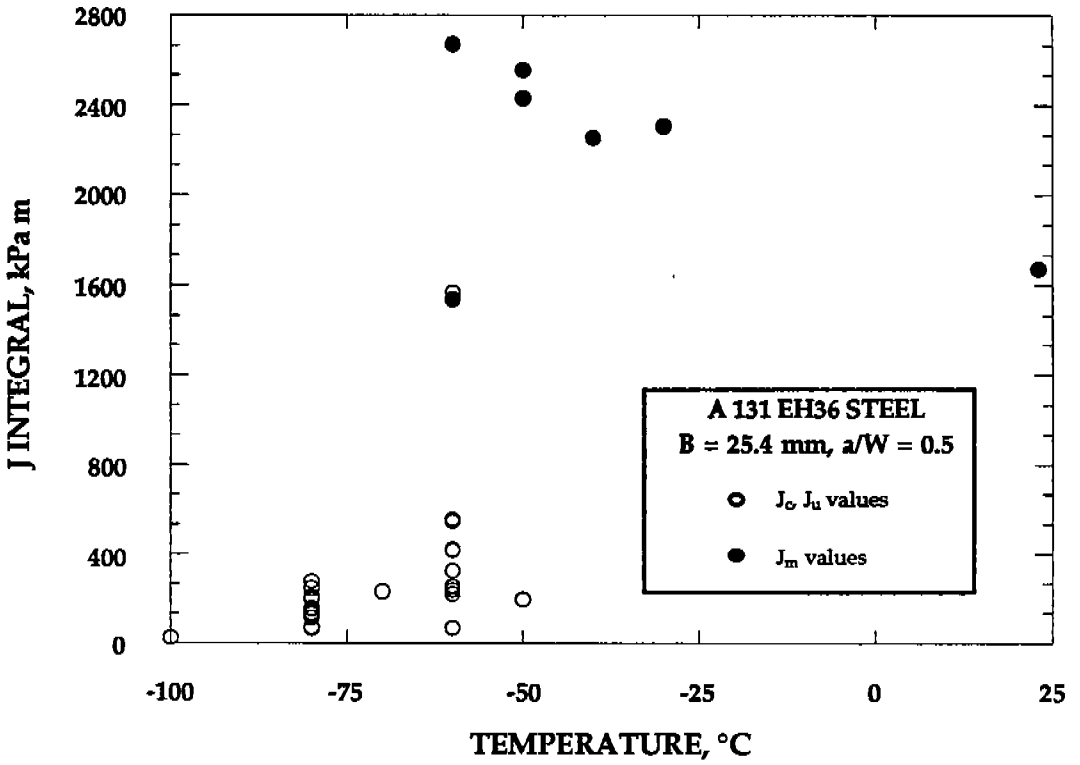

FIGURE 2.16 J integral transition behavior of the A131 EH36 steel plate. L-T orientation.

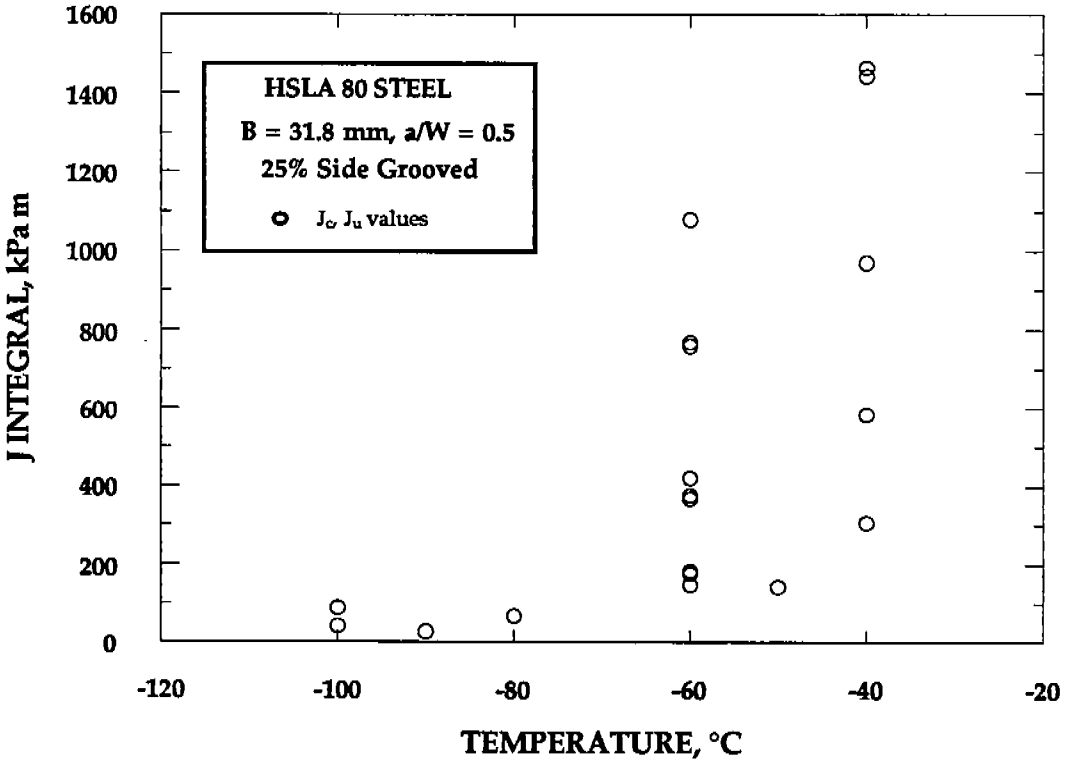

FIGURE 2.17 J integral transition behavior of the HSLA 80 steel plate. T-L orientation.

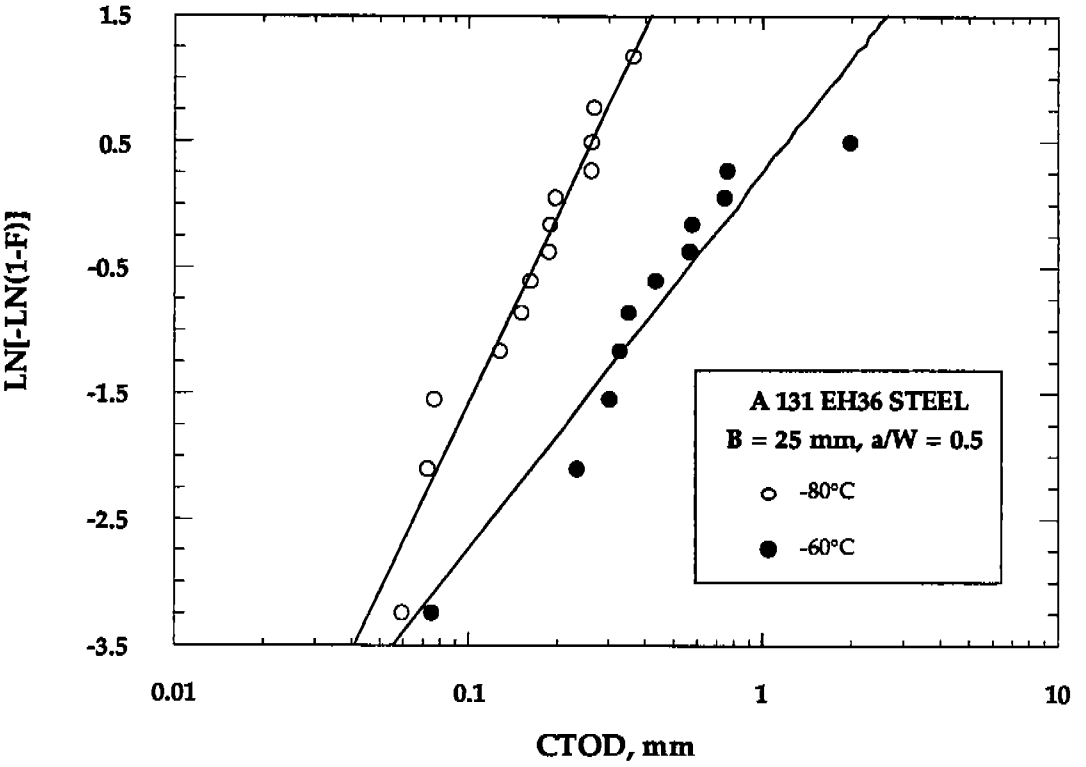

FIGURE 2.18 Weibull plot of CTOD data in the transition region for A 131 EH36 steel.

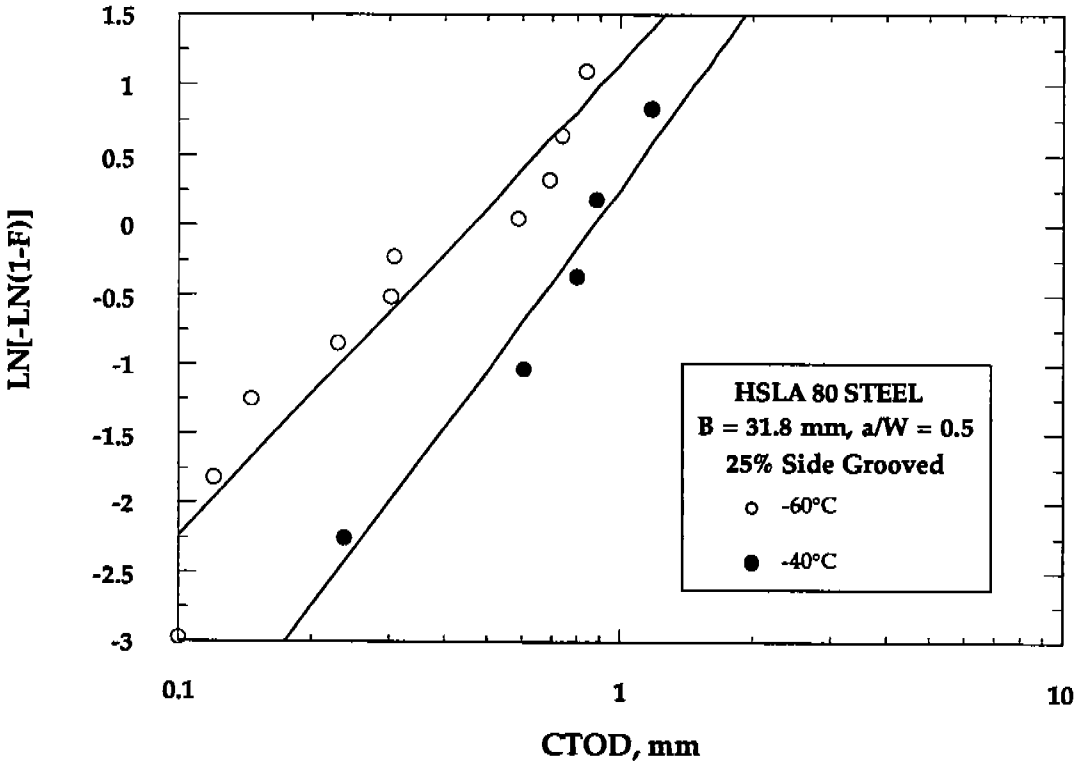

FIGURE 2.19 Weibull plot of CTOD data in the transition region for HSLA 80 steel.

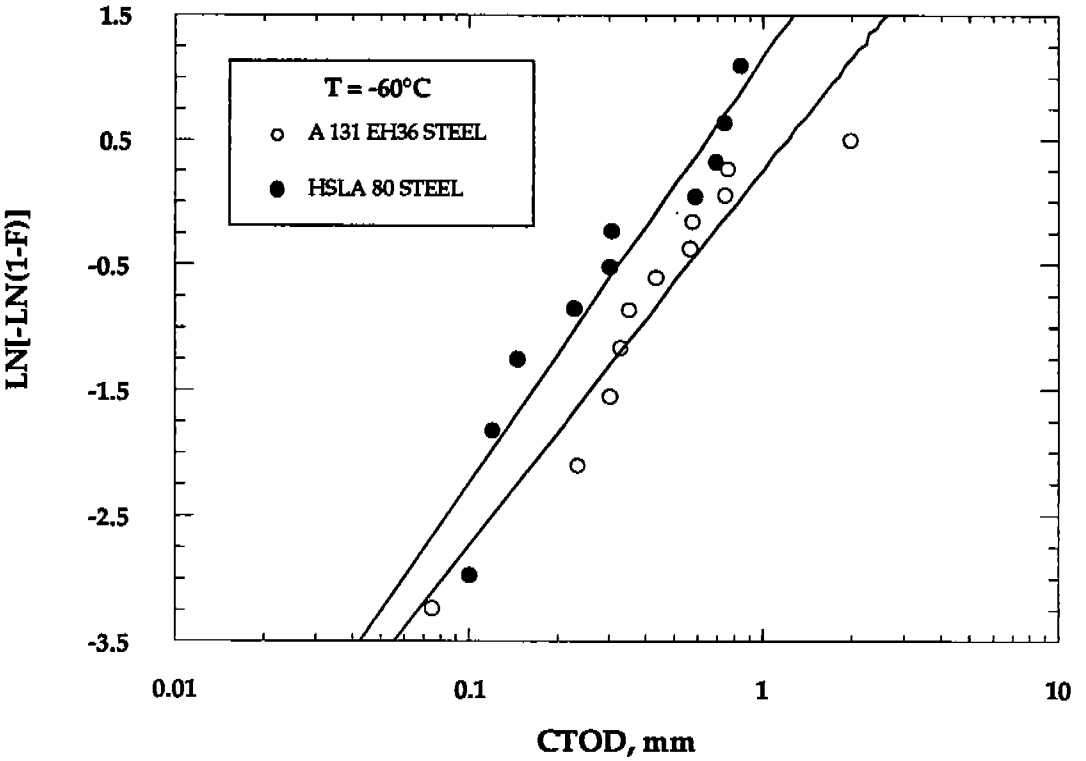

FIGURE 2.20 Weibull plot of CTOD data for both steels at -60°C.

3. SPECIMEN SIZE EFFECTS IN THE TRANSITION REGION

What follows is a summary of an analytical study of size effects on cleavage fracture toughness. Very detailed crack tip finite element analyses were performed by Professor R.H. Dodds Jr. as part of a separate investigation. In the present study, we utilized these results in conjunction with a local failure criterion to scale cleavage toughness with size. This section is very similar to an article that has been published separately [10].

3.1 SINGLE PARAMETER FRACTURE MECHANICS

One of the fundamental assumptions of fracture mechanics is that the crack tip conditions can be uniquely characterized by a single parameter such as the stress intensity factor (K) or the J integral. When this assumption is valid, the critical value of the crack tip parameter represents a size-independent measure of fracture toughness. The ASTM Standards for K_{IC} and J_{IC} testing [2,3] include minimum specimen size requirements which are designed to ensure a single parameter description of crack tip behavior. However, these standards are unsuitable for the transition region, as discussed below.

3.1.1 Existing Standards

The standard for K_{IC} testing [3] has very strict size requirements because the stress intensity factor is based on a linear elastic stress analysis; K is meaningless when there is significant crack tip plasticity. The size requirements in E 399-83 ensure that the crack tip plastic zone is small compared to specimen dimensions:

$$B, a \geq 2.5\left(\frac{K_{IC}}{\sigma_{YS}}\right)^2 \tag{3.1a}$$

$$0.45 \leq a/W \leq 0.55 \tag{3.1b}$$

where B is the specimen thickness, a is crack length, W is width, and σ_{YS} is the 0.2 % offset yield strength. The requirements in Eq. (3.1) restrict the K_{IC} test to brittle

materials or very large specimens. In the case of most structural steels, valid K_{IC} tests are only possible on the lower shelf of toughness.

The size requirements in E 813 [4] are much more lenient than E 399, primarily because the J integral is better suited to nonlinear material behavior. The minimum specimen dimensions for a valid J_{IC} result are as follows:

$$B, b \geq \frac{25 J_{IC}}{\sigma_Y} \tag{3.2}$$

where b is the uncracked ligament length (W-a) and σ_Y is the flow stress, defined as the average of the yield and tensile strength. The J_{IC} test measures a critical J near the onset of stable crack growth; E 813 is not valid when the specimen fails in an unstable manner. Thus E 813 cannot be used to quantify fracture toughness in the ductile-brittle transition region of steels, where the primary failure mechanism is cleavage. While Eq. (3.2) has been shown to be sufficient to guarantee nearly size-independent J_{IC} values for initiation of ductile tearing, this requirement is inappropriate for cleavage toughness, which is more sensitive to specimen size [12].

The only ASTM Standard that permits fracture toughness testing in the transition region is E 1290-89, the *Standard Test Method for Crack-Tip Opening Displacement (CTOD) Fracture Toughness Measurement* [5]. The CTOD test applies to all micromechanisms of failure in metals, but there are no minimum specimen size requirements. The lack of size requirements in this standard is consistent with the pragmatic philosophy of the CTOD design curve approach developed in the United Kingdom [6,7]. This approach, which is usually applied to welded steel structures, concedes that critical CTOD values may vary with size and geometry, but states that CTOD data can be applied to fitness-for-purpose assessments if the test specimens possess at least as much crack tip constraint as the structure under consideration. The CTOD design approach recommends that the specimen thickness match the section thickness of the structure. The British CTOD testing standard [13] permits a/W ratios as small as 0.15, which facilitates weldment testing and allows shallow structural flaws to be simulated in the laboratory. Early drafts of the ASTM E 1290 included liberal tolerances on a/W, but these were deleted from the the final version.

3.1.2 Size Criteria for the Transition Region

The ductile-brittle transition region of structural steels is not adequately addressed by existing ASTM Standards. The K_{IC} test is not applicable because too much plastic deformation precedes failure in the transition region. The J_{IC} test is valid only on the upper shelf, while the CTOD standard does not guarantee a size-independent measure of fracture toughness.

There is a pressing need for rational specimen size criteria for the transition region. Such criteria are proposed in this chapter. The minimum specimen size for cleavage fracture to be characterized by J or CTOD was quantified by means of finite element analysis. These analyses also make it possible to predict the size dependence of fracture toughness when the single parameter assumption is no longer valid. Both shallow and deep notched specimens are considered, as well as a wide range of strain hardening behavior.

3.2 ANALYSIS PROCEDURES

This investigation utilized elastic-plastic finite element analysis to quantify the size dependence of cleavage fracture toughness and to develop size criteria for single parameter characterization. Crack tip stress fields obtained from specimens of finite size were compared to the corresponding stress fields for small scale yielding.

3.2.1 Relationship to Previous Work

Previous investigators, such as Shih and German [14] and McMeeking and Parks [15], used finite element analysis to develop specimen size criteria for J controlled fracture. Shih and German analyzed both bending and tension, and compared the computed stress fields with the Hutchinson, Rice and Rosengren (HRR) [16,17] singularity. Shih and German arbitrarily stated that the specimen was J controlled if the computed stresses near the crack tip were within 10% of the HRR solution. Shih and Hutchinson [18] later applied this same approach to derive size criteria for combined loading, ranging from pure tension to pure bending.

The procedure employed in the present study differs from the Shih and German approach in two major respects. First, the crack tip stresses in finite size specimens are compared to the actual small scale yielding stress fields rather than the HRR singularity, which only applies to a limited region ahead of the crack tip. The

other main difference in the present approach is that the micromechanism of fracture is considered when quantifying the size dependence of fracture toughness. An arbitrary criterion based on 10% deviation in stress from small scale yielding is not appropriate for stress-controlled cleavage fracture, because even a slight deviation in stress can result in a significant elevation of the critical J value [12]. In the present study, the size dependence of cleavage toughness is computed directly; the proposed size requirements ensure that the measured fracture toughness is nearly equal to the toughness in small scale yielding.

3.2.2 Finite Element Analysis

Plane strain elastic-plastic finite element analysis was performed on four configurations with three strain hardening rates, resulting in a total of twelve cases (see Table 3.1). The crack tip stress fields for small scale yielding were evaluated, as well as single edge notched bend (SENB) specimens with a/W ratios of 0.05, 0.15, and 0.50. The material stress-strain behavior was modeled with a Ramberg-Osgood power law expression:

$$\frac{\varepsilon}{\varepsilon_0} = \frac{\sigma}{\sigma_0} + \alpha\left(\frac{\sigma}{\sigma_0}\right)^n \tag{3.3}$$

where ε is strain, σ is stress, σ_0 is a reference stress, $\varepsilon_0 = \sigma_0/E$, and α and n are dimensionless constants. For the present study, $\alpha = 1.0$, $\varepsilon_0 = 0.002$, and $\sigma_0 = 60$ ksi (414 MPa); in this case σ_0 corresponds to the 0.2% offset yield strength, σ_{YS}. The strain hardening exponent, n, was assigned values of 5, 10 and 50, which correspond to high, medium and low work hardening, respectively.

Figure 3.1 shows a schematic of the model that was used for the small scale yielding analyses. The circular domain with a crack reduces to a semicircle because of symmetry. The finite element mesh contains 720 elements and 2300 nodes. The mesh was scaled geometrically in order to concentrate elements and nodes near the crack tip. Linear elastic stress intensity factors were imposed at the boundary of the domain; in all cases the value of the imposed K was sufficiently low to confine the plastic zone to the domain. This model is designed to simulate a crack in an infinite body; McMeeking and Parks [15] were among the first to apply this approach to crack tip stress analysis.

Finite element meshes of SENB specimens were generated with a/W = 0.05, 0.15, 0.50. Each of these meshes contained approximately 350 elements and 1200 nodes, with most of the elements and nodes concentrated near the crack tip.

For each analysis, the J integral was evaluated by means of the energy domain integral approach [19]. The CTOD was defined as the intersection of the crack flanks with a 90° vertex emanating from the crack tip.

Additional details of the finite element analysis are given in Reference [20].

3.2.3 Cleavage Fracture Criterion

Under small scale yielding conditions, the crack tip stresses and strains are uniquely characterized by J, and the onset of fracture is uniquely defined by a critical value of J, irrespective of the micromechanism of failure. When J dominance is lost, the stresses and strains no longer increase in proportion to one another, and critical J values are size dependent. The magnitude of this size dependence depends on the micromechanism of failure. For example, a material which fails when a critical strain is reached locally would exhibit a different fracture toughness size dependence from a material that fails at a critical local stress.

In order to quantify size effects on fracture toughness, one must assume a local failure criterion. In the case of cleavage fracture, a number of micromechanical models have recently been proposed [21-24], most based on weakest-link statistics. The weakest-link models assume that cleavage failure is controlled by the largest or most favorably oriented fracture-triggering particle. The actual trigger event involves a local Griffith instability of a microcrack which forms from a microstructural feature such as a carbide or inclusion; the Griffith energy balance is satisfied when a critical stress is reached in the vicinity of the microcrack. The size and location of the critical microstructural feature dictate the fracture toughness; thus cleavage toughness is subject to considerable scatter [24].

The Griffith instability criterion implies fracture at a critical normal stress near the tip of the crack; the statistical sampling nature of cleavage initiation (i.e., the probability of finding a critical microstructural feature near the crack tip) suggests that the volume of the process zone is also important. Thus the probability of cleavage fracture in a cracked specimen can be expressed in the following general form:

$$F = F(\sigma_1, V(\sigma_1)) \tag{3.4}$$

where F is the failure probability, σ_1 is the maximum principle stress at a point, and $V(\sigma_1)$ is the cumulative volume sampled where the principal stress $\geq \sigma_1$. Equation (3.4) is sufficiently general to apply to any fracture process controlled by maximum principal stress, not just weakest link failure. For a specimen subjected to plane strain conditions, V = BA, where A is cumulative area on the x-y plane. (This report uses the conventional fracture mechanics coordinate axis, where x is the direction of crack propagation, y is normal to the crack plane, and z is parallel to the crack front.) For small scale yielding, dimensional analysis shows that the principal stress ahead of the crack tip can be written as

$$\frac{\sigma_1}{\sigma_o} = g\left(\frac{J}{\sigma_o r}, \theta\right) \tag{3.5a}$$

or

$$\frac{\sigma_1}{\sigma_o} = h\left(\frac{J^2}{\sigma_o^2 A}\right) \tag{3.5b}$$

where r is the radial distance from the crack tip and θ is the angle from the crack plane.

It can be shown that the HRR singularity is a special case of Eq. (3.5). When J dominance is lost, there is a relaxation in triaxiality; the principal stress at a fixed r and θ is less than the small scale yielding value (Eq. (3.5a)). Stated another way, the cumulative area for a given σ_1 is less than implied by Eq. (3.5b). However, it is possible to define an *effective J* that satisfies Eq. (3.5b):

$$\frac{J_{ssy}^2}{A} = \frac{J^2}{A_{ssy}} \quad \text{for a fixed } \sigma_1 \tag{3.6}$$

where J and A are the actual applied J integral and area in the specimen and A_{ssy} is the area which corresponds to J and σ_1 under small scale yielding conditions. The small scale yielding J value (J_{ssy}) can be viewed as *the effective driving force for cleavage.*

The procedure for determining J_{ssy} is illustrated schematically in Fig. 3.2. When the cumulative area ahead of the crack tip is normalized by the actual applied J, the large scale yielding curve lies below the small scale yielding curve. The lower curve is collapsed onto the upper curve when A is normalized by J_{ssy}.

The ratio J/J_{ssy} at the moment of fracture is a measure of the size dependence of cleavage fracture toughness. When the specimen is sufficiently large to maintain J controlled conditions, this ratio should equal 1.0.

3.3 RESULTS

3.3.1 Small Scale Yielding

Figures 3.3 to 3.5 show nondimensionalized plots of the stress normal to the crack plane for small scale yielding. The corresponding HRR solution is included on each plot for comparison. Elastic K values of 25 and 50 ksi $\sqrt{in}$ (27.6 and 55.2 MPa $\sqrt{m}$) were imposed in each case. The corresponding J values were computed from the finite element results and converted to equivalent K values, which are slightly lower than the elastic stress intensities; this discrepancy in applied and computed K values is caused by crack tip plasticity.

Although the finite element solutions do not agree with the HRR singularity except very near the crack tip, the computed stress fields scale with J/r, as expected from dimensional analysis (Eq. (3.5a)). The crack tip stress fields need not agree with the HRR solution for J controlled fracture; the precise functional relationship of the crack tip fields is unimportant as long as the stresses obey Eq. (3.5).

The crack tip fields in small scale yielding can be modeled by infinite series, where the HRR singularity is the leading term. This term dominates as $r \rightarrow 0$, but the asymptotic HRR solution is invalid for distances less than ~ 2 times the CTOD, because the crack tip fields are influenced by blunting and large strain effects. Thus there is a very limited region where the HRR solution applies; crack tip stress fields in finite specimens should be compared to the complete small scale yielding solution rather than the HRR singularity.

Figure 3.6 shows principal stress contours in nondimensional coordinates for small scale yielding with n = 10. This graph demonstrates that the principal stress scales with r/J at all angles (Eq. (5a); the areas bounded by the contours also scale, as predicted by Eq. (5b). Note that the contours have a similar shape, implying that that the small scale yielding stress fields can be written as the product of separable functions of r and θ:

$$\sigma_{ij} = c_{ij}\left(\frac{J}{\sigma_o r}\right) d_{ij}(\theta) \tag{3.7}$$

This relationship appears to hold for r values ranging from 2 to 20 times the CTOD.

3.3.2 SENB Specimens

Figure 3.7 compares the nondimensional principal stress contours for the small scale yielding solution with an SENB specimen with a/W = 0.5; the latter approximates small scale yielding behavior because it is loaded to a relatively low J value. Note that the contours coincide except for the sharp spike at $\theta = 45°$ in the SENB specimen. This slight difference in the shape of the contours is probably a mesh effect rather than a real phenomena; the finite element mesh for the small scale yielding analysis was approximately twice as refined near the crack tip as the SENB mesh. The areas bounded by the contours for the two cases agree to within 1%.

Figure 3.8a illustrates the effect of large scale yielding on nondimensional principal stress contours for n = 10 and a/W = 0.5. Although the contours maintain a constant shape, their size (when normalized by J) decreases with plasticity. (The *absolute size* of the contour actually increases with J, but at a slower rate than predicted from Eq. (3.5).) The equivalent small scale yielding J values, J_{ssy}, are chosen so that the contours coincide for a constant σ_1 (Fig. 3.8b).

Computed J_{ssy} values are plotted as a function of J and σ_1 in Fig. 3.9. The ratio J/J_{ssy} increases with J due to constraint loss. This ratio is insensitive to the principal stress; the deviation at high stress levels can be discounted because this is near the large strain region, where the accuracy of the finite element solution is suspect.

The nearly constant J/J_{ssy} ratio at a fixed J is an important result. Critical J values can be corrected for constraint loss be means of a single constant; the applied J and the J/J_{ssy} ratio completely characterize the principal stress distribution ahead of the crack tip.

3.3.3 Effect of Specimen Dimensions on J_c

Figures 3.10 to 3.12 illustrate the effect of crack length, a/W and hardening exponent on the J/J_{ssy} ratio. Since a critical value of J_{ssy} represents a size-independent cleavage toughness, the J/J_{ssy} ratio quantifies the geometry dependence of J_c, the measured fracture toughness. For the deeply notched specimens (a/W = 0.5), J_c approaches the small scale yielding value when the ratio $a\sigma_0/J$ is greater than ~200,

but the shallow notched specimens do not produce small scale yielding behavior unless the specimens are very large relative to J/σ_0. The relative crack tip constraint increases as strain hardening rate increases, i.e., as n decreases.

The effective driving force for cleavage, J_{ssy}, is plotted against the apparent driving force, J, in Figs. 3.13 to 3.15. The dashed line in each graph represents the small scale yielding limit, where $J = J_{ssy}$ by definition. Each of the curves in Figs. 3.13 to 3.15 agrees with the small scale yielding limit at low J values but deviates as J increases. The deviation from small scale yielding occurs more rapidly and at lower J values in shallow notched specimens and in low hardening materials. For n = 50 (Fig. 3.15), the effective driving force saturates at a constant value; further increases in J do not affect J_{ssy}. Once a specimen reaches the saturation value of J_{ssy}, the likelihood of cleavage fracture with further loading decreases considerably. Such a specimen could cleave only if the crack grew by ductile tearing and sampled a critical microstructural feature.

Figure 3.16 is a plot of J/J_{ssy} as a function of n and specimen size, which is normalized by flow stress in order to be consistent with the E 813 size criteria (Eq. (3.2)) and to reduce the effect of strain hardening on the size dependence. The flow stress for the Ramberg-Osgood materials was estimated from the following relationship:

$$\sigma_Y = \frac{\sigma_o}{2}\left[1 + \frac{\left(\frac{N}{0.002}\right)^N}{\exp(N)}\right] \tag{3.8}$$

where $N = 1/n$. Equation (3.8) was derived by solving for the tensile instability point in Eq. (3.3), converting true stress to engineering stress, and averaging σ_o and the estimated tensile strength. The J/J_{ssy} ratio becomes relatively flat and approaches 1.0 when the $a\sigma_Y/J$ ratio exceeds ~200, although the point at which each curve approaches the small scale yielding limit depends on the hardening exponent.

The effect of specimen size on critical CTOD is shown in Fig. 3.17. The curves for the three hardening exponents converge and approach $\delta/\delta_{ssy} = 1.0$ when the a/δ ratio is greater than ~ 300.

3.3.4 Effect of Thickness

All of the results presented so far are based on plane strain finite element analysis. When the specimen thickness is finite, however, the through-thickness constraint can be considerably less than plane strain.

Three-dimensional elastic plastic finite element analyses of flawed structures and test specimens are rarely performed because of the substantial computational requirements. Even rarer are three dimensional analyses with sufficient mesh refinement to analyze crack tip stresses. One such analysis, which was recently performed by Narishimhan and Rosakis [25], provides some insight regarding the thickness required to maintain nearly plane strain conditions. They analyzed an SENB specimen where the crack length and ligament length were three and six times the thickness, respectively; thus thickness was the governing dimension. The hardening exponent, n, was 22 in their analysis.

Figure 3.18, which was constructed from the results of Narishimhan and Rosakis, is a plot of stress normal to the crack plane, relative to the midthickness value. Three load steps are plotted, corresponding to $B\sigma_Y/J$ ratios of 235, 103, and 26.3. The relative distance ahead of the crack tip is in the range of 2 to 4 times the CTOD in each case. For the lowest J value, the stress is nearly constant except close to the free surface. At the intermediate load step, the stress is relatively constant through the middle 40% of the thickness. The stress at the highest J value varies continuously though the thickness.

Narishimhan and Rosakis did not report strain values, so it is not possible to state with certainty that the middle of the specimen is in plane strain at low and moderate J values. However, the crack tip stress fields at midthickness agree very closely with values obtained by Narishimhan and Rosakis from a two-dimensional plane strain analysis of the SENB specimen. Thus it is reasonable to assume that the midthickness principal stress corresponds to the plane strain value, at least for the two lowest J values in Fig. 3.18.

According to Fig. 3.18, an SENB specimen maintains nearly plane strain constraint through a significant portion of the thickness for $B\sigma_Y/J$ ratios up to 100. The size of the plane strain region can be defined as the *effective thickness*, which decreases as J increases.

In the case of cleavage fracture, there is a statistical thickness effect on fracture toughness, as first reported by Landes and Schaffer [26]. Because of the weakest link nature of cleavage initiation, a population of large specimens has a lower average

toughness than small specimens of the same material, because more material is sampled along the crack front in a large specimen and there is a higher probability of sampling a brittle region. Thus as constraint relaxes in a test specimen, the probability of cleavage fracture is influenced by the decrease in effective thickness.

3.3.5 Comparison with Experimental Data

Figures 3.10 to 3.17 provide the capability to correct cleavage fracture toughness for constraint loss. Given the measured toughness, specimen size, and material hardening characteristics it is possible to estimate the toughness of the specimen if its dimensions were infinite.

Fracture toughness data recently published by Sorem [27] were used in the present investigation to assess the ability of these analyses to characterize constraint loss. Sorem performed fracture toughness tests on SENB specimens of A 36 steel over a range of temperatures. The specimens were square section (B x B) with the thickness equal to 31.8 mm (1.25 in). Two aspect ratios were tested: a/W = 0.50 and a/W = 0.15. Since the material is a mild steel that exhibits a yield point, the flow behavior does not match the Ramberg-Osgood expression perfectly, but a slight deviation from the Ramberg-Osgood idealization should not affect the results significantly. Based on the σ_{TS}/σ_{YS} ratio and Eq. (3.8), we estimated n = 6 for this material.

Figure 3.19 shows CTOD data for the A 36 steel at two temperatures in the transition region. The solid diamonds represent the experimental data, while the crosses indicate predicted small scale yielding values. Every specimen but one (the highest CTOD value for a/W = 0.15 at -43°C) failed by cleavage without significant prior stable crack growth. At both temperatures, the shallow notched specimens have a higher apparent toughness than the deep notched specimens but the corrected values agree reasonably well. Relatively small corrections are needed for specimens with a/W = 0.50, but the small scale yielding correction has a major effect when a/W = 0.15. The small scale yielding CTOD values appear to be less scattered than the uncorrected data.

Figures 3.20 and 3.21 are Weibull plots of the A 36 data at - 76 and - 43°C, respectively. In both cases, there is a significant difference between the experimental data for a/W = 0.15 and 0.50, but the small scale yielding values are similar for the two geometries. At the higher temperature, the a/W = 0.15 data appear to be slightly over-corrected (or the a/W = 0.50 data are under-corrected), but this difference is not

statistically significant. The Weibull slopes in Figs. 3.20 and 3.21 increase when corrected for small scale yielding, indicating a decrease in scatter.

3.4 SPECIMEN SIZE REQUIREMENTS

Based on Figs. 3.16 to 3.18, we recommend the following specimen size limits for cleavage fracture in deeply notched bend specimens:

$$B, b, a \geq \frac{200\, J_c}{\sigma_Y} \tag{3.9}$$

or

$$B, b, a \geq 300\, \delta_c \tag{3.10}$$

These requirements, which should also apply to deeply notched compact specimens, guarantee fracture toughness results that are nearly size independent, but only when cleavage occurs without significant prior stable crack growth.

Equation (3.9) is eight times as severe as the size requirements in E 813-87 (Eq. (2)) but is not as severe as E 399-83 (Eq. (3.1)). Consider, for example, a material with J_c = 200 kPa m, σ_{YS} = 450 MPa, and σ_Y = 500 MPa. The minimum thickness required for a valid K_{IC} test is 570 mm (22.4 in), while a 10 mm (0.39 in) thick specimen would satisfy E 813-87. An 80 mm (3.15 in) thick specimen is required to satisfy Eq. (3.9).

It is very difficult (and sometimes impossible) to achieve J controlled fracture in shallow notched specimens, but the measured toughness can be corrected for constraint loss with Figs. 3.10 to 3.12. Figures 3.19 to 3.21 show that this approach successfully removed the geometry dependence of fracture toughness in A 36 steel.

This study focused primarily on the effect of in-plane dimensions on fracture toughness; the effect of thickness requires further study. Figure 3.18 shows that test specimens can maintain nearly plane strain conditions at midthickness to relatively high J values, but the size of the plane strain region decreases with plasticity. It should be possible to define an effective thickness, which equals the actual thickness for small scale yielding but decreases with J. The effective thickness can then be taken into account through statistical models for cleavage fracture [21-24].

The effect of prior ductile crack growth also requires further study. The results presented in this chapter apply only to stationary cracks. Ductile crack growth affects the cleavage toughness in at least two ways: (1) the crack tip stress field ahead of a

growing crack is undoubtedly different from that of a stationary crack; and (2) the growing crack samples more material than a stationary crack, increasing the likelihood of finding a critical cleavage trigger.

3.5 CONSTRAINT EFFECTS IN THE TWO SHIP STEELS

For the specimens tested in the present study, CTOD values greater than 0.085 mm fail the size restriction of Eq. (3.10). Thus, most of the data in the transition region for the two ship steels is affected by constraint loss.

Figures 3.22 and 3.23 are Weibull plots that compare experimental CTOD data for the EH36 and HSLA 80 steels with corresponding values corrected for constraint. At low toughness values, the constraint correction has a minimal effect on the data, but the constraint correction is significant at high toughness levels. The Weibull slope increases considerably when the constraint correction is applied to the data; scatter in fracture toughness data is greatly reduced when constraint effects are taken into account.

As stated earlier, the present analysis does not account for ductile crack growth. CTOD values in the upper transition region where corrected for constraint loss only. Further work is necessary to develop an appropriate correction for prior stable tearing.

3.6 STRUCTURAL APPLICATIONS

When the single parameter assumption of fracture mechanics is valid, fracture toughness values determined from laboratory specimens are transferable to structures. In most practical situations,however, the single parameter assumption is invalid either for the test specimen, the structure, or both.

The analysis presented in this section provides a framework for predicting fracture in structures when the test specimen and/or structure experience a loss in constraint. A critical value of J_{ssy} represents a size-independent measure of fracture toughness. Therefore, although a structure and test specimen may not fail at the same critical J value, they should fail at the same critical Jssy.

Figure 3.24 schematically illustrates how the behavior of a structure could be predicted from a laboratory specimen. The effective driving force for cleavage, J_{ssy}, is plotted against J, as in Figs. 3.13 to 3.15. Since both the structure and the test specimen should fail at the same value of *effective* driving force, a J_c value from a

laboratory test specimen could be used to predict the J_c in the structure, given a plot such as Fig. 3.24. The J_{ssy} - J relationship for the structure could be obtained from finite element analysis in conjunction with a stress-based failure criterion.

A major difficulty with this approach is that it would be necessary to perform detailed numerical analyses on each structural configuration of interest. Various flaw sizes and orientations would have to be modeled, resulting in an overwhelming number of complex analyses.

TABLE 3.1 Matrix of finite element solutions.

Geometry:	Hardening Exponent:		
	n = 5	n = 10	n = 50
Small Scale Yielding	X	X	X
a/W = 0.50	X	X	X
a/W = 0.15	X	X	X
a/W = 0.05	X	X	X

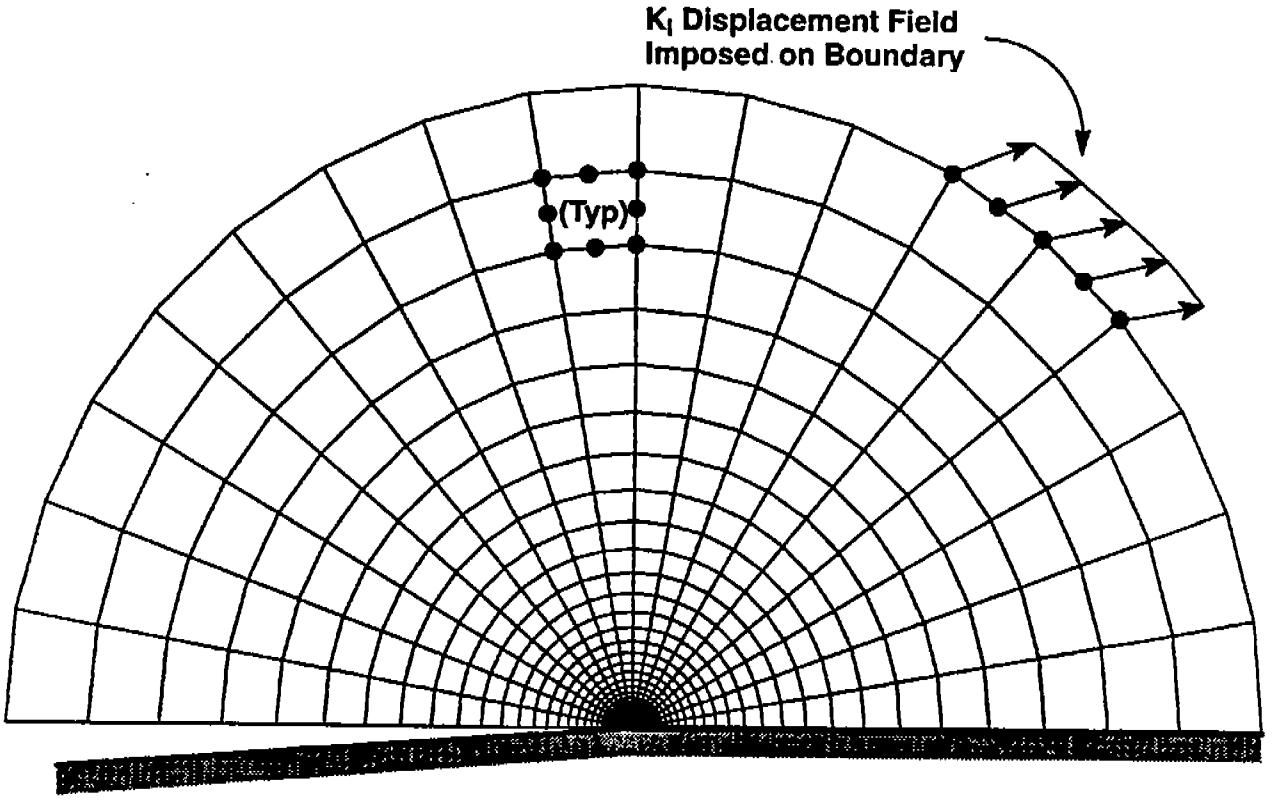

FIGURE 3.1 Finite element mesh used for the small scale yielding analysis (720 elements, 2277 nodes).

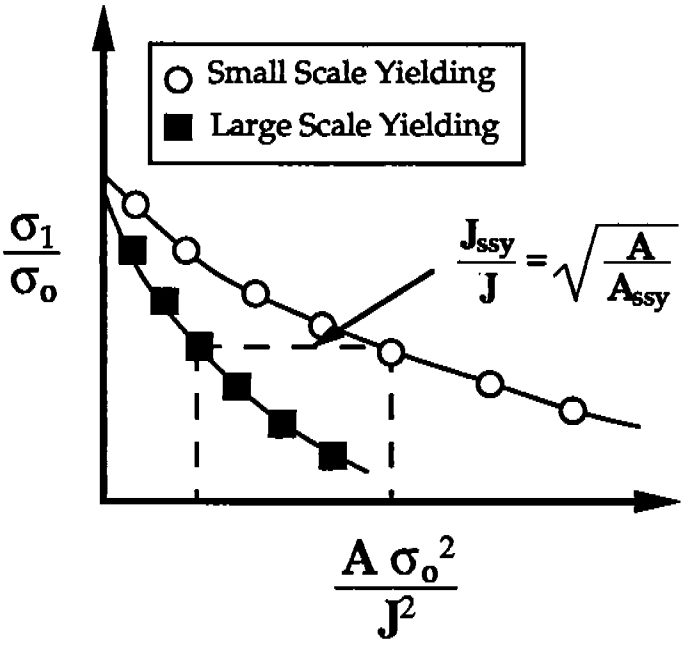

(a)

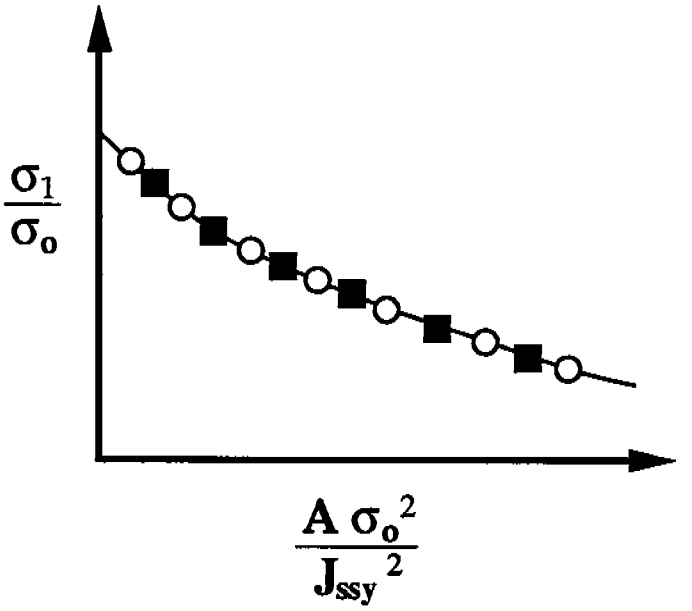

(b)

FIGURE 3.2 Definition of the effective small scale yielding J integral, J_{ssy}.

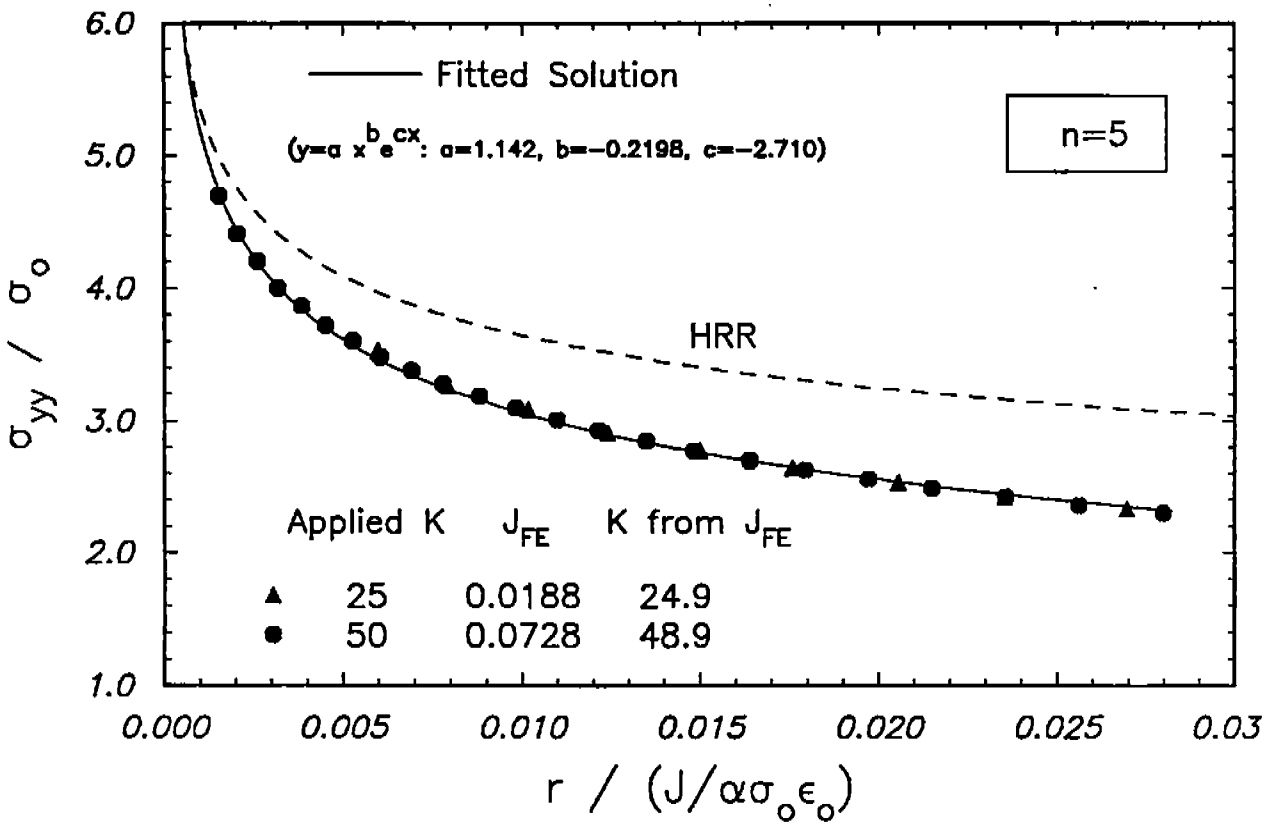

FIGURE 3.3 Stress normal to the crack plane in small scale yielding for n = 5.

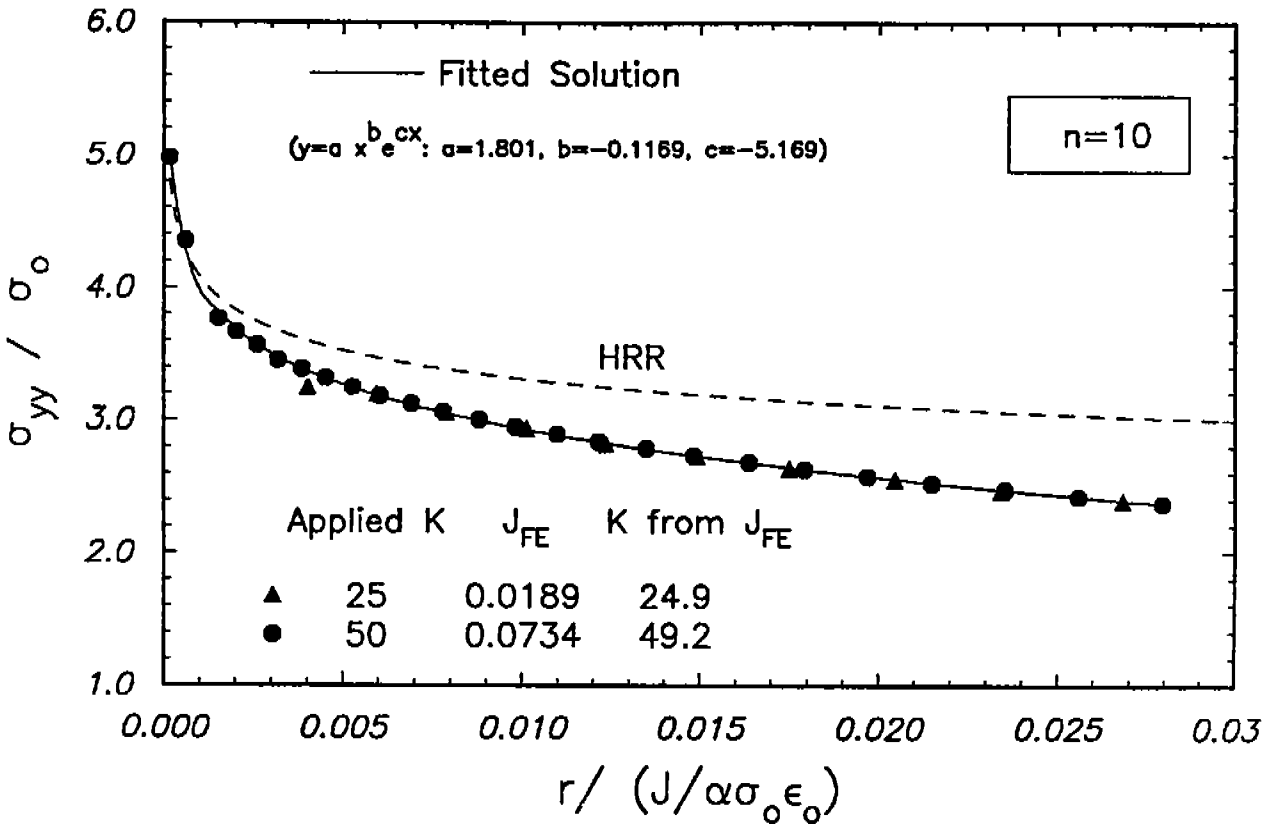

FIGURE 3.4 Stress normal to the crack plane in small scale yielding for n = 10.

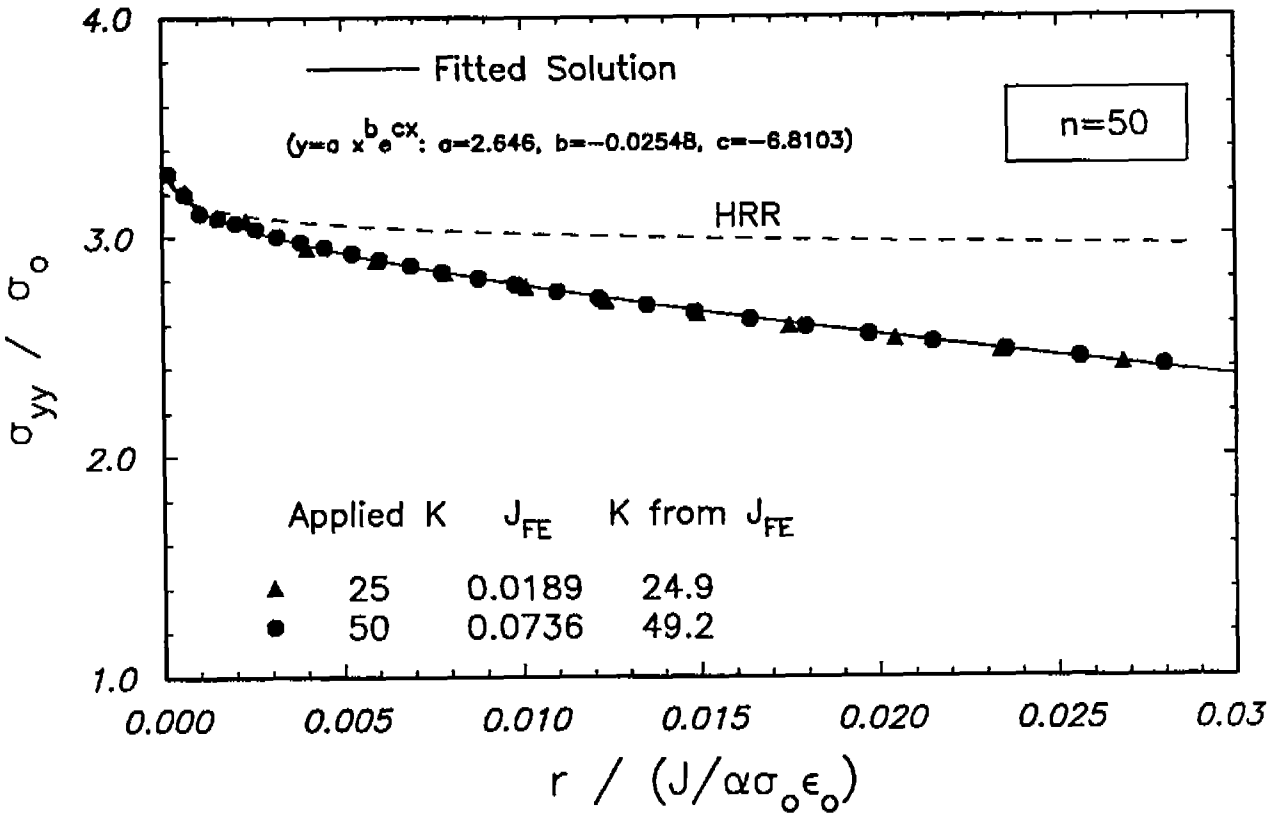

FIGURE 3.5 Stress normal to the crack plane in small scale yielding for n = 50.

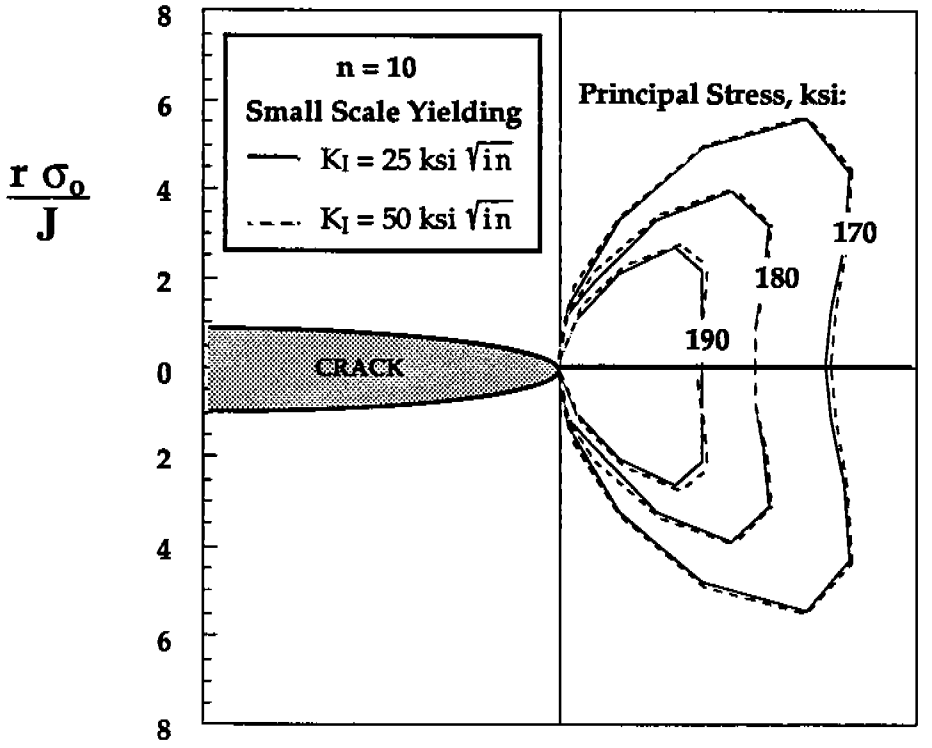

FIGURE 3.6 Maximum principal stress contours ahead of a crack in small scale yielding for n = 10.

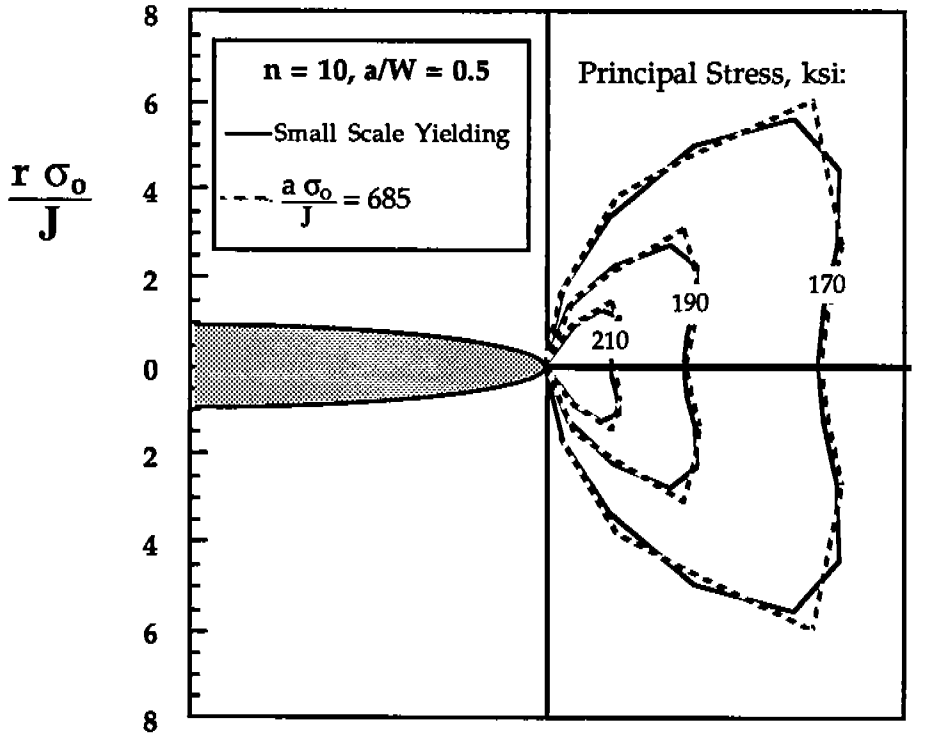

FIGURE 3.7 Comparison of principal stress contours in small scale yielding and in an SENB specimen with a/W = 0.5 and $a\sigma_o/J$ = 665.

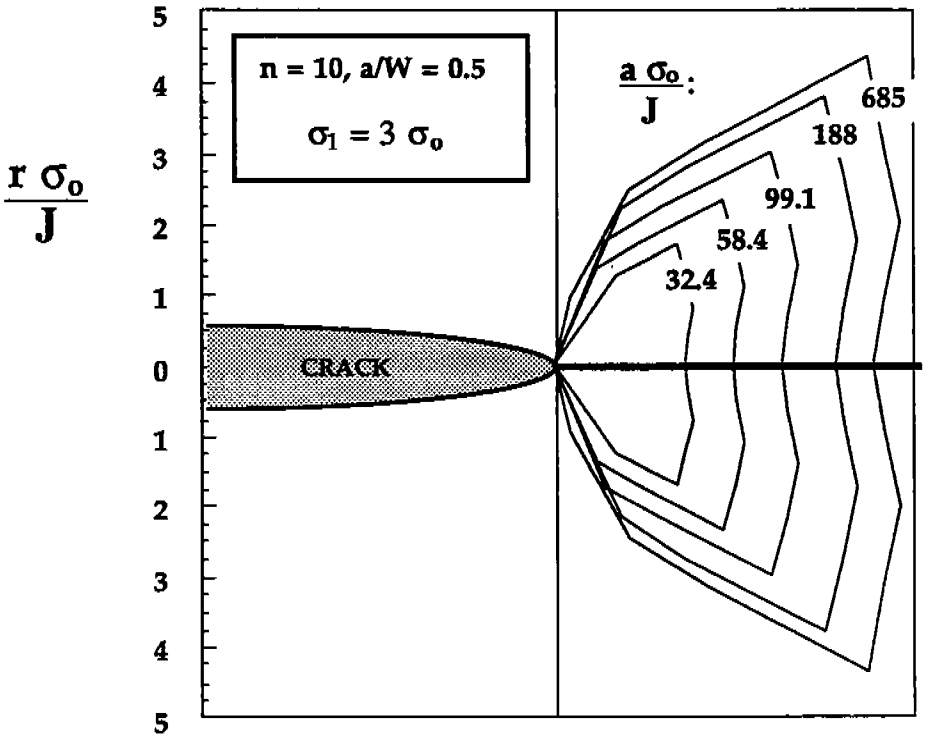

(a) Normalized by J

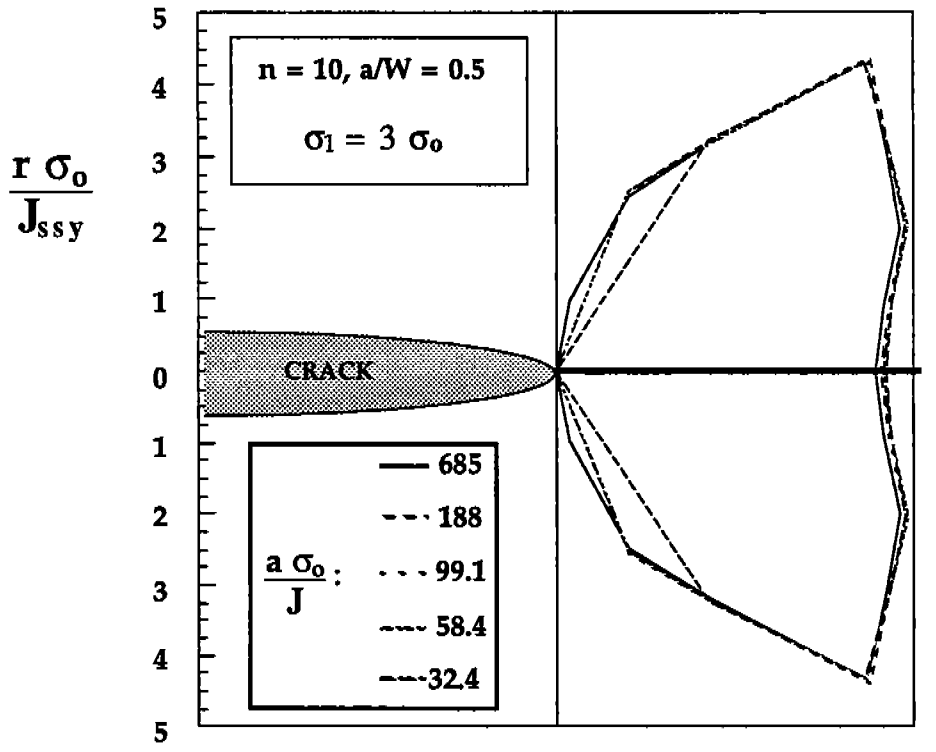

(b) Normalized by Jssy.

FIGURE 3.8. Principal stress contours for n = 10 and a/W = 0.5.

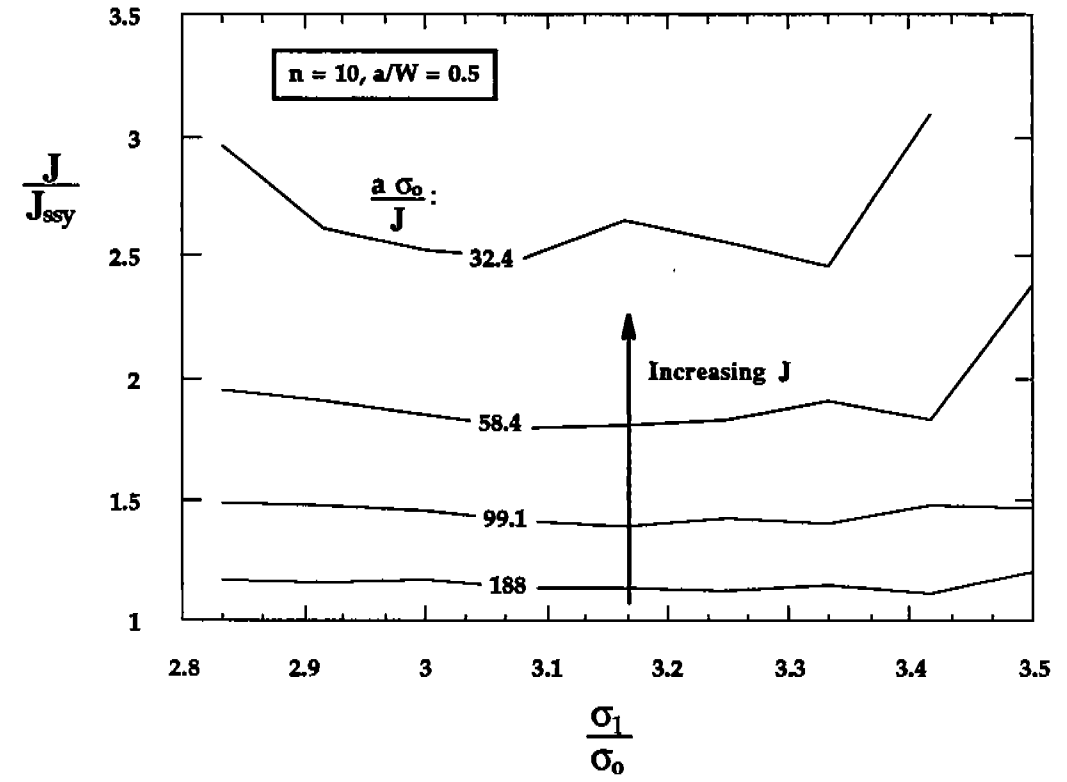

FIGURE 3.9 Effect of principal stress on the computed J/J_{ssy} ratio.

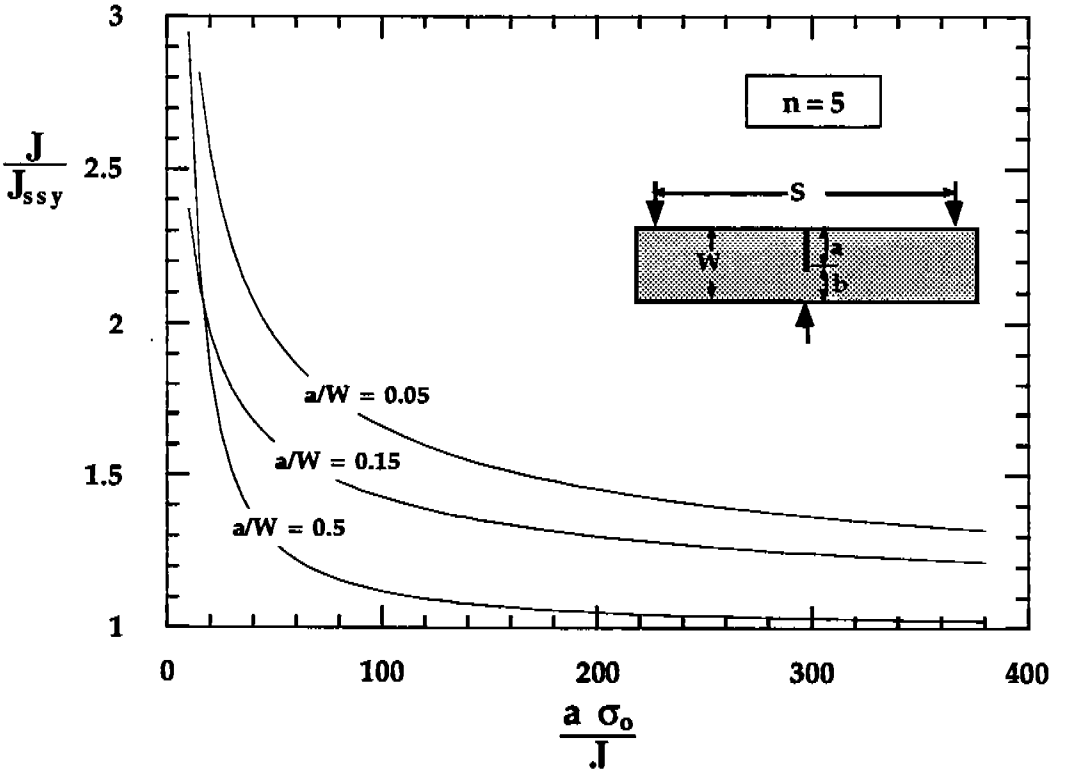

FIGURE 3.10 Effect of crack length and a/W on the J/J_{ssy} ratio for n = 5.

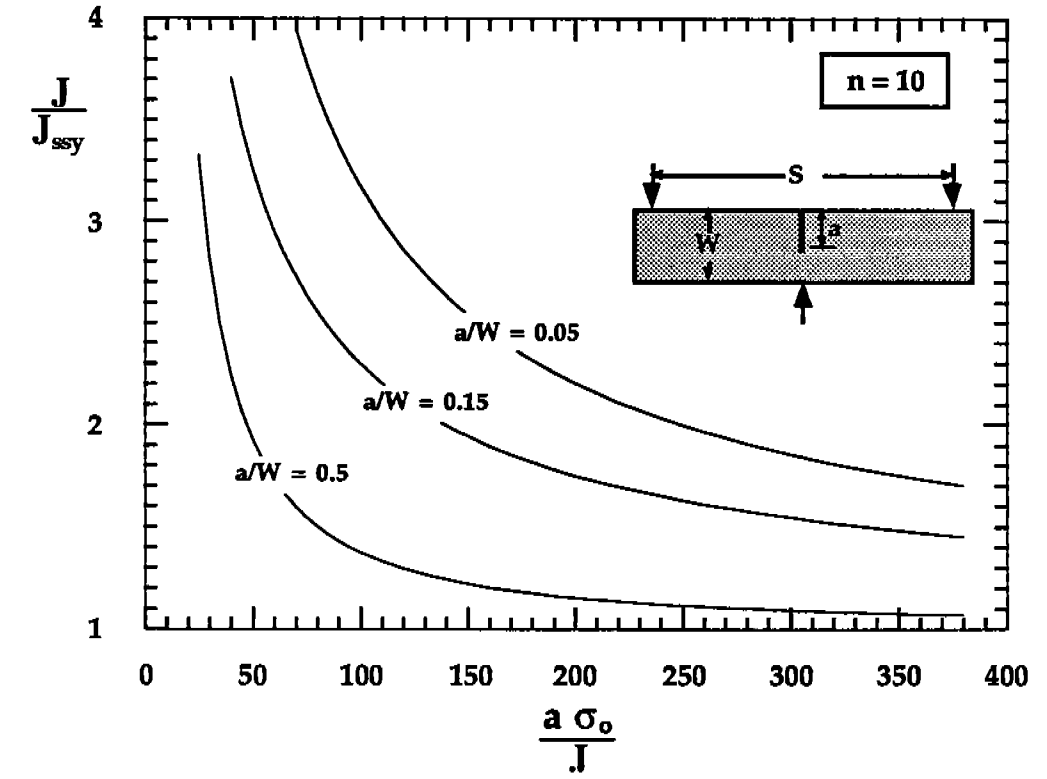

FIGURE 3.11 Effect of crack length and a/W on the J/J_{ssy} ratio for n = 10.

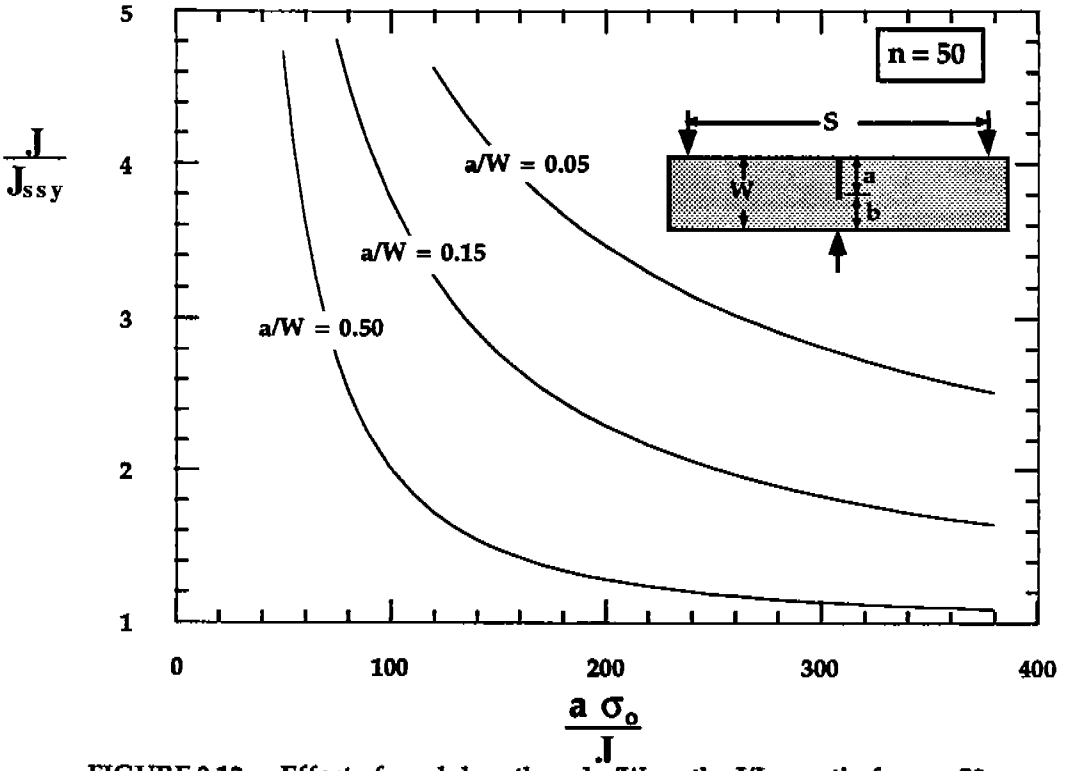

FIGURE 3.12 Effect of crack length and a/W on the J/J_{ssy} ratio for n = 50.

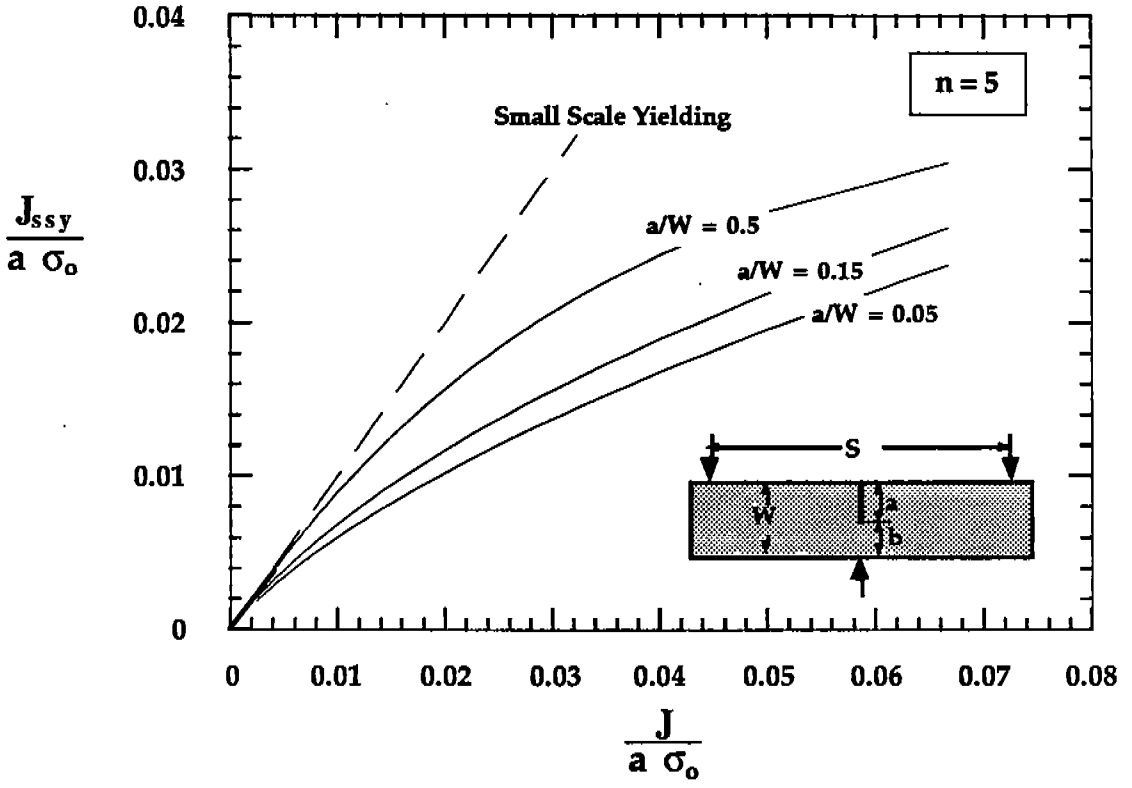

FIGURE 3.13 Comparison of effective and apparent driving force for n = 5

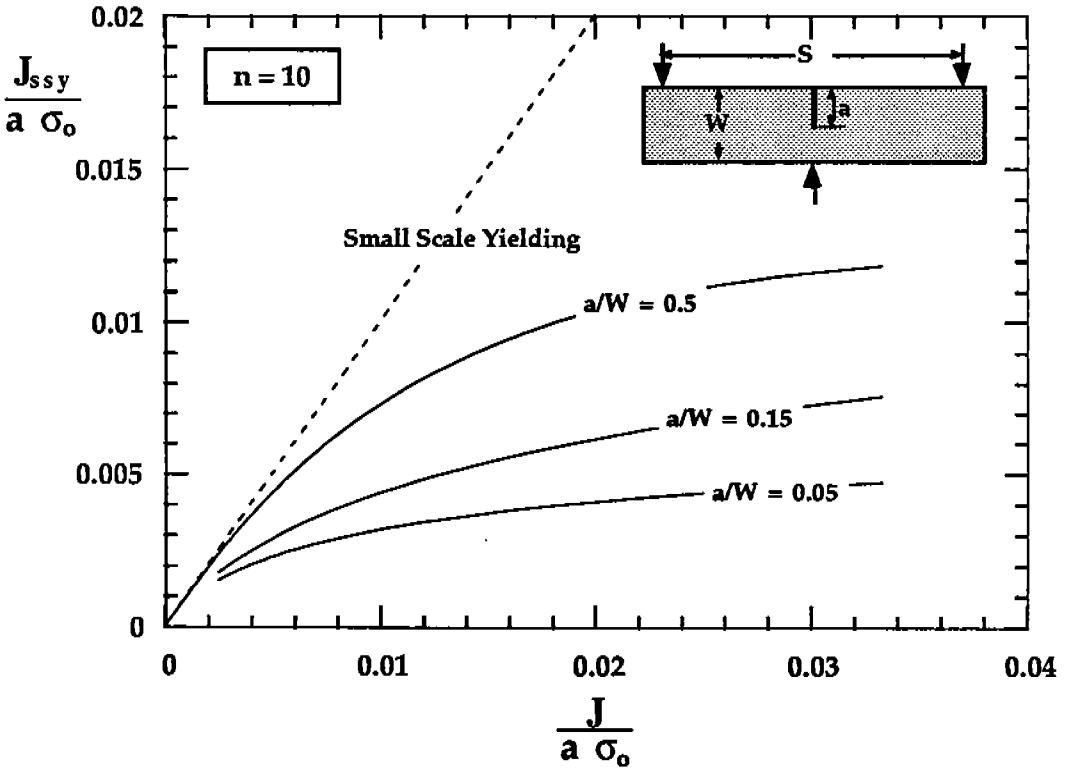

FIGURE 3.14 Comparison of effective and apparent driving force for n = 10

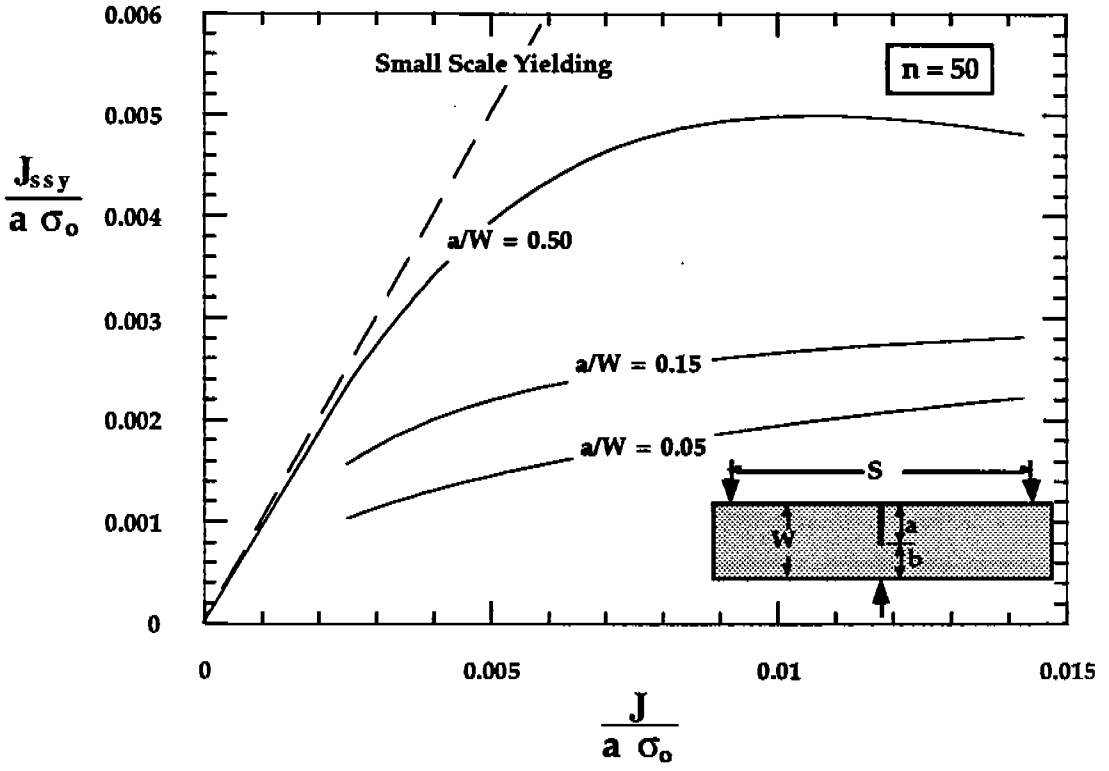

FIGURE 3.15 Comparison of effective and apparent driving force for n = 50

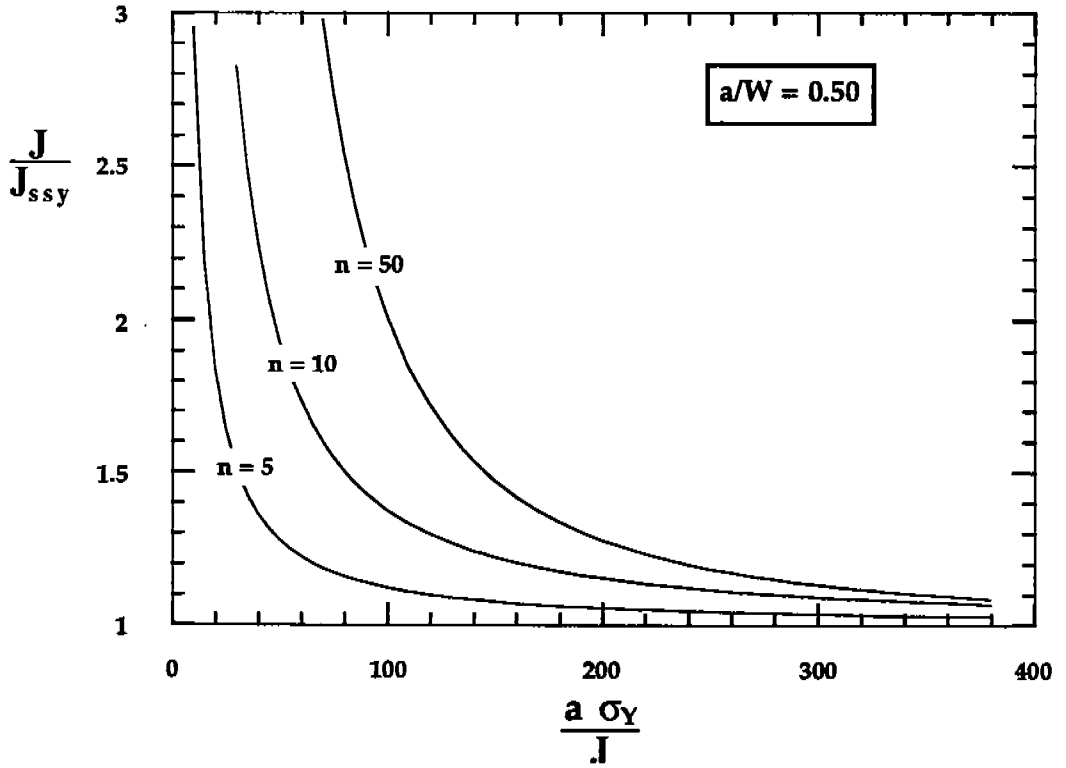

FIGURE 3.16 J/J_{ssy} as a function of strain hardening, J and flow stress.

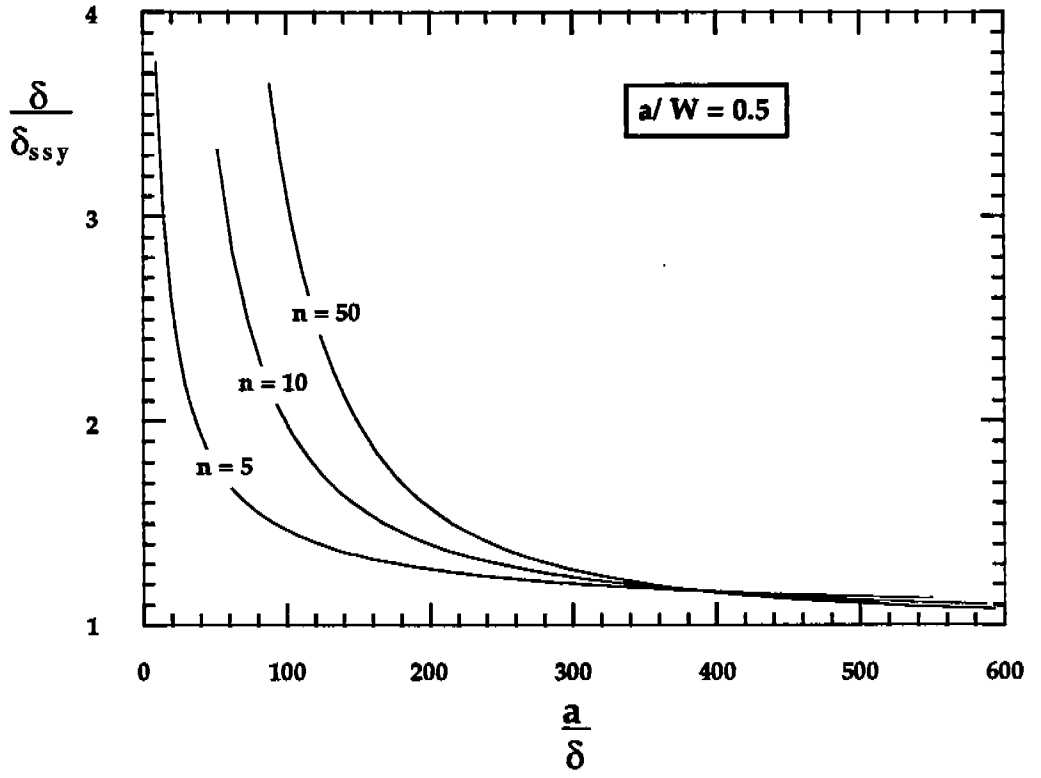

FIGURE 3.17 Effect of specimen size on critical CTOD values for a/W = 0.5

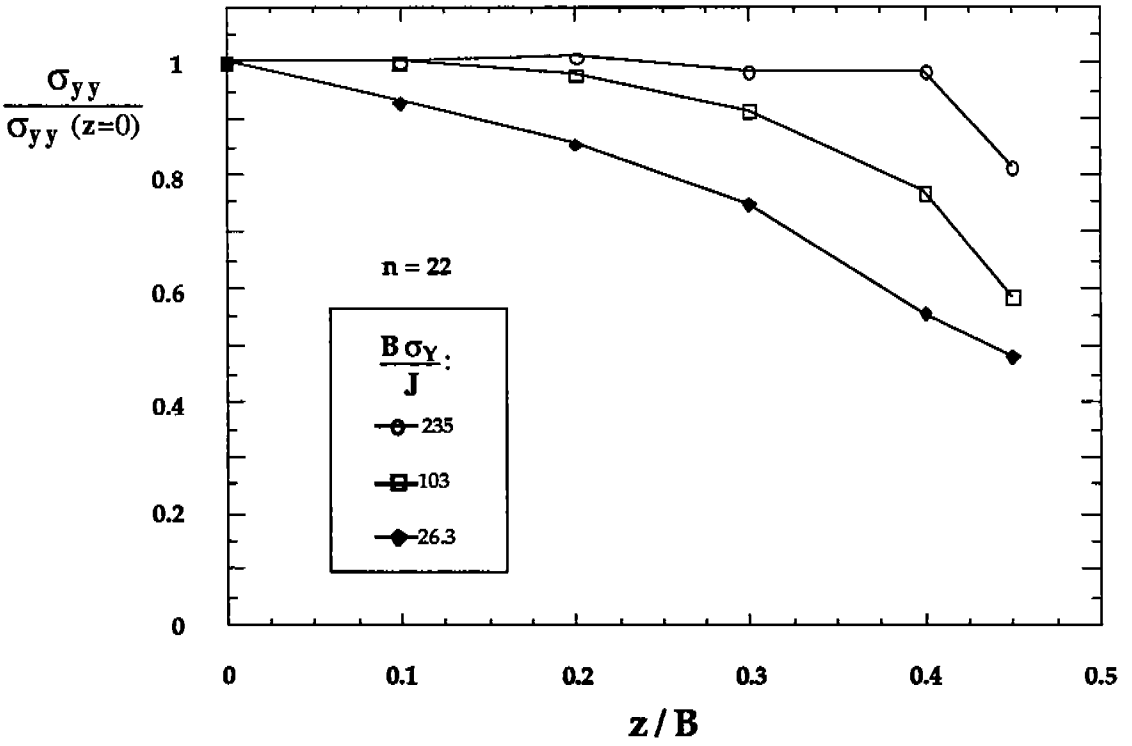

FIGURE 3.18 Variation of normal stress through the thickness of an SENB specimen [25].

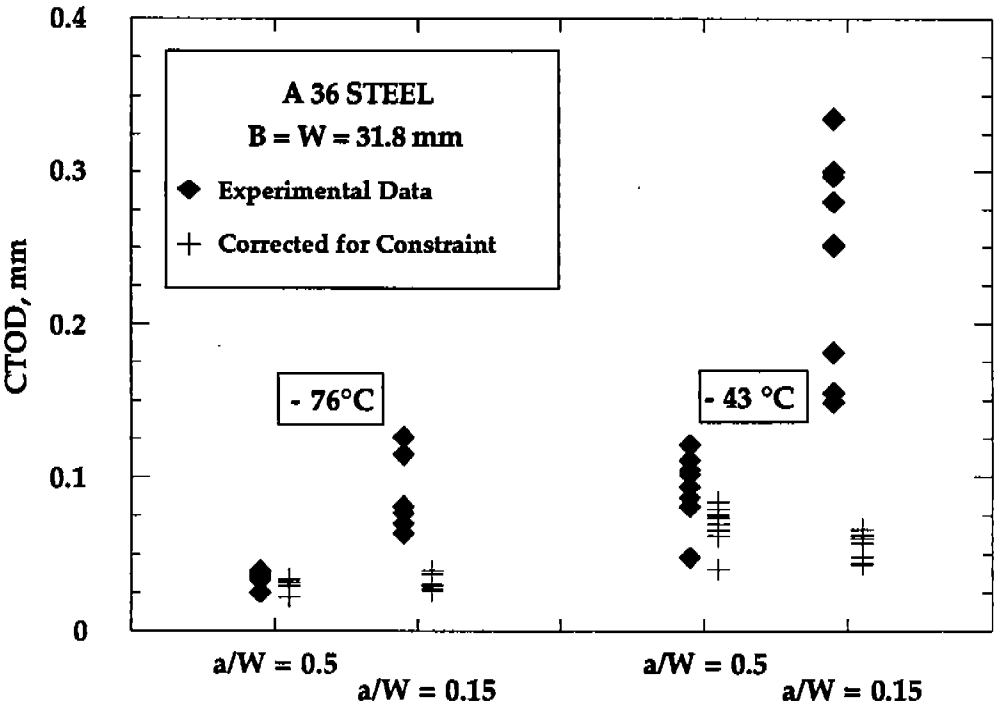

FIGURE 3.19 Comparison of experimental CTOD values for A 36 steel with CTOD corrected for constraint loss. Data were obtained from Sorem [27].

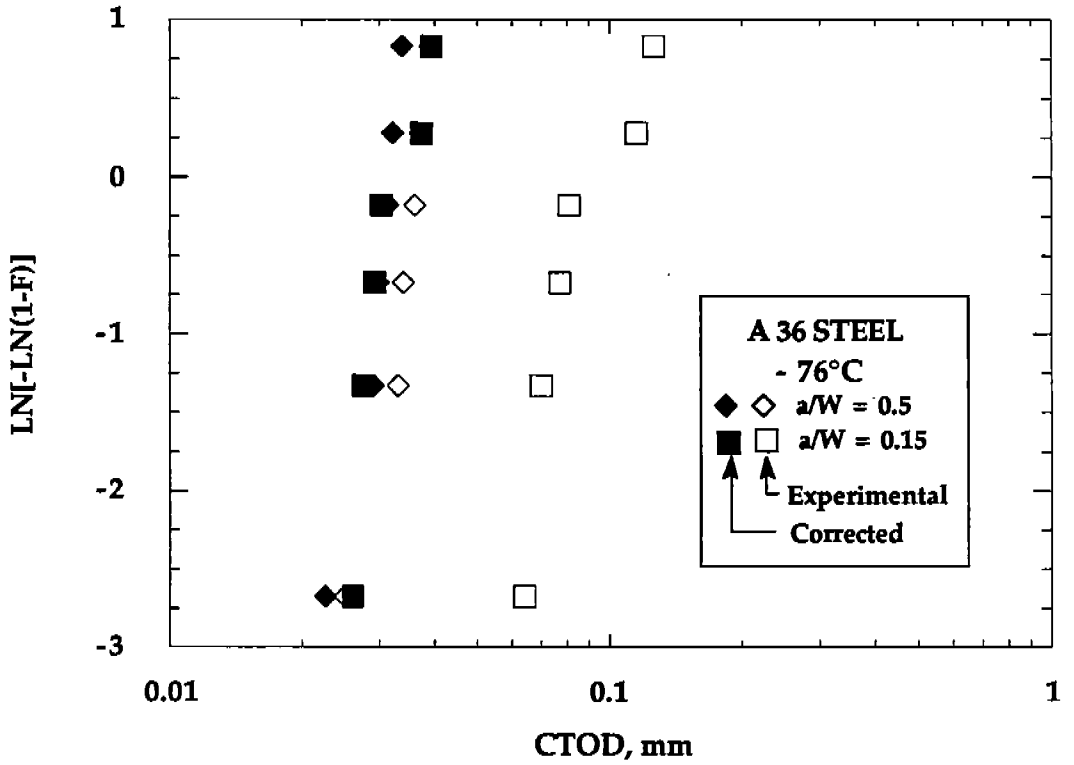

FIGURE 3.20. Weibull plot of A 36 steel CTOD data at - 76°C.

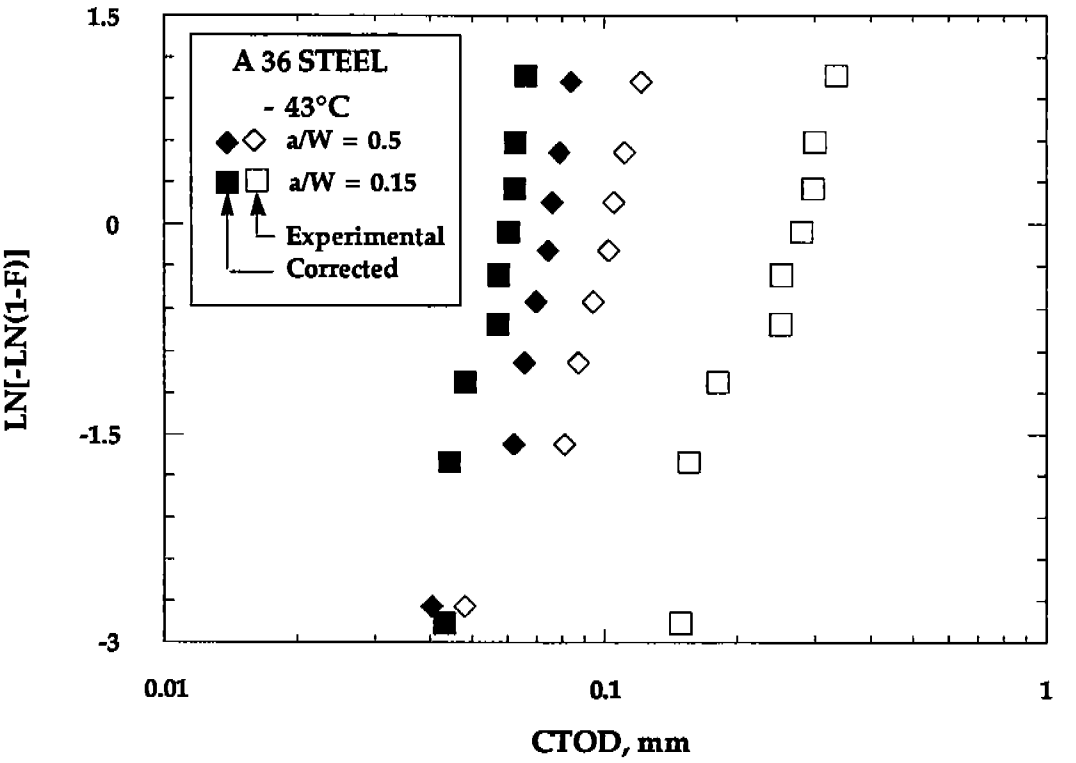

FIGURE 3.21. Weibull plot of A 36 steel CTOD data at - 43°C.

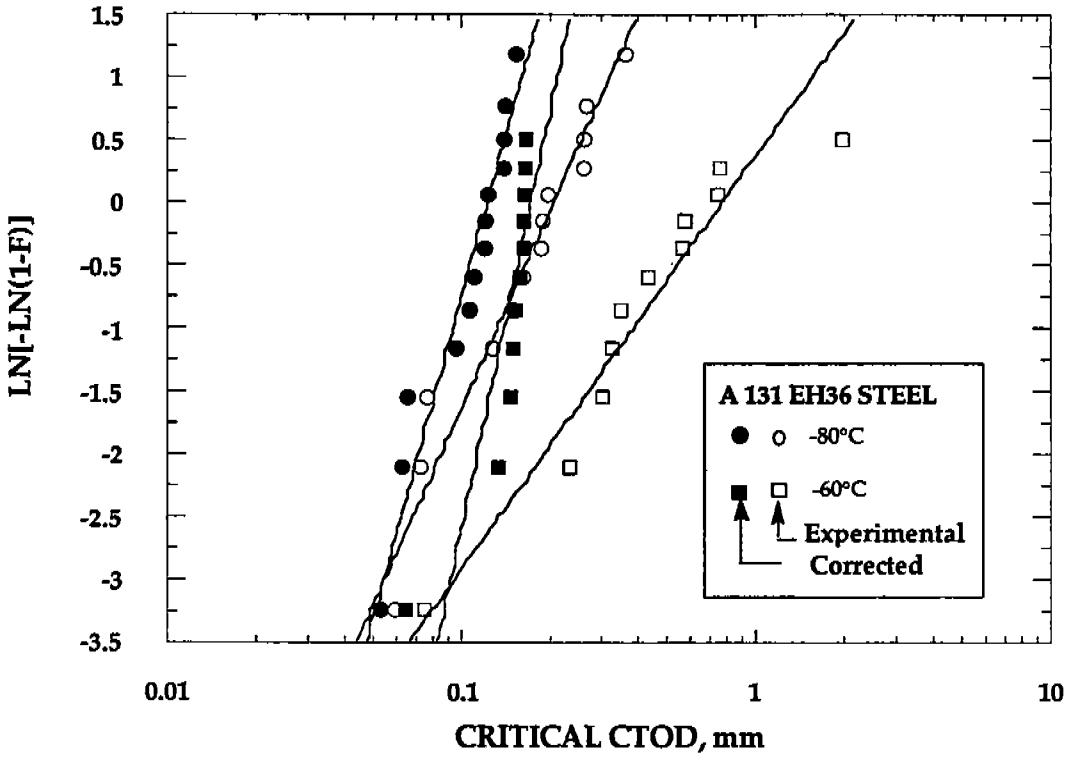

FIGURE 3.22 Weibull plot for A131 EH36 steel CTOD data corrected for constraint.

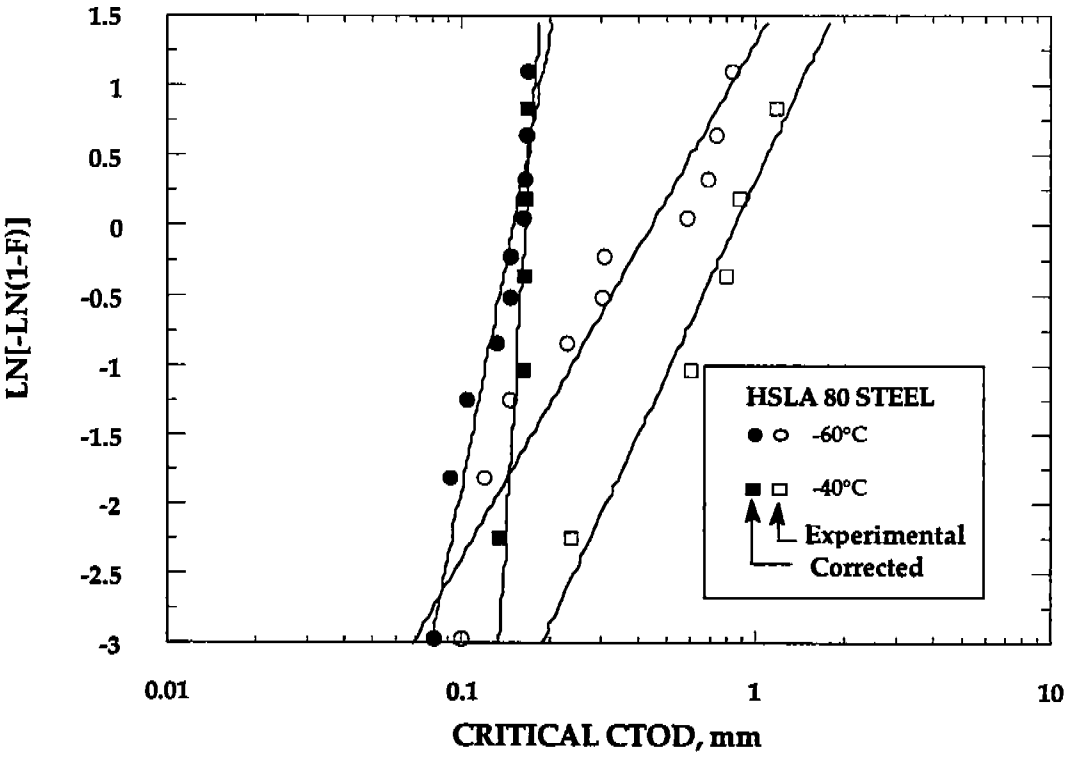

FIGURE 3.23 Weibull plot for HSLA 80 steel CTOD data corrected for constraint.

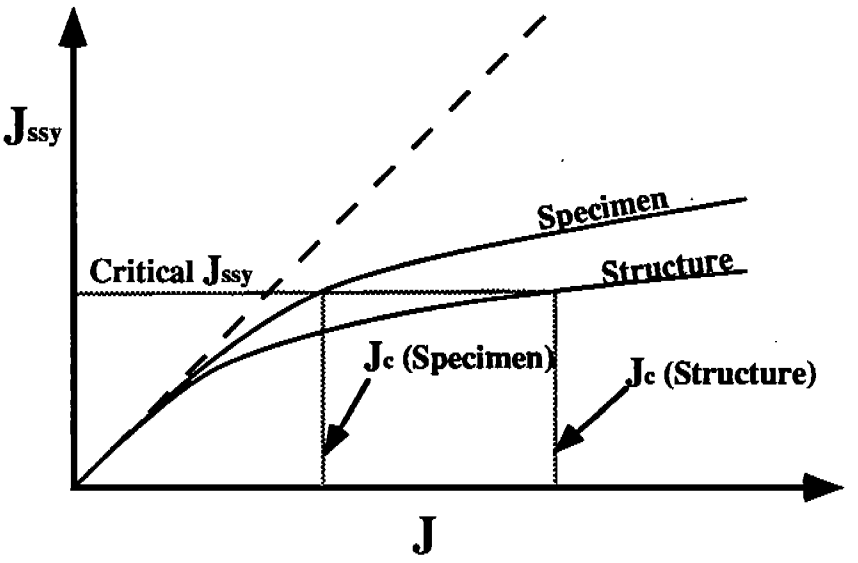

FIGURE 3.24 Correlation of J_c values for a structure and a test specimen.

4. COMPARISON BETWEEN FRACTURE TESTS

4.1 J-CTOD RELATIONSHIPS

The J integral and the crack tip opening displacement (CTOD) are both measures of elastic-plastic fracture toughness. Existing J integral approaches are concerned with ductile fracture, while CTOD-based approaches are usually applied to the ductile-brittle transition region. The difference in application of the two parameters is due to tradition rather than any sound technical reason. J integral methodology was developed by the nuclear power industry, where service temperatures are on the upper shelf, while CTOD approaches were developed for welded structures at lower temperatures (eg. North Sea platforms). In principle, both parameters are equally valid for all fracture mechanisms.

If a relationship between J and CTOD can be established, it should be possible to convert a fracture toughness data set quantified in terms of one parameter to the other parameter. This would allow one to use J and CTOD data interchangeably in fracture analyses.

Shih [28] derived a relationship between J and CTOD for cases where the crack tip conditions are characterized by the HRR singularity:

$$J = \frac{\sigma_0 \delta}{d_n} \tag{4.1}$$

where d_n is a dimensionless parameter which depends on material flow properties. Equation (4.1) implies that there is a unique relationship between J and CTOD for a given material when J controlled conditions exist at the crack tip. When J no longer characterizes crack tip conditions, the J-CTOD relationship becomes geometry dependent [12,28]. The effect of specimen geometry and strain hardening on the relationship between J and CTOD is explored below.

4.1.1 Analytical Comparisons

The finite element results that were introduced in Chapter 3 are well suited to an analytical comparison of J and CTOD. For each configuration, hardening exponent,

and load step, the J integral was determined by the energy domain integral approach, while CTOD was determined from the blunted mesh by the 90° intercept method.

Figures 4.1 to 4.3 illustrate the effect of a/W on the J-CTOD relationship in SENB specimens. Note that the ratio $J/(\sigma_0\,\delta)$ depends on a/W at large J values but converges to a single, geometry-independent value as J approaches zero; this limiting value of $J/(\sigma_0\,\delta) = 1/d_n$. In general, the ratio $J/(\sigma_0\,\delta)$ decreases with constraint loss; this parameter is often referred to as the constraint factor.

Figure 4.4 illustrates the effect of hardening exponent on the J-CTOD relationship. The ordinate was normalized by the flow stress, σ_Y, rather than the yield strength, in order to reduce the effects of strain hardening. The ratio $J/(\sigma_Y\,\delta)$ decreases with decreasing strain hardening, but is much less sensitive to n than the ratio $J/(\sigma_0\,\delta)$.

4.1.2 Experimental Comparisons

Critical J and CTOD values were both determined from each fracture toughness test on the two ship steels. Figures 4.5 and 4.6 are plots of J/σ_Y versus CTOD for the A 131 EH36 and HSLA 80 steels, respectively. Although there is some scatter, the data follow a linear trend with a slope of 1.68 for the EH36 steel and 1.85 for the HSLA 80 material.

The A 131 EH36 and HSLA 80 steels have approximate strain hardening exponents of 9 and 17, respectively (if the upper yield point is ignored). The slopes in Figs. 4.5 and 4.6 are slightly higher than predicted from finite element analysis (Fig. 4.4). This discrepancy may be caused by a number of factors. The scatter at high CTOD values implies some uncertainty in the computed slopes. In addition, the experimental estimates of J and CTOD do not necessarily correspond to the "true" values of these parameters; equations for J and CTOD in ASTM standards contain simplifying assumptions, such as the plastic hinge model.

The scatter in Figs. 4.5 and 4.6 is highest for the upper shelf (J_m and δ_m) toughness values. The J and CTOD at maximum load were computed independently in each case

The precise location of the maximum load plateau is subject to interpretation. When two independent measurements of maximum load toughness are made from a given load-displacement record, the two measurements will probably not yield the same point on the curve, even if the same individual makes both mea-

surements. Thus the scatter in Figs. 4.5 and 4.6 may be due to lack of precision in measurement rather than variability in the J-CTOD relationship.

The ratio $J/(\sigma_Y \delta)$ for the two steels is plotted against CTOD in Figs. 4.7 and 4.8. These plots reveal deviations from a constant J-CTOD ratio that were not evident in Figs. 4.5 and 4.6. In the case of the EH36 steel (Fig. 4.5), the computed $J/(\sigma_Y \delta)$ ratio exceeds 2.0 at low CTOD values. This behavior is probably associated with the separation of energy and displacement into elastic and plastic components. The ASTM relationships for J and CTOD assume that elastic and plastic behavior can be separated, but this assumption may result in errors when elastic and plastic displacements are of similar magnitude.

4.2 CVN-FRACTURE TOUGHNESS RELATIONSHIPS

Charpy impact testing is much more established in the welding fabrication industry than fracture mechanics tests such as J and CTOD. Although Charpy data provide a qualitative estimate of the toughness of a material, absorbed energy values do not give quantitative predictions of structural performance. Consequently, many investigators have attempted to correlate Charpy data with fracture toughness measurements. There are a number of published empirical correlations between Charpy energy and K_{IC}. Unfortunately, most of these correlations are unreliable, and none are universally applicable.

A theoretical CVN-fracture toughness relationship for the ductile-brittle transition region has recently been developed. A preliminary experimental validation of this model has given encouraging results [29]. In the present study, dynamic and quasistatic tensile data are used in conjunction with Charpy data and the theoretical model to predict CTOD transition curves. The background of the theoretical model is outlined briefly below.

4.2.1 Theoretical Model

The theoretical Charpy-fracture toughness relationship is based on a weakest link statistical model for cleavage fracture [24]. Failure is assumed to occur when at least one critical microstructural feature is sampled along the crack front. The failure probability is given by

$$F = 1 - \exp\left(- \int_0^V \frac{(\sigma_1 - \sigma_u)^m}{\psi} dV \right) \tag{4.2}$$

where V is volume, σ_1 is principal stress, σ_u is a threshold fracture stress, and m and ψ are constants. The principal stress distribution is governed by geometry, while σ_u, m and ψ are assumed to be material constants that completely define the inherent fracture properties of the microstructure.

When CVN toughness is related to fracture toughness from a specimen with a sharp crack, σ_u, m and ψ are assumed to be geometry independent; the geometry dependence is taken into account through the σ_1 distributions for the two configurations. The finite element results of Shih and German [14] are used to define the stress distribution ahead of a sharp crack, while the stress distribution in a dynamically loaded CVN specimen is obtained from a solution published by Norris [30].

Figures 4.9 and 4.10 schematically illustrate how fracture toughness is predicted from CVN data. The material fracture constants (σ_u, m and ψ) are inferred from the Charpy transition curve, the Norris finite element solution [30] and dynamic flow properties (Fig. 4.9). These parameters are then used in conjunction with the Shih and German crack tip stress analysis [14] and the quasistatic flow properties to compute the fracture toughness transition curve (Fig. 4.10). Additional details are given below.

Norris [30] plotted principal stress contours for a dynamically loaded CVN specimens at times (after impact) of 230 and 330 μs, which correspond to 14 and 23 J of absorbed energy, respectively. Figure 4.11 is a plot of cumulative volume versus principal stress, normalized by the dynamic yield strength. The two curves can be collapsed onto a single curve by dividing the volume by (CVN energy)$^{0.743}$, as illustrated in Fig. 4.12. At a fixed temperature, the ordinate in Fig. 4.12 depends only on σ_1; that is,

$$\frac{V}{CVN^{0.743}} = h(\sigma_1) \tag{4.3}$$

Solving for dV gives:

$$dV = CVN^{0.743} \frac{\partial h}{\partial \sigma_1} d\sigma_1 \tag{4.4}$$

Thus the failure probability in a Charpy specimen at a given energy value is given by

$$F = 1 - e^{-\lambda} \tag{4.5}$$

where

$$\lambda = CVN^{0.743} \int_{\sigma_{max}}^{\sigma_u} \frac{(\sigma_1 - \sigma_u)^m}{\psi} \frac{\partial h}{\partial \sigma_1} d\sigma_1 \tag{4.6}$$

Note that the integrand is independent of Charpy energy. Consider the temperature, T*, at which the median (F = 0.5) CVN value is 23 J. For F = 0.5, $\lambda = 0.693$; at T*, the λ value that corresponds to 14J is equal to 0.479. Thus the failure probability at 14 J and T* = 0.381.

There are three unknowns in Eq. (4.6): σ_u, m and ψ. One unknown can be eliminated by setting $\sigma_u = 2\,\sigma_o$, where σ_o is the dynamic yield strength at T*. The other two unknowns can be inferred by solving simultaneous integral equations for $\lambda = 0.693$ and $\lambda = 0.479$.

Once the three material fracture constants have been computed, they are used in conjunction with the quasistatic flow properties and the Shih and German analysis to determine the fracture toughness transition curve, which can be expressed in terms of J or CTOD. Since the microscopic fracture energy in the Griffith expression is temperature dependent, the ψ value must be adjusted for temperature:

$$\psi(T) = \psi(T^*) \left(\frac{\gamma_p(T^*)}{\gamma_p(T)} \right)^{m/2} \tag{4.7}$$

where γ_p is the Griffith fracture energy. Wallin, et al. [22] have estimated the temperature dependence of γ_p for ferrite-pearlite microstructures:

$$\gamma_p = 9.17 + 0.19\, e^{(0.0104T)} \tag{4.8}$$

where γ_p is in J/m^2 and T is in degrees Kelvin.

4.2.2 Comparison With Experiment

The dynamic and static tensile data for the A 131 EH36 and HSLA 80 steel, as well as the CVN transition curves were used to predict CTOD transition curves. Since it was not possible to measure yield strength directly in the high rate tensile tests ($\dot{\varepsilon}$ = 280 s^{-1}), the dynamic yield strength was estimated by

$$\frac{\sigma_{YS}\,(\text{dynamic})}{\sigma_{YS}\,(\text{static})} \cong \frac{\sigma_{TS}\,(\text{dynamic})}{\sigma_{TS}\,(\text{static})} \tag{4.9}$$

According to Norris [30], the average strain rate at the root of a Charpy notch is approximately 3000 s^{-1}, an order of magnitude higher than our dynamic tensile tests. We assumed that the tensile properties at 280 s^{-1} were reasonably representative of the behavior in a CVN specimen. The tensile properties at the intermediate strain rate (5.1 s^{-1}) gave poor predictions of fracture toughness.

Figures 4.13 and 4.14 compare predicted and experimental CTOD values for the two ship steels. In both cases, the predictions are reasonably good, but are slightly nonconservative. Predictions with tensile properties at the intermediate strain rate (which are not shown) were grossly nonconservative.

4.4.2 Parametric Study of Theoretical Model

Although the agreement between theory and experiment is reasonable in Figs. 4.13 and 4.14, a certain amount of subjective judgement was required to assign input values in the model. Thus it is important to assess the sensitivity of the analysis to any assumptions that were made regarding input parameters.

The primary inputs to the theoretical CVN-fracture toughness correlation are the dynamic yield strength at the 23 J transition temperature and the threshold fracture stress, σ_u. The former quantity was obtained from the high rate tensile data, while σ_u was arbitrarily assigned a value of twice the dynamic yield strength (at T_{23J}). In the case of the predictions for the EH 36 plate (Fig. 4.13), the dynamic yield strength was estimated to be 600 MPa, and σ_u was taken as 1200 MPa. The

corresponding values for the HSLA 80 predictions (Fig. 4.14) were 850 and 1700 MPa, respectively.

As stated in the previous section, the high rate tensile data, rather than the intermediate rate data, was used to infer the dynamic yield strength input. This decision was somewhat subjective, in light of the unusual behavior that was observed in the data, where the intermediate strain rate apparently gave higher flow stresses. The highest strain rate is probably more representative of the conditions at the notch root in a CVN specimen, but there is a high degree of uncertainty in the data at this strain rate.

The assigned value of σ_u was arbitrary in each case. The analysis software in its present form is only capable of fitting two of the Weibull parameters; a value must be assumed for the third quantity. Without direct experimental measurements, it is only possible to estimate a range of possible values for σ_u. The threshold fracture stress obviously must be greater than zero. An upper limit can be inferred by considering the crack tip stresses in the temperature range where cleavage is expected; σ_u must be below the maximum stresses in both CVN and fracture toughness specimens. Based on finite element analysis [14,15,30], one can conclude that σ_u must be less than approximately 3 σ_{YS} in the cleavage temperature range.

Because of uncertainties in the input values in the model, a parametric study was performed in order to assess the sensitivity to the predictions on these input parameters. Figures 4.15 and 4.16 show the effect of the assumed threshold stress in the two steels. The assumed σ_u only has a slight effect on the predicted median transition curves, which is fortunate since this value must be assigned arbitrarily in the model. The dynamic yield strength has a much more dramatic effect on the predictions, as illustrated in Figs. 4.17 and 4.18. Even a variation of 50 MPa, or less than 10%, has a significant effect on the computed transition behavior. In the present case, the uncertainty in the dynamic flow properties at the notch of a CVN specimen was considerably more than 50 MPa. Thus, the good agreement between theory and experiment in Figs. 4.13 and 4.14 may be only coincidental.

4.3 STRUCTURAL SIGNIFICANCE OF CVN REQUIREMENTS

Many steel specifications and welding fabrication codes include minimum requirements for CVN toughness. The temperature at which the CVN toughness is required can be above, below, or at the minimum design temperature. The Charpy reference temperature is often based on an empirical correlation between CVN

toughness and K_{IC}. The lack of a consistent definition for a reference temperature indicates that the various CVN-K_{IC} correlations differ from one another considerably.

The Charpy specifications in codes and standards are designed to ensure that the structure operates at or above the transition temperature of the material. In most steels, the onset of the ductile-brittle transition occurs at approximately 20 J (15 ft-lb). The onset of the CTOD transition occurs at around 0.1 mm. At this toughness level, which has been adopted by the offshore industry as a minimum specification for weld heat-affected zones, the material should have reasonable flaw tolerance. The 20 J CVN transition temperature usually does not coincide with the 0.1 mm CTOD transition. The relative position of these transition temperature determines whether a given Charpy requirement is conservative or nonconservative.

Figure 4.19 is a plot of the *difference* between Charpy and CTOD transitions versus yield strength for a variety of steels. When this difference is positive, the CVN transition lies above the fracture toughness transition, and CVN toughness criteria should be conservative as long as the reference temperature is at or below the service temperature. When the difference is negative, CVN requirements may be nonconservative unless the reference temperature is below the service temperature. For the data in Fig. 4.19, two points lie on the conservative side, three points are nonconservative, and the CVN and CTOD transitions coincide in two cases. There seems to be a slight tendency for higher strength materials to have negative CVN-CTOD shift.

There is apparently not a unique relationship between CVN and CTOD transition temperatures. Thus fracture control schemes based on Charpy toughness should be used with extreme caution, if at all.

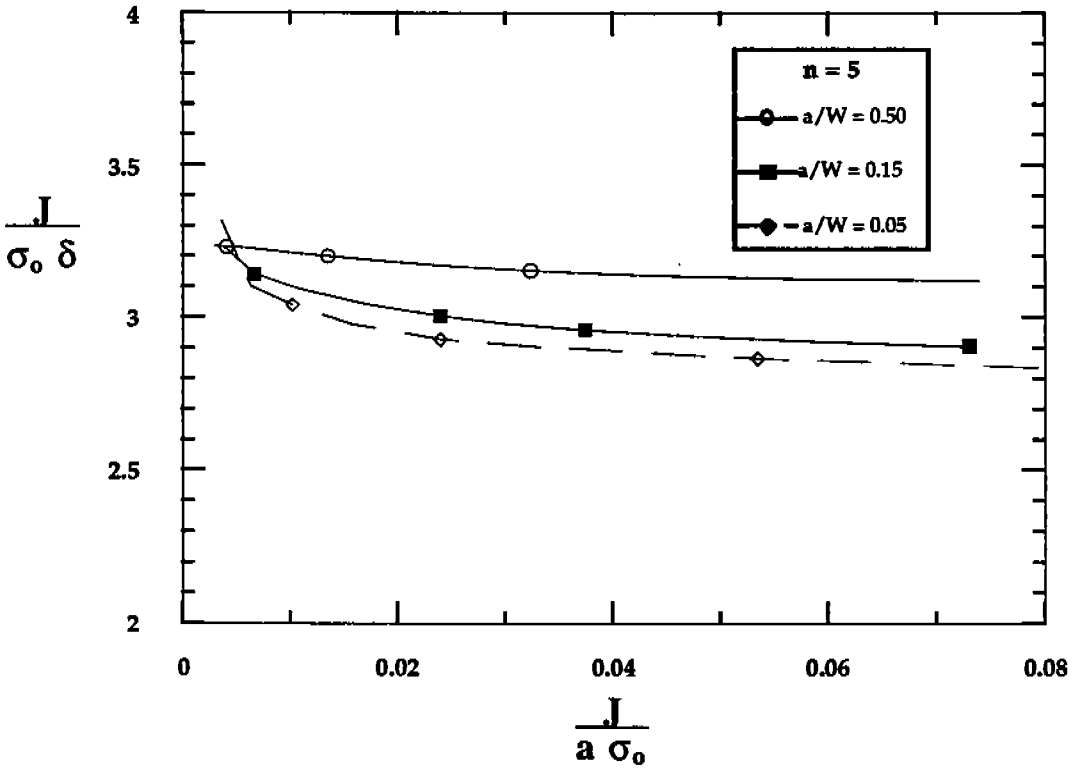

FIGURE 4.1 Analytical J-CTOD relationship as a function of a/W for n = 5.

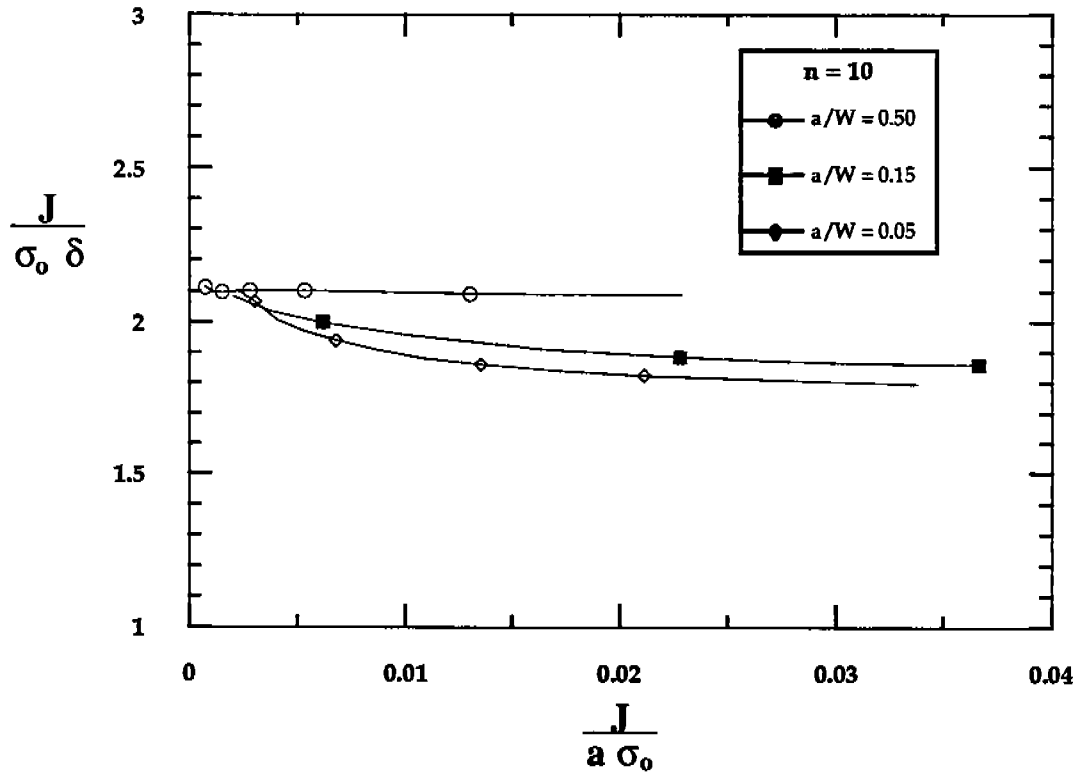

FIGURE 4.2 Analytical J-CTOD relationship as a function of a/W for n = 10.

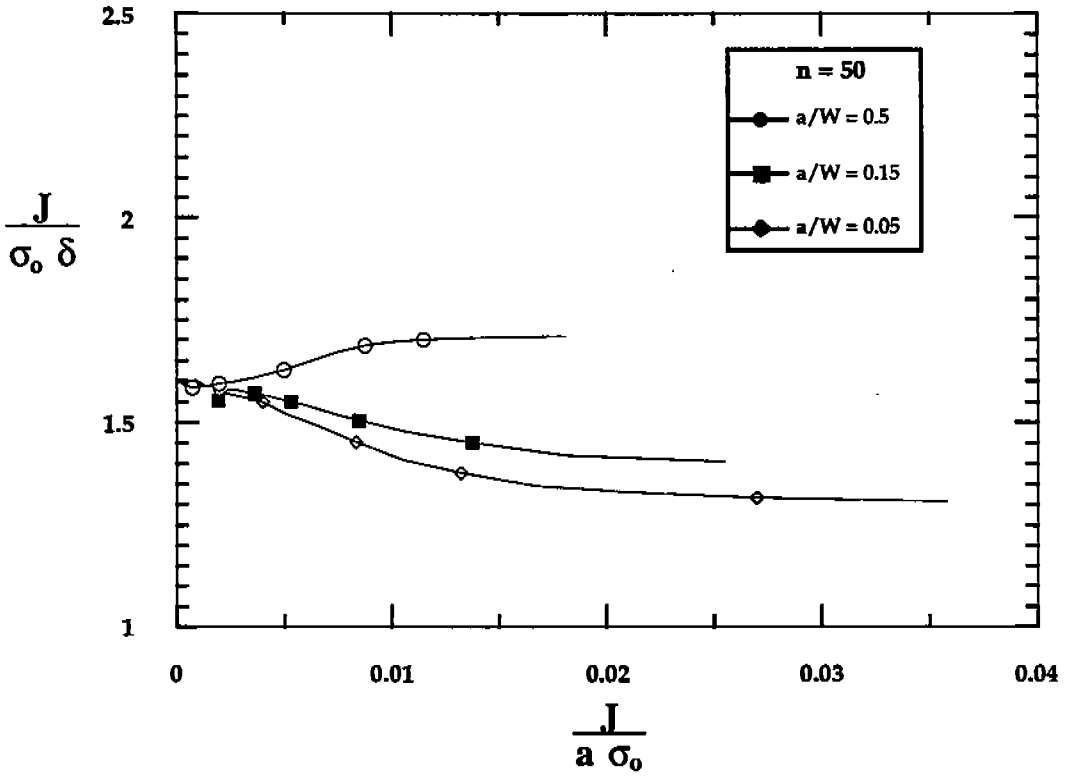

FIGURE 4.3 Analytical J-CTOD relationship as a function of a/W for n = 50.

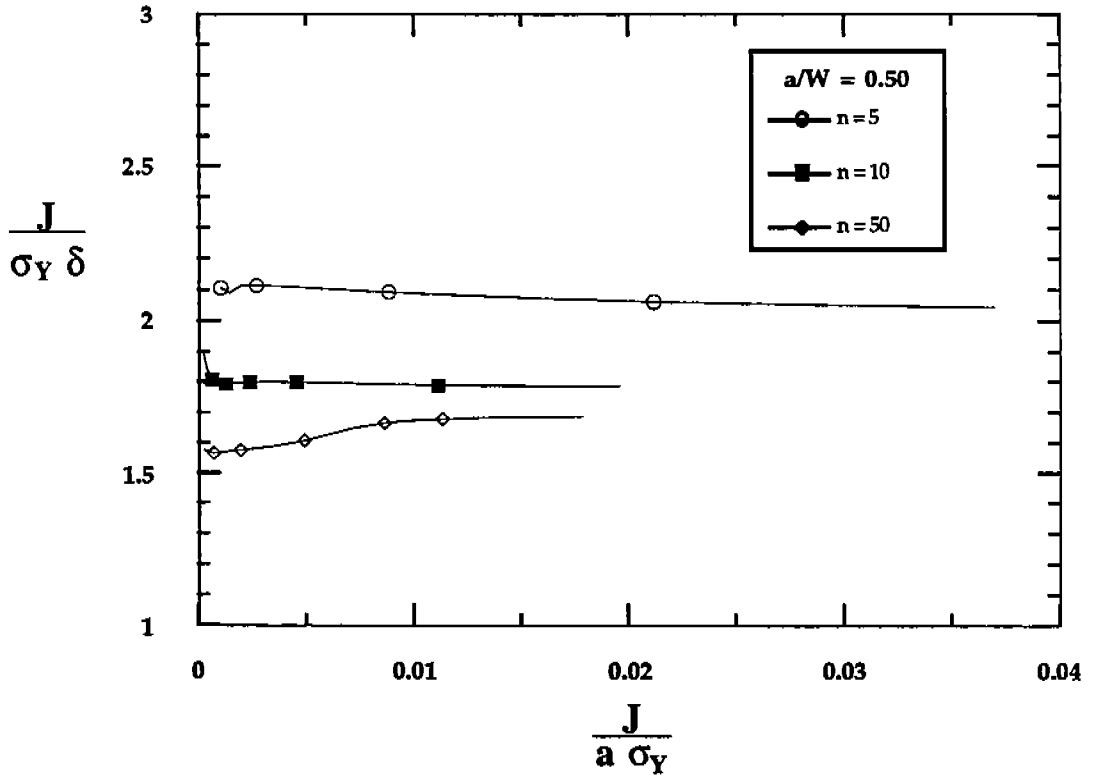

FIGURE 4.4 Effect of strain hardening exponent on the J-CTOD relationship for a/W = 0.5.

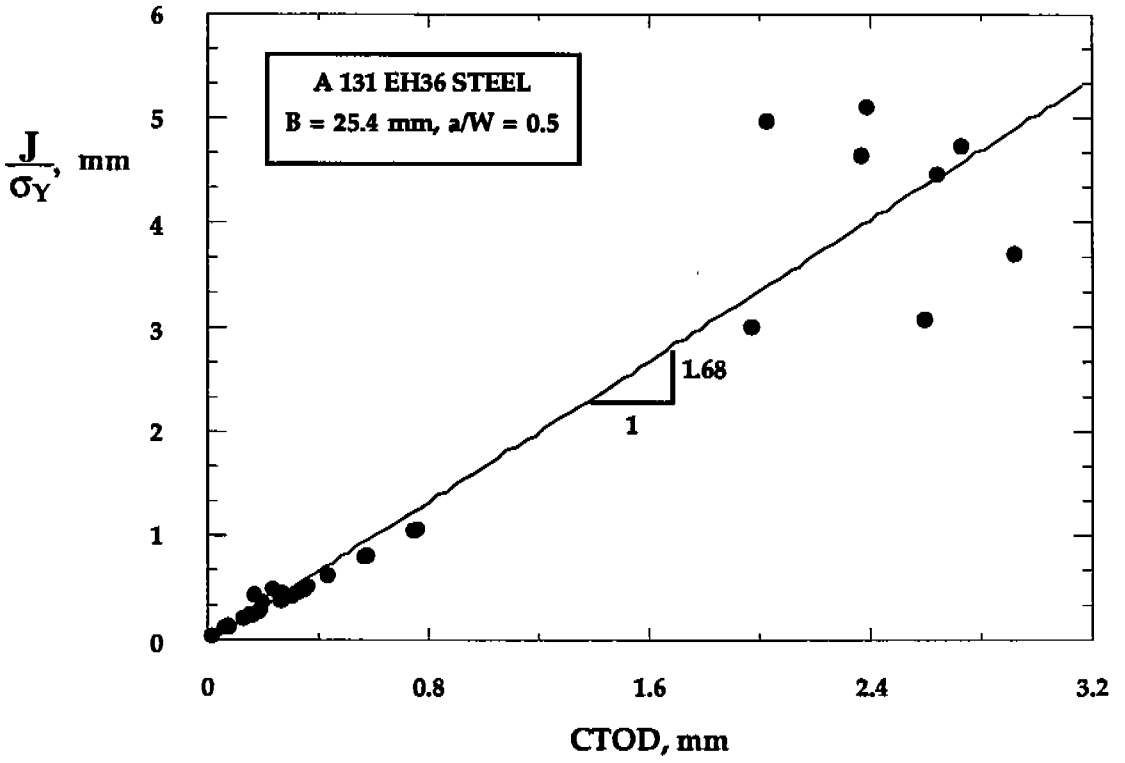

FIGURE 4.5 J versus CTOD for the A 131 EH36 steel plate.

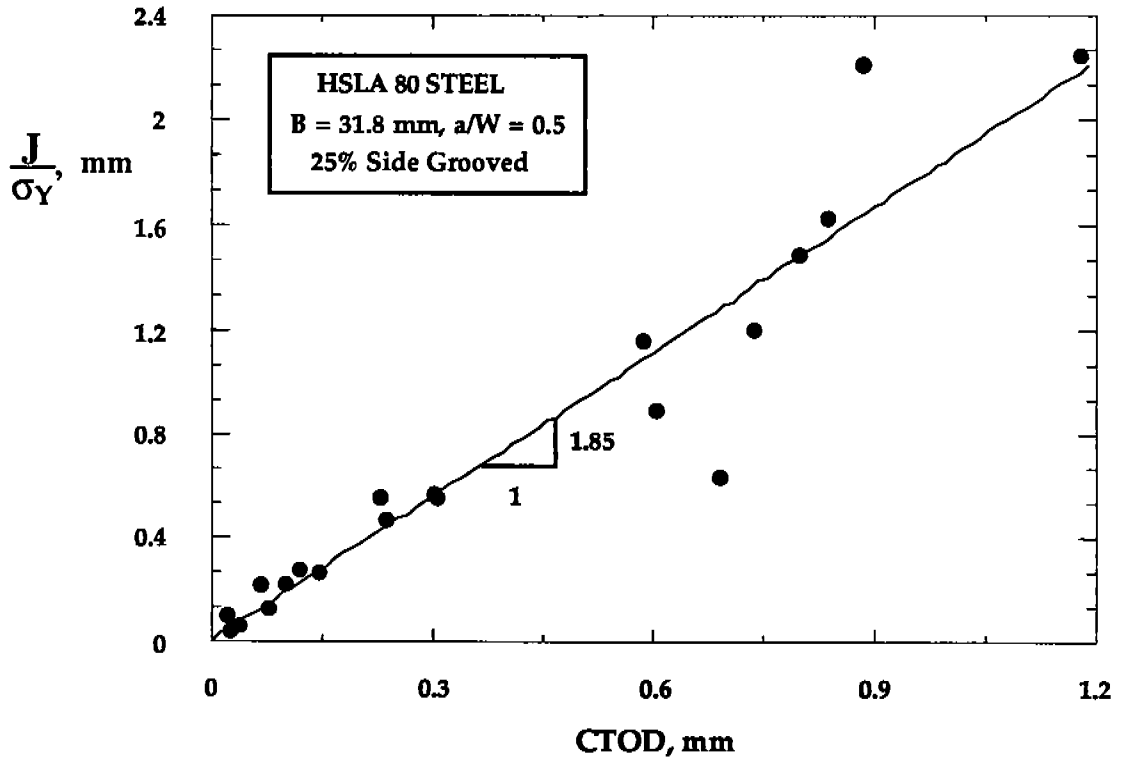

FIGURE 4.6 J versus CTOD for the HSLA 80 steel plate.

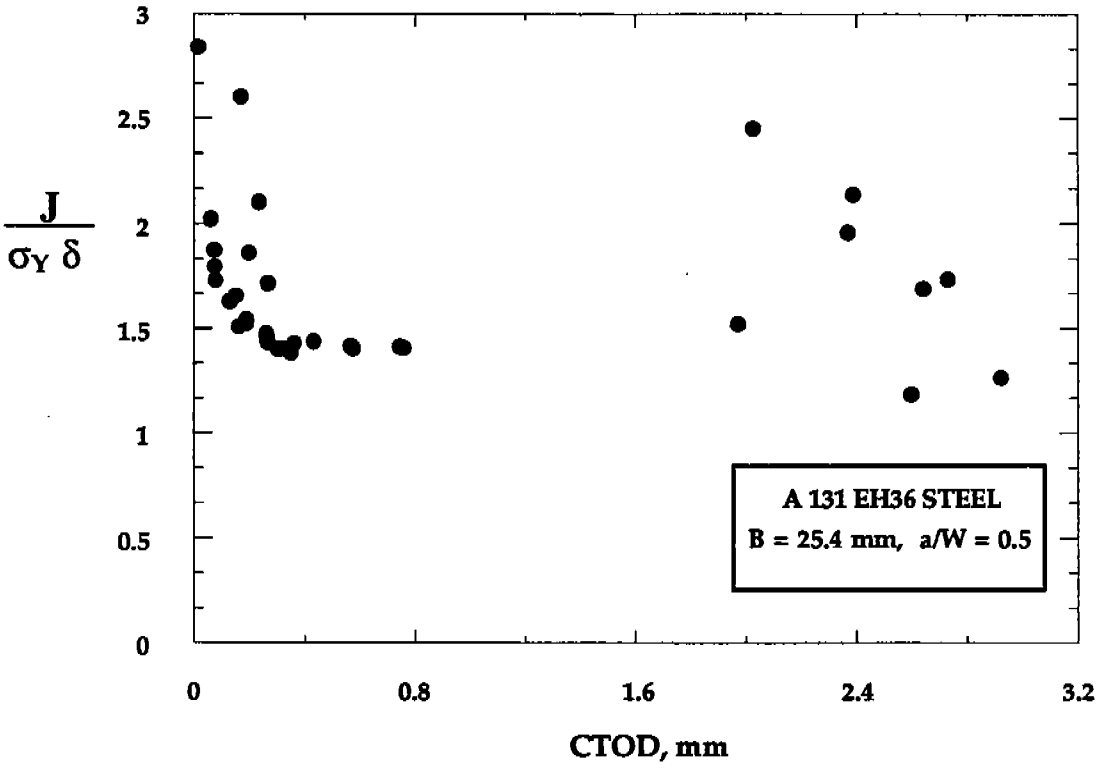

FIGURE 4.7 Experimental J-CTOD ratio for the A 131 EH36 steel.

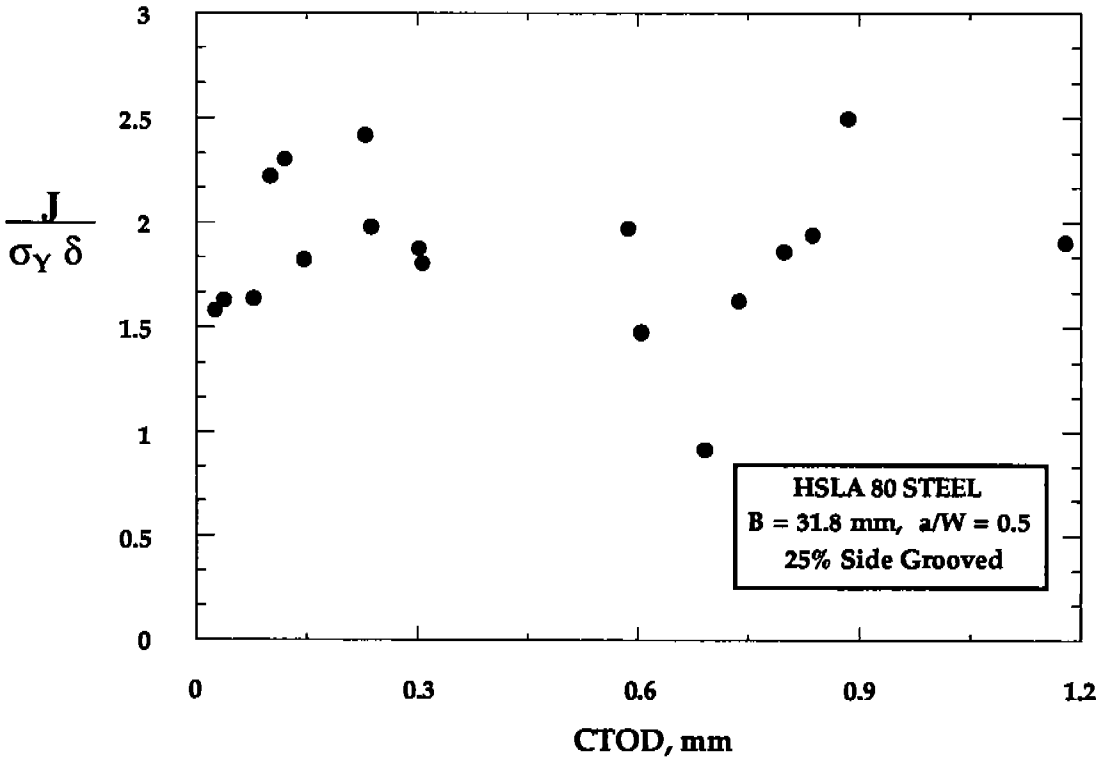

FIGURE 4.8 Experimental J-CTOD ratio for the HSLA 80 steel.

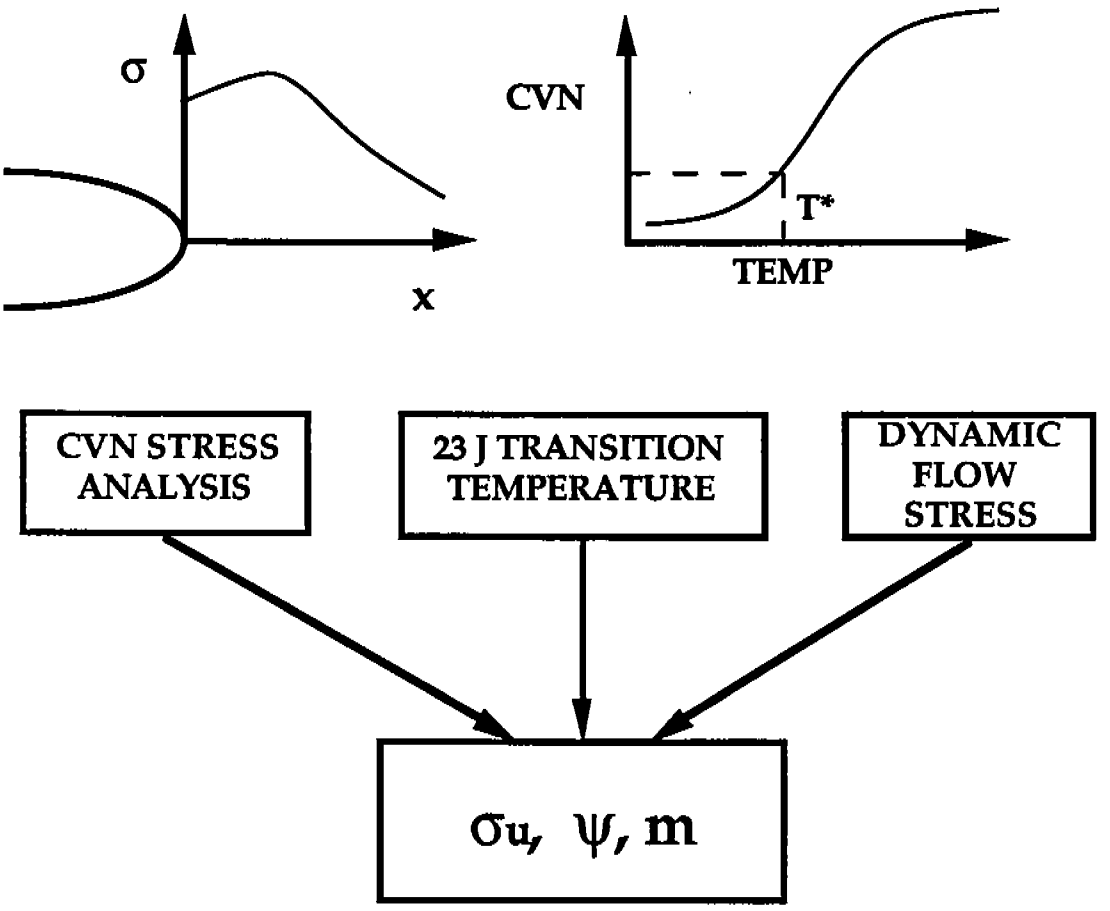

FIGURE 4.9 Schematic representation of the estimation of material fracture constants from CVN data.

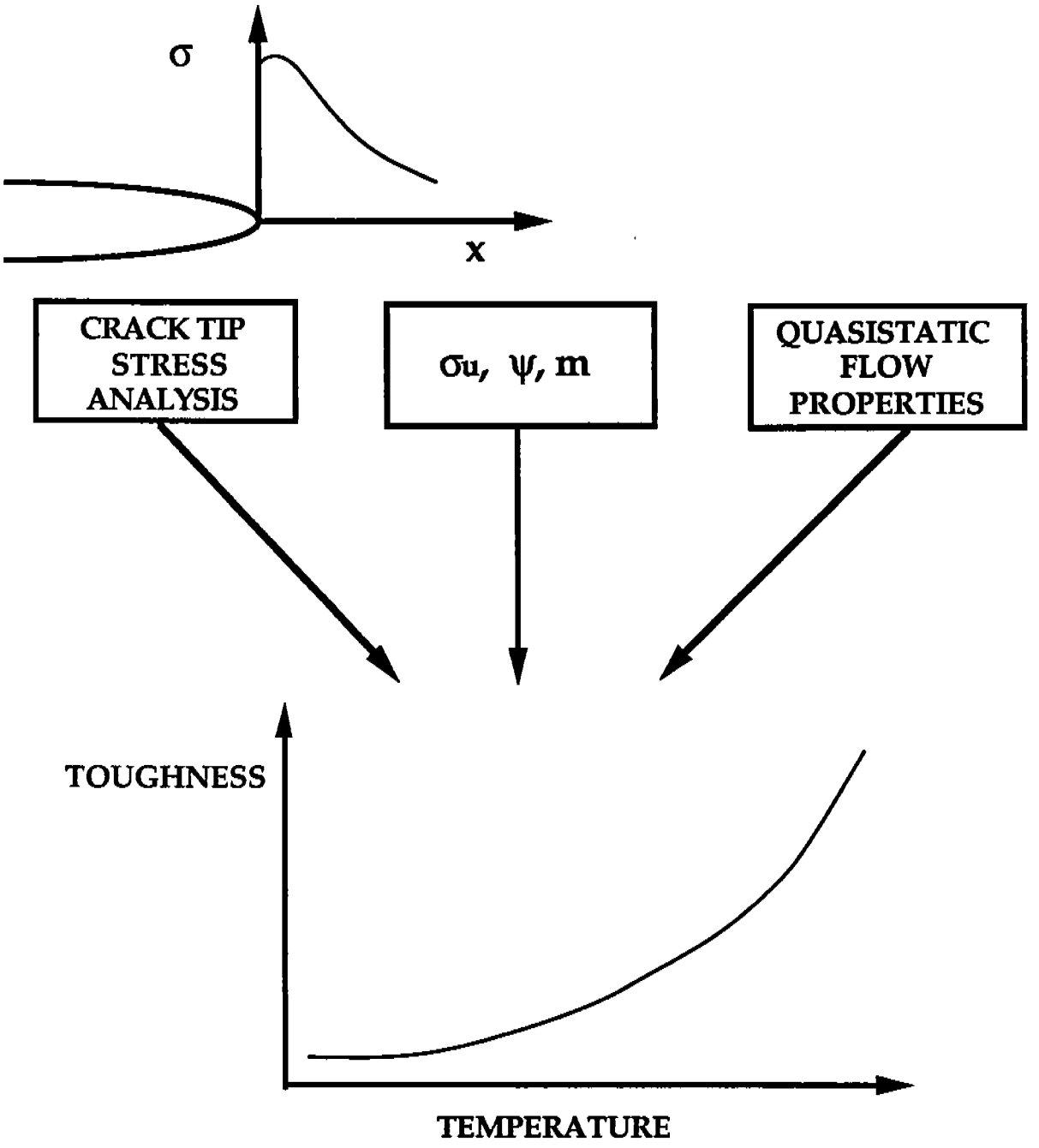

FIGURE 4.10 Schematic of the prediction of fracture toughness from the material fracture constants.

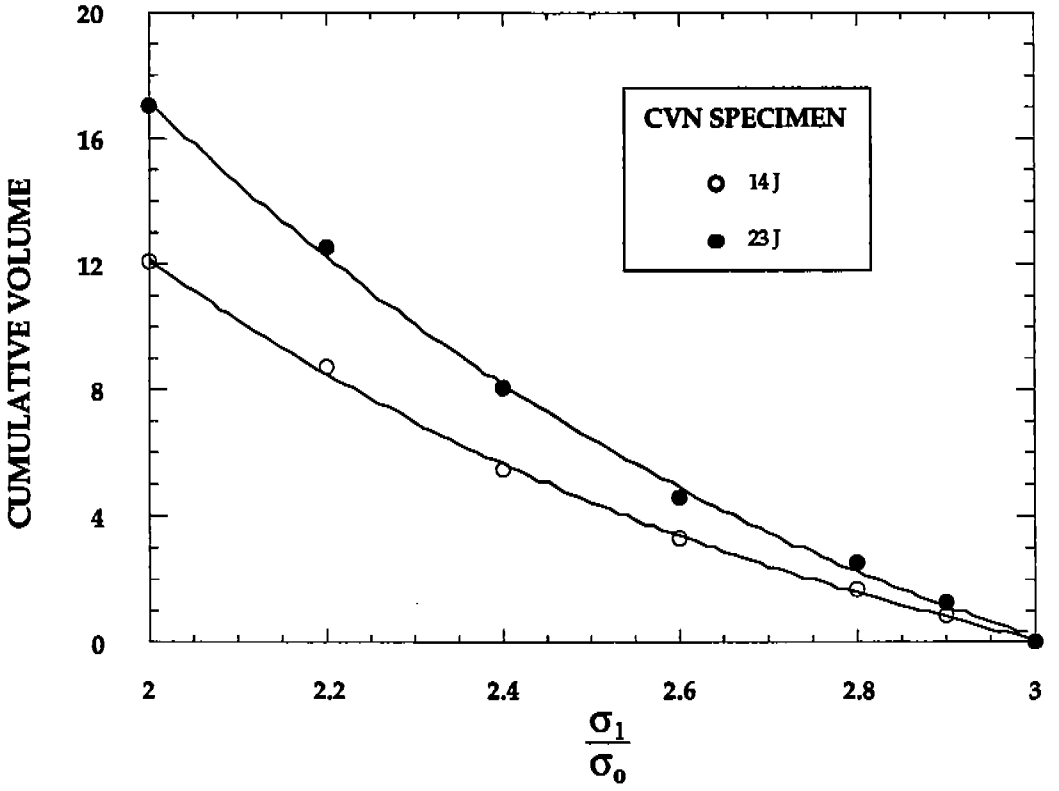

FIGURE 4.11 Cumulative volume sampled ahead of a CVN specimen at two energy levels.

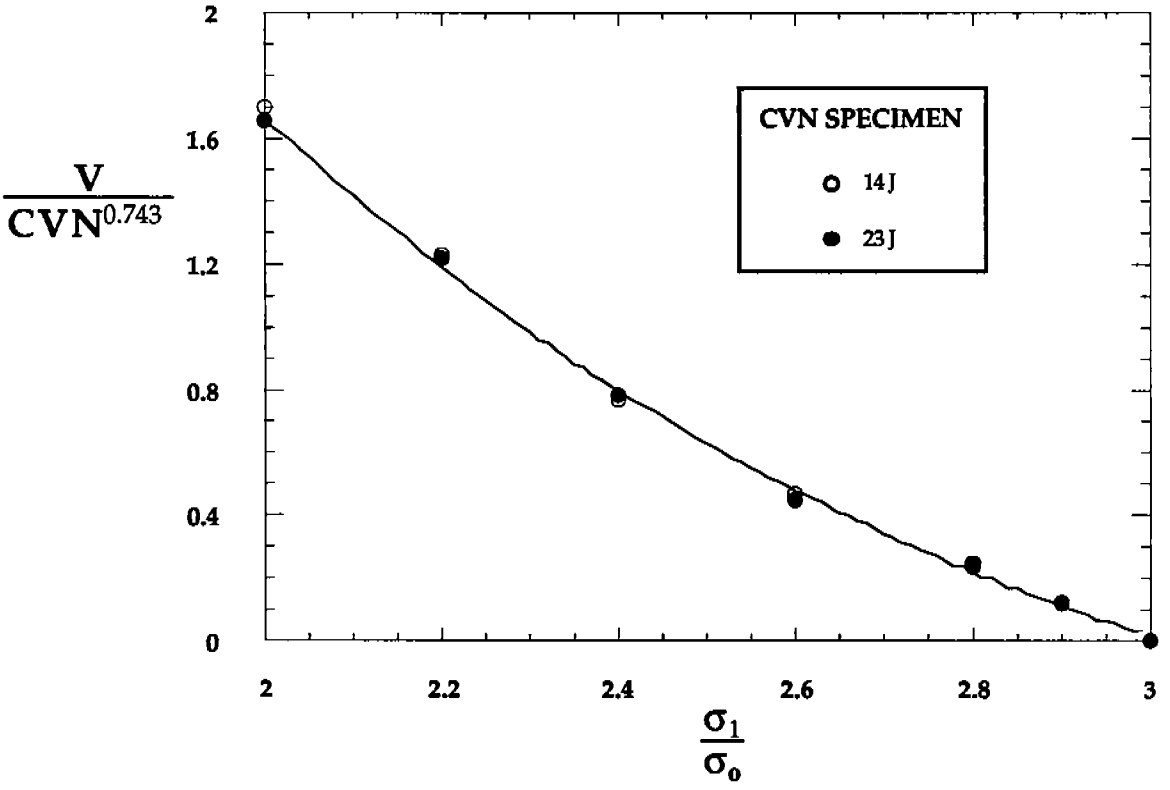

FIGURE 4.12 Cumulative volume ahead of a CVN specimen, normalized by energy.

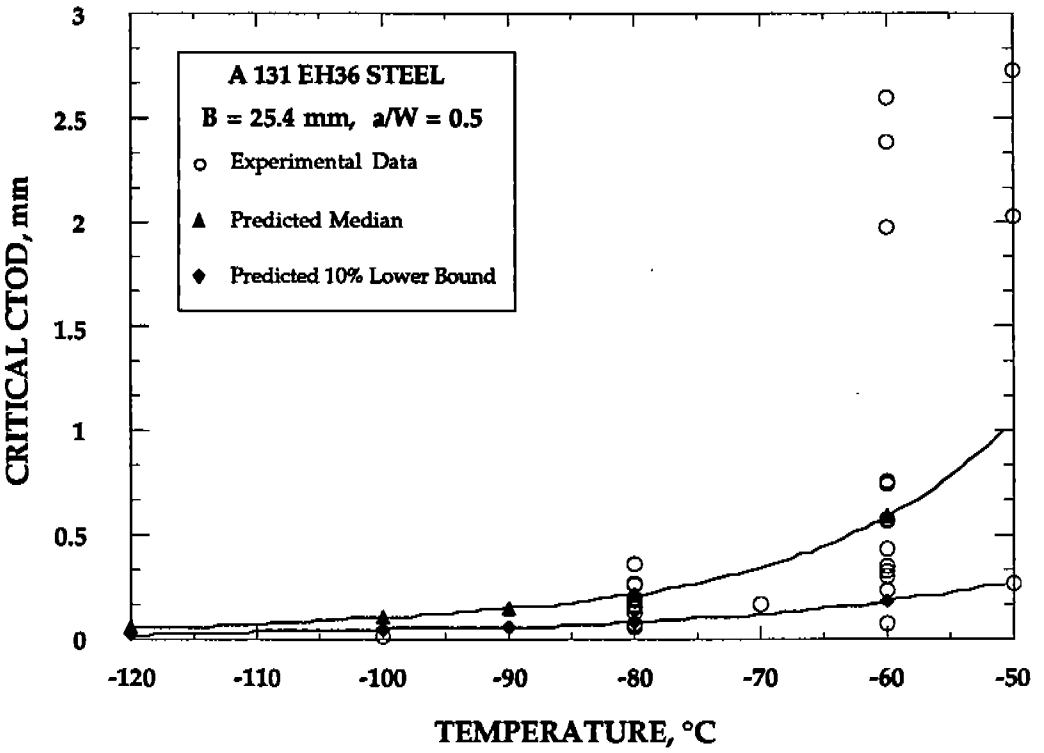

FIGURE 4.13 Predicted and experimental CTOD values for A 131 EH36 steel.

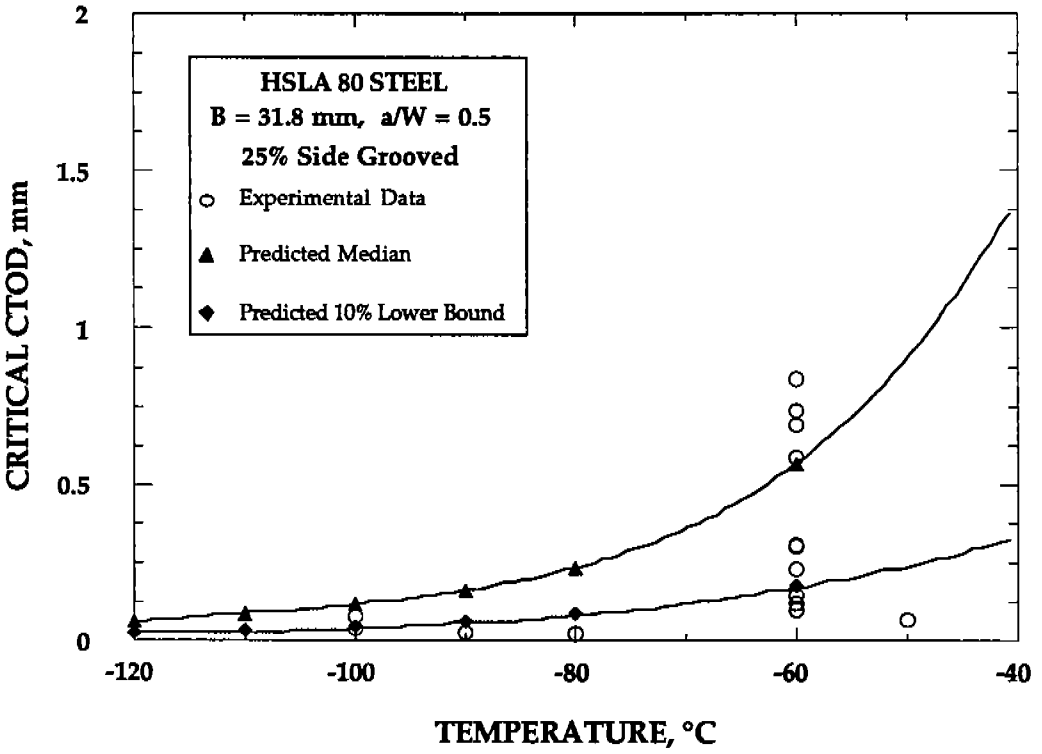

FIGURE 4.14 Predicted and experimental CTOD values for HSLA 80 steel.

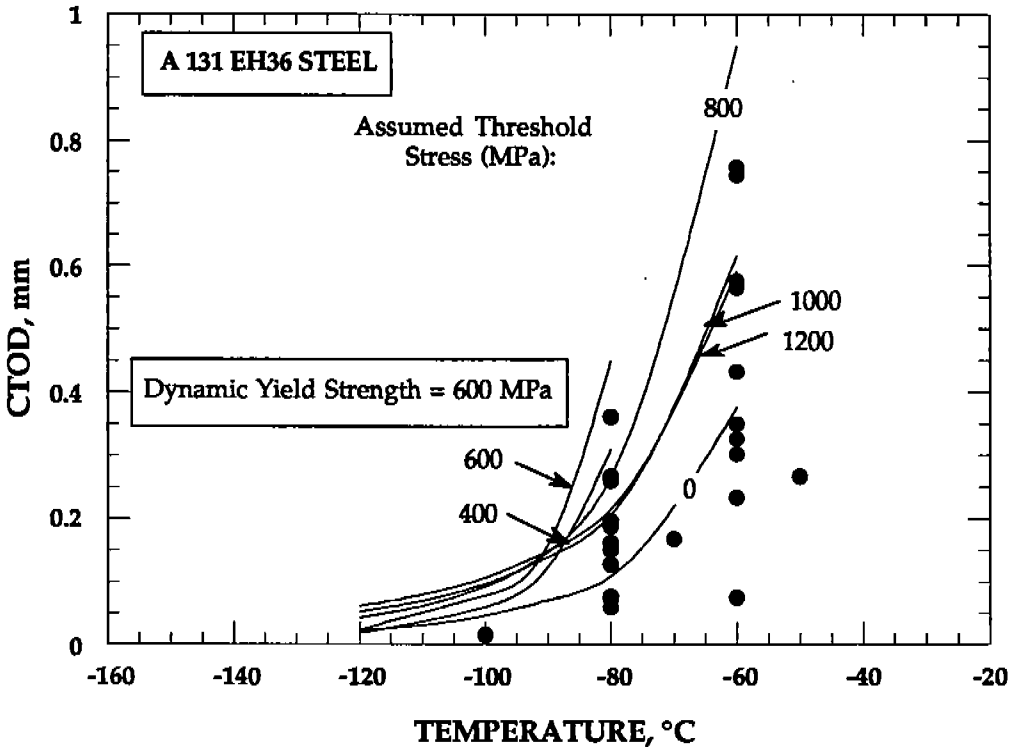

FIGURE 4.15 Effect of the assumed threshold stress on predicted CTOD in the A 131 EH 36 steel.

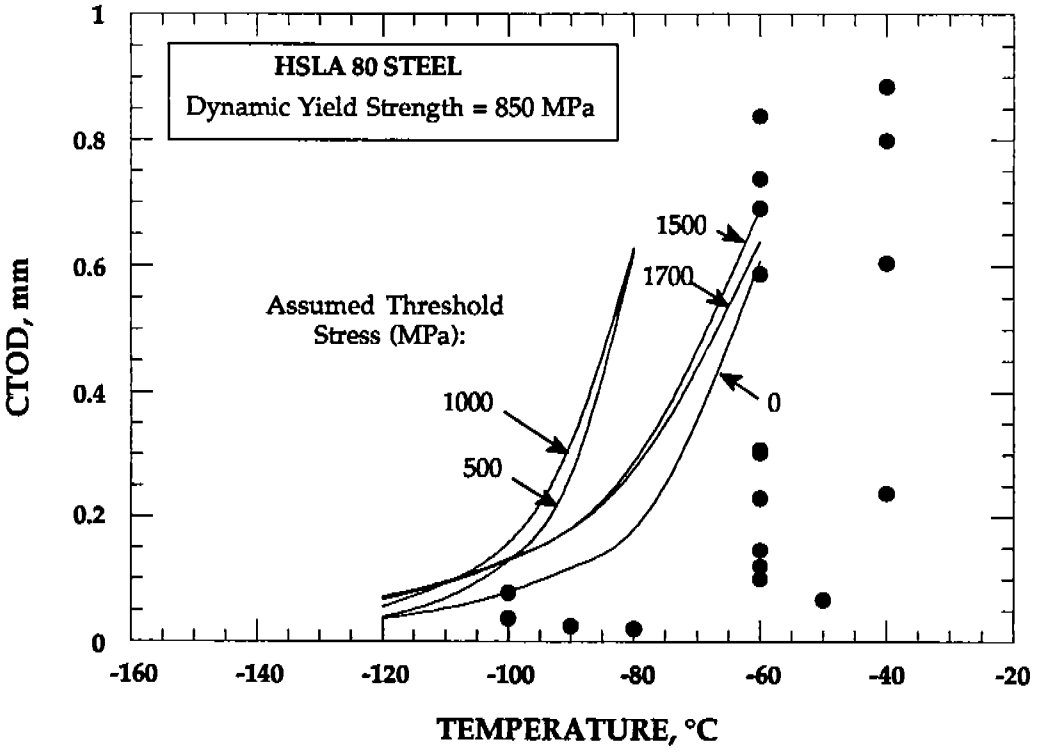

FIGURE 4.16 Effect of the assumed threshold stress on predicted CTOD in the HSLA 80 steel.

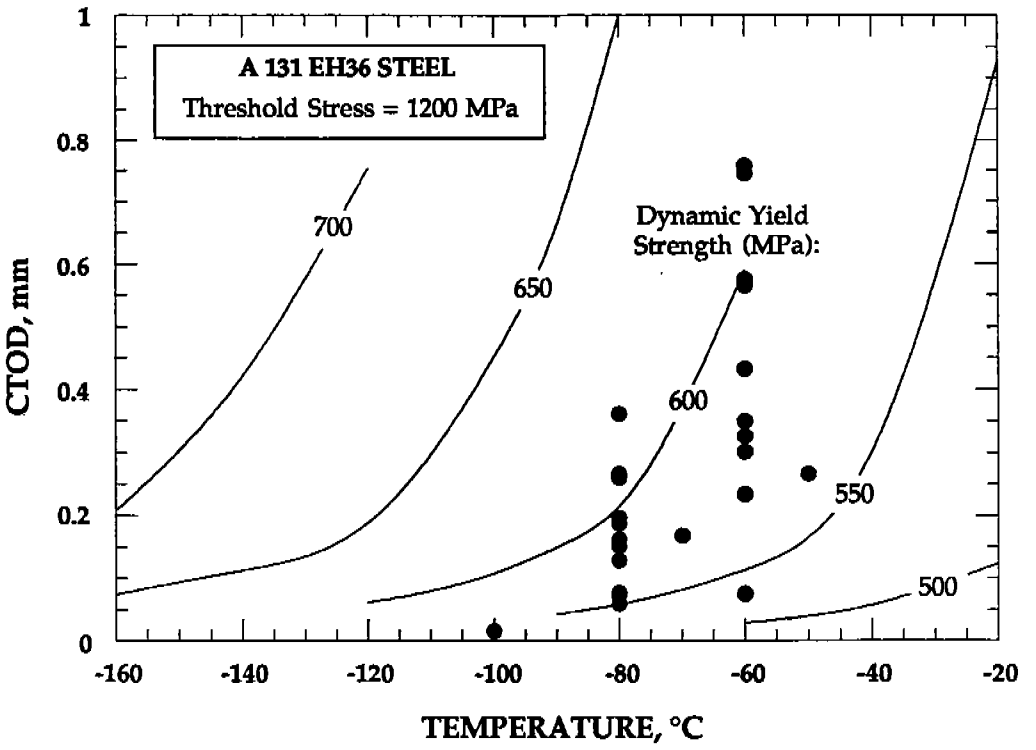

FIGURE 4.17 Effect of the dynamic yield strength on predicted CTOD in the A 131 EH 36 steel.

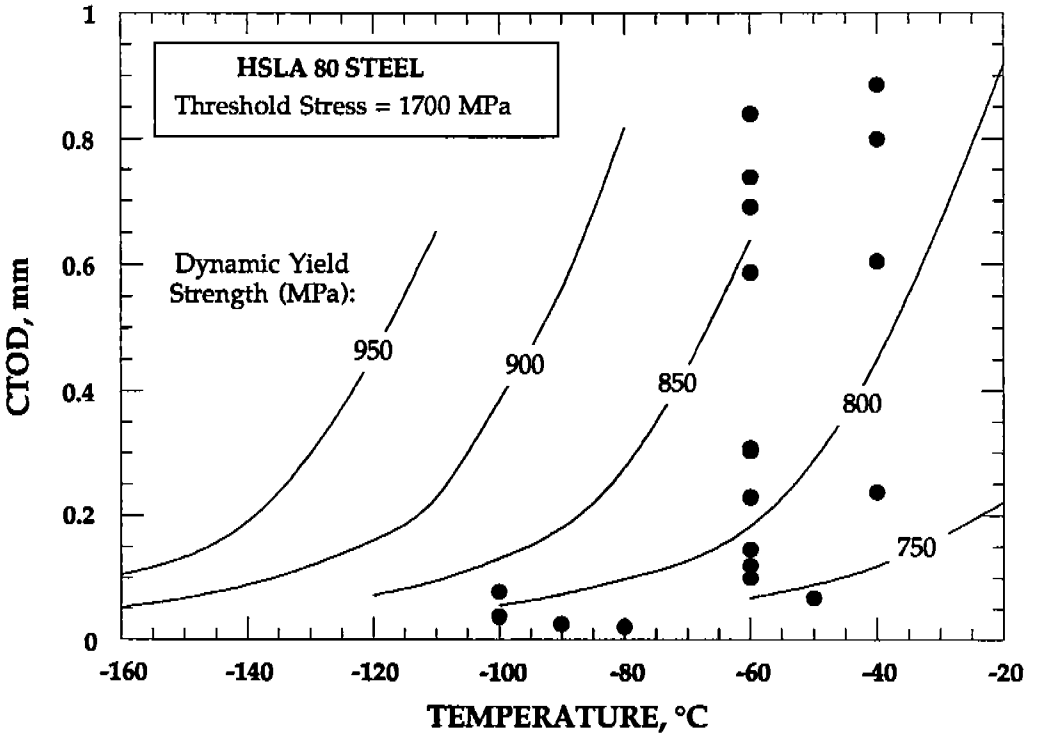

FIGURE 4.18 Effect of the dynamic yield strength on predicted CTOD in the HSLA 80 steel.

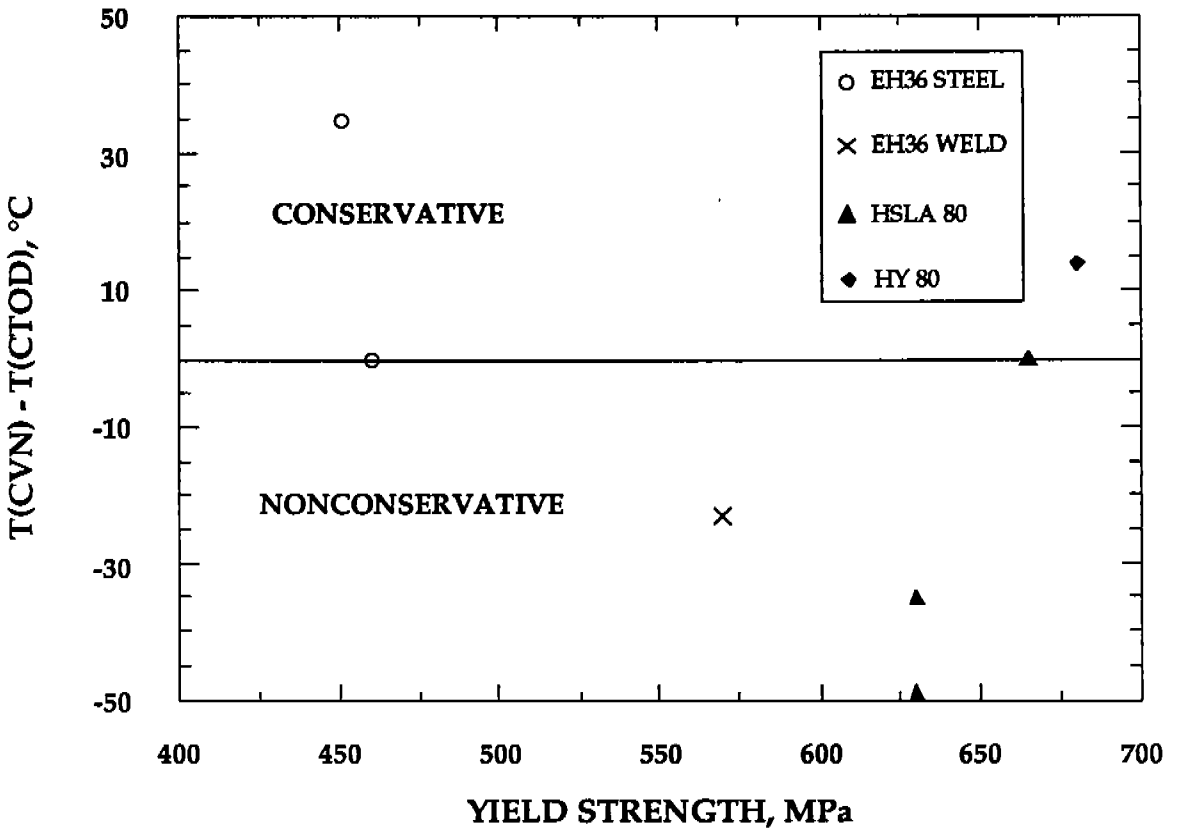

FIGURE 4.19 **Comparison between the 20 J CVN transition temperature with the 0.1 mm CTOD transition for several steel plates.**

5. SUMMARY AND CONCLUSIONS

A series of mechanical tests were performed on two ship steels: ASTM A 131 EH36 and HSLA 80. Tensile tests performed over a wide range of temperatures and strain rates indicated that both materials were rate sensitive. An unusual rate dependence was observed in that an intermediate strain rate exhibited higher flow stress than the highest rate. This apparent anomaly may be a result of noise in the high rate data caused by dynamic oscillations. Charpy and fracture toughness tests revealed that both steels possess high toughness. The CTOD transition for each material occurs in the range -80 to -40°C.

Finite element analysis and a local cleavage failure criterion led to the following size requirements for J and CTOD:

$$B, b \geq \frac{200\, J_c}{\sigma_Y} \tag{5.1a}$$

and

$$B, b \geq 300\, \delta_c \tag{5.1b}$$

Equation (5.1a) is eight times as strict as the size requirements for J_{IC}. When fracture toughness data cannot meet the requirements of Eq. (5.1), the data can be corrected for constraint loss. The present analysis successfully removed geometry dependence of shallow and deep notched specimens of A 36 steel. When the constraint correction was applied to transition region data for the two ship steels tested in this study, the scatter was greatly reduced. This approach provides a framework for predicting fracture in structures when either the structure or the test specimen is not fully constrained. Implementing such an approach, however, would require a large number of detailed numerical analyses.

Relationships between J and CTOD were established both analytically and experimentally. These two parameters are essentially equivalent measures of elastic-plastic fracture toughness.

The relationship between Charpy energy and fracture toughness is less clear, however. A theoretical correlation gave reasonable predictions of CTOD in the transition region, but further refinement and validation of this model is needed. The predicted transition curves were highly sensitive to the assumed dynamic flow

properties. A comparison between CVN and CTOD transition temperatures implied that there is not a unique relationship between the two temperatures. Thus, material toughness requirements based on Charpy may either be overly conservative or unsafe, depending on the material.

Future work should be directed toward incorporating the effects of thickness and ductile tearing into the constraint analysis. The theoretical CVN-fracture toughness relationship should also be studied further.

6. REFERENCES

1. Anderson, T.L., "Application of Elastic-Plastic Fracture Mechanics to Welded Structures: A Critical Review." Mechanics and Materials Center Report MM 6165-89-11, Texas A&M University, College Station, TX, August 1989.

2. E399-83, "Standard Test Method for Fracture Toughness of Metallic Materials." American Society for Testing and Materials, Philadelphia, PA, 1983.

3. E813-87, "Standard Test Method for J_{Ic}, a Measure of Fracture Toughness." American Society for Testing and Materials, Philadelphia, PA, 1987.

4. E1152-87 "Standard Test Method for Determining J-R Curves." American Society for Testing and Materials, Philadelphia, PA, 1987.

5. E1290-89 "Standard Test Method for Crack Tip Opening Displacement Testing." American Society for Testing and Materials, Philadelphia, PA, 1989.

6. Burdekin, F.M. and Dawes, M.G., "Practical Use of Linear Elastic and Yielding Fracture Mechanics with Particular Reference to Pressure Vessels." Proceedings of the Institute of Mechanical Engineers Conference, London, May 1971, p.28.

7. PD 6493:1980, "Guidance on Some Methods for the Derivation of Acceptance Levels for Defects in Fusion Welded Joints." British Standards Institution, March 1980.

8. Harrison, R.P., Loosemore, K., Milne, I, and Dowling, A.R., "Assessment of the Integrity of Structures Containing Defects." Central Electricity Generating Board Report R/H/R6-Rev 2, April 1980.

9. Ainsworth, R.A., "The Assessment of Defects in Structures of Strain Hardening Materials." *Engineering Fracture Mechanics*, Vol. 19, 1984, p. 633.

10. Anderson, T.L. and Dodds, R.H. "Specimen Size Requirements for Fracture Toughness Testing in the Transition Region." Submitted to *Journal of Testing and Evaluation*, December, 1989.

11. Anderson, T.L., McHenry, H.I. and Dawes, M.G., "Elastic-Plastic Fracture Toughness Testing with Single Edge Notched Bend Specimens." ASTM STP 856, American Society of Testing and Materials, Philadelphia, PA, 1985. pp. 210-229.

12. Anderson, T.L., "Crack Tip Parameters for Large Scale Yielding and Low Constraint Configurations." *International Journal of Fracture*, Vol 41, pp. 79-104, 1989.

13. BS 5762: 1979, "Methods for Crack Opening Displacement (COD) Testing." British Standards Institution, London, 1979.

14. Shih, C.F. and German, M.D., "Requirements for a One Parameter Characterization of Crack Tip Fields by the HRR Singularity." *International Journal of Fracture*, Vol. 17, 1981, pp. 27-43.

15. McMeeking, R.M. and Parks, D.M., "On Criteria for J-Dominance of Crack-Tip Fields in Large-Scale Yielding." ASTM STP 668, American Society of Testing and Materials, Philadelphia, PA, 1979, pp. 175-194.

16. Hutchinson, J.W., "Singular Behavior at the End of a Tensile Crack Tip in a Hardening Material." *Journal of the Mechanics and Physics of Solids*, Vol. 16, 1968, pp. 13-31.

17. Rice, J.R. and Rosengren, G.F., Plane Strain Deformation near a Crack Tip in a Power-Law Hardening Material." *Journal of the Mechanics and Physics of Solids*, Vol. 16, 1968, pp. 1-12.

18. Shih, C.F. "J-Dominance under Plane Strain Fully Plastic Conditions: the Edge Crack Panel Subject to Combined Tension and Bending." *International Journal of Fracture*, Vol. 29, 1985, pp. 73-84.

19. Shih, C.F., Moran, B., and Nakamura, T., "Energy Release Rate along a Three-Dimensional Crack Front in a Thermally Stressed Body." *International Journal of Fracture*, Vol. 30, 1986, pp. 79-102.

20. Dodds, R.H. Jr. and Anderson T.L., "A Framework to Correlate a/W Effects on Elastic-Plastic Fracture Toughness (J_c)." to be published in *International Journal of Fracture*.

21. Lin, T., Evans, A.G. and Ritchie, R.O., "Statistical Model of Brittle Fracture by Transgranular Cleavage." *Journal of the Mechanics and Physics of Solids*, Vol 34, 1986, pp. 477-496.

22. Wallin, K., Saario, T., and Törrönen, K., "Statistical Model for Carbide Induced Brittle Fracture in Steel." *Metal Science*, Vol. 18, 1984, p. 13.

23. Beremin, F.M., "A Local Criterion for Cleavage Fracture of a Nuclear Pressure Vessel Steel." *Metallurgical Transactions*, Vol. 14A, 1983, p. 2277.

24. Anderson, T.L. and Stienstra, D., "A Model to Predict the Sources and Magnitude of Scatter in Toughness Data in the Transition Region." *Journal of Testing and Evaluation*, Vol. 17, 1989, pp. 46-53.

25. Narasimhan, R. and Rosakis A.J., "Three Dimensional Effects Near a Crack Tip in a Ductile Three Point Bend Specimen - Part I: A Numerical Investigation." California Institute of Technology, Division of Engineering and Applied Science, Report SM 88-6, Pasadena, CA, January 1988.

26. Landes J.D. and Shaffer, D.H., "Statistical Characterization of Fracture in the Transition Region." ASTM STP 700, American Society of Testing and Materials, Philadelphia, PA, 1980, p. 368.

27. Sorem, W.A., "The Effect of Specimen Size and Crack Depth on the Elastic-Plastic Fracture Toughness of a Low-Strength High-Strain Hardening Steel." Ph.D Dissertation, University of Kansas, Lawrence, KS, May 1989.

22. Shih, C.F., "Relationship between the J-Integral and the Crack Opening Displacement for Stationary and Extending Cracks." *Journal of the Mechanics and Physics of Solids*, Vol 29, 1981, pp. 305-326.

29. Zapata, J.E., "An Experimental Validation of a Theoretical Charpy-Fracture Toughness Correlation." Master of Science Thesis, Texas A&M University, College Station, TX, December 1989.

30. Norris, D.M., "Computer Simulation of the Charpy V-Notch Toughness Test." *Engineering Fracture Mechanics*, Vol. 11, pp. 261-274, 1979.

COMMITTEE ON MARINE STRUCTURES

Commission on Engineering and Technical Systems

National Academy of Sciences - National Research Council

The COMMITTEE ON MARINE STRUCTURES has technical cognizance over the interagency Ship Structure Committee's research program.

Stanley G. Stiansen (Chairman), Riverhead, NY
Mark Y. Berman, Amoco Production Company, Tulsa, OK
Peter A. Gale, Webb Institute of Naval Architecture, Glen Cove, NY
Rolf D. Glasfeld, General Dynamics Corporation, Groton, CT
William H. Hartt, Florida Atlantic University, Boca Raton, FL
Paul H. Wirsching, University of Arizona, Tucson, AZ
Alexander B. Stavovy, National Research Council, Washington, DC
Michael K. Parmelee, Secretary, Ship Structure Committee, Washington, DC

LOADS WORK GROUP

Paul H. Wirsching (Chairman), University of Arizona, Tucson, AZ
Subrata K. Chakrabarti, Chicago Bridge and Iron Company, Plainfield, IL
Keith D. Hjelmstad, University of Illinois, Urbana, IL
Hsien Yun Jan, Martech Incorporated, Neshanic Station, NJ
Jack Y. K. Lou, Texas A & M University, College Station, TX
Naresh Maniar, M. Rosenblatt & Son, Incorporated, New York, NY
Solomon C. S. Yim, Oregon State University, Corvallis, OR

MATERIALS WORK GROUP

William H. Hartt (Chairman), Florida Atlantic University, Boca Raton, FL
Fereshteh Ebrahimi, University of Florida, Gainesville, FL
Santiago Ibarra, Jr., Amoco Corporation, Naperville, IL
Paul A. Lagace, Massachusetts Institute of Technology, Cambridge, MA
John Landes, University of Tennessee, Knoxville, TN
Mamdouh M. Salama, Conoco Incorporated, Ponca City, OK
James M. Sawhill, Jr., Newport News Shipbuilding, Newport News, VA

SHIP STRUCTURE COMMITTEE PUBLICATIONS

SSC-332 Guide for Ship Structural Inspections by Nedret S. Basar & Victor W. Jovino 1985

SSC-333 Advance Methods for Ship Motion and Wave Load Prediction by William J. Walsh, Brian N. Leis, and J. Y. Yung 1989

SSC-334 Influence of Weld Porosity on the Integrity of Marine Structures by William J. Walsh , Brian N. Leis, and J. Y. Yung 1989

SSC-335 Performance of Underwater Weldments by R. J. Dexter, E. B. Norris, W. R. Schick, and P. D. Watson 1986

SSC-336 Liquid Slosh Loading in Slack Ship Tanks; Forces on Internal Structures & Pressures by N. A. Hamlin 1986

SSC-337 Part 1 - Ship Fracture Mechanisms Investigation by Karl A. Stambaugh and William A. Wood 1987

SSC-337 Part 2 - Ship Fracture Mechanisms - A Non-Expert's Guide for Inspecting and Determining the Causes of Significant Ship Fractures by Karl A. Stambaugh and William A. Wood 1987

SSC-338 Fatigue Prediction Analysis Validation from SL-7 Hatch Corner Strain Data by Jen-Wen Chiou and Yung-Kuang Chen 1985

SSC-339 Ice Loads and Ship Response to Ice - A Second Season by C. Daley, J. W. St. John, R. Brown, J. Meyer, and I. Glen 1990

SSC-340 Ice Forces and Ship Response to Ice - Consolidation Report by C. Daley, J. W. St. John, R. Brown, and I. Glen 1990

SSC-341 Global Ice Forces and Ship Response to Ice by P. Minnick, J. W. St. John, B. Cowper, and M. Edgecomb 1990

SSC-342 Global Ice Forces and Ship Response to Ice - Analysis of Ice Ramming Forces by Yung-Kuang Chen, Alfred L. Tunik, and Albert P-Y Chen 1990

SSC-343 Global Ice Forces and Ship Response to Ice - A Second Season by p. Minnick and J. W. St. John 1990

SSC-344 Development of an Onboard Strain Recorder by Eric Greene and William A. Wood 1987

None Ship Structure Committee Publications - A Special Bibliography 1983